THE UNIVERSITY OF READING

Estimation of the Diurnal Variability of Sea Surface Temperatures using Numerical Modelling and the Assimilation of Satellite Observations

Thesis submitted for the degree of

Doctor of Philosophy

School of Mathematics, Meteorology and Physics

Samuel Pimentel

December 2006

ABSTRACT

This thesis is concerned with the diurnal cycle of sea surface temperature (SST). The diurnal variability of SSTs are an important feature of the climate system. In order to obtain accurate SST records and reduce errors in satellite derived SST estimates an understanding of the diurnal signals in these observations are essential. Satellite derived SST observations measure the skin and sub-skin layers whereas ocean models typically resolve a 5 metre temperature. An understanding of these differences are important for assimilation of SST.

In this thesis a one-dimensional mixed layer ocean model is improved and developed with the capability of representing the dominant processes involved in the development of the diurnal cycle of SSTs. The model is forced with operational forecast data and used to build spatial maps of the diurnal warming.

The extent of the diurnal warming at a particular location and time is predominately governed by a non-linear response to the cloud cover and sea surface wind speeds over the day. The accuracy of the modelled SST is hampered by uncertainty in these forcing variables. A novel algorithm is developed that uses SST observations to derive corrections to the wind speeds and cloud cover values. These corrections are determined such that the corrected forcing values result in model trajectories that better fit the SST observations. Results reveal SST estimates and air-sea fluxes that are more consistent with observations. This technique provides a dynamic observation operator that can be used to remove diurnal warming signals from observations and provide estimates of skin to foundation temperature differences. This new method is an invaluable tool in providing accurate measures of the diurnal warming. Overall this thesis has advanced knowledge in modelling diurnal variability and established an improved method for assimilating satellite SST observations by taking account of the diurnal cycle.

ACKNOWLEDGEMENTS

DECLARATION

I confirm that this is my own work and the use of all material from other sources has been properly and fully acknowledged.

Samuel Pimentel

Contents

List of Figures

List of Tables

0.1 List of Abbreviations

AATSR	Advanced Along-Track Scanning Radiometer
AVHRR	Advanced Very High Resolution Radiometer
CMO	Coastal Mixing and Optics Experiment
COARE	Coupled Ocean-Atmosphere Response Experiment
DW	Diurnal Warming
ECMWF	European Centre for Medium-Range Weather Forecasts
EnKF	Ensemble Kalman Filter
ENSO	El Nino Southern Oscillation
ESSC	Environmental Systems Science Centre
FOAM	Forecast Ocean Analysis Model
GCM	General Circulation Model
GHRSST-PP	GODAE High Resolution Sea Surface Temperature Pilot Project
GMT	Greenwich Mean Time
GODAE	Global Ocean Data Assimilation Experiment
GOCE	Geostationary Operational Environment Satellite
GOTM	General Ocean Turbulence Model
HADISST	Hadley Centre Sea Ice and Sea Surface Temperature Data Set
IR	Infrared
JAXA	Japan Aerospace Exploration Agency
LWR	Long-wave Radiation
MLD	Mixed Layer Depth
MOST	Monin-Obukhov Similarity Theory
MW	Microwave
NAR	North Atlantic Regional

NASA	National Aeronautics and Space Administration
NCAR	National Center for Atmospheric Research
NCOF	National Centre for Ocean Forecasting
NWP	Numerical Weather Prediction
OI	Optimal Interpolation
OSTIA	Ocean Sea Temperature and Ice Analysis
PDE	Partial Differential Equation
POLCOMS	Proudman Oceanographic Laboratory Coastal Ocean Modelling System
RMS	Root Mean Square
RSOI	Reduced Space Optimal Interpolation
SeaWiFS	Sea-viewing Wide Field-of-view Sensor
SEVIRI	Spinning Enhanced Visible and Infrared Imager
SST	Sea Surface Temperature
STD	Standard Deviation
SWR	Short-wave Radiation
TKE	Turbulent Kinetic Energy
TMI	TRMM Microwave Imager
TOGA	Tropical Ocean Global Atmosphere
TRMM	Tropical Rain Measuring Mission
UKMO	United Kingdom Meteorological Office
WHOI	Woods Hole Oceanographic Institute

0.2   List of Symbols

b	Buoyancy
c_p	Specific heat capacity of sea water at constant pressure
c_{pa}	Specific heat capacity of air at constant pressure
$c_\mu,\ c'_\mu$	Stability functions
e	Water vapour pressure
g	Gravitational acceleration
h	Height above sea surface
h_i	Thichness of model grid layer i
k	Turbulent kinetic energy; thermal conductivity of sea water
l	Generic length scale
n	Fractional cloud cover
p	Sea water pressure
q	Water vapour mixing ratio
q_{rh}	Relative humidity
$\boldsymbol{u} = (u, v)^T$	Horizontal wind velocities
$u_*,\ q_*,\ T_*$	Scaling parameters
$\boldsymbol{v} = (u, v)^T$	Horizontal sea water velocities
z	Depth in the water column
$z_0,\ z_{0q},\ z_{0T}$	Roughness lengths
z_{MLD}	Mixed layer depth
z^i	Depth at model grid layer i
A_a	Water vapour and ozone absorption
B	Production of turbulent kinetic energy by buoyancy
$C_D,\ C_E,\ C_H$	Transfer coefficients for momentum, latent and sensible heat respectively
C_n	Cloud cover coefficient used in Reed formula

I_0	Net surface short-wave radiation
$I_\downarrow$	Clear Sky Surface insolation
I_{diff}	Surface diffuse insolation
I_{dir}	Surface direct insolation
L	Monin-Obukhov length
L_v	Latent heat of vapourization
P	Production of turbulent kinetic energy by mean shear
Q	Net surface heat flux without solar radiation
Q_B	Net surface long-wave radiation
$Q_B^\downarrow$	Downwelling long-wave radiation
Q_E	Latent heat flux
Q_H	Sensible heat flux
Re	Reynolds number
S	Sea water salinity
S_0	Solar constant
T_a	Air temperature
T_v	Virtual air temperature
α	Albedo
α_L	Long-wave reflectivity
β	Solar noon angle
δ	Sun declination angle
ϵ	Rate of dissipation; surface emissivity
ν	Kinematic fluid viscosity
$\nu^m,\ \nu^\theta,\ \nu^S$	Molecular diffusivities of momentum, heat, and salinity respectively
$\nu_t,\ \nu_t'$	Turbulence diffusivity parameters
θ	Sea water temperature
κ	von Karman constant
λ	Saunders coefficient

λ_n	Latitude dependent cloud cover coefficient
ρ	Sea water density
ρ_0	Reference sea water density
ρ_a	Air density
σ	Stefan-Boltzmann constant
$\sigma_k, \sigma_\epsilon$	Schmidt number for turbulent kinetic energy and dissipation respectively
τ	Atmospheric transmission coefficient
$\boldsymbol{\tau} = (\tau_x, \tau_y)^T$	Wind stresses
ϕ	Latitude
ϕ_m, ϕ_q, ϕ_T	Stability parameters
ω	Solar zenith angle
Ψ_m, Ψ_q, Ψ_T	Stability corrections
$\nabla = \left(\frac{\partial}{\partial x}, \frac{\partial}{\partial y} \right)$	Horizontal gradient, x and y are the eastward and northward coordinates respectively

Chapter 1

Introduction

1.1 Motivation

Knowledge of sea surface temperatures (SSTs) has importance for humankind with many valuable social and economic benefits. The SST is a crucial component in many physical, biological, and chemical processes within the Earth system. It is one of the most important properties governing the exchange of energy between the atmosphere and ocean and as such is of paramount importance in air-sea flux calculations. A good knowledge of SST is therefore germane in our understanding of upper ocean physical, biogeochemical processes, and air-sea interaction. SST is a variable widely used for describing ocean circulation and dynamics. It has an important role in Numerical Weather Prediction (NWP) as a boundary condition in General Circulation Models (GCMs) and therefore is valuable for weather forecasting. For example a necessary condition for the genesis of tropical cyclones is that the SST be above approximately $26\,°C$ and SST maps are used to evaluate oceanic heat content, which is important for predicting hurricane intensity development [126] and [45]. It also has an important role in climate science where it is viewed as a key indicator of climate change and variability [53].

1.2   Air-Sea Interaction

The SST may be perceived as being determined by a balance of many processes, including air-sea exchange, ocean transport, and ocean mixing. Figure 1.1 illustrates these principal environmental processes that affect SST. An understanding of these processes and their interactions is vital for the beneficial inclusion of global high resolution SST observations into ocean models.
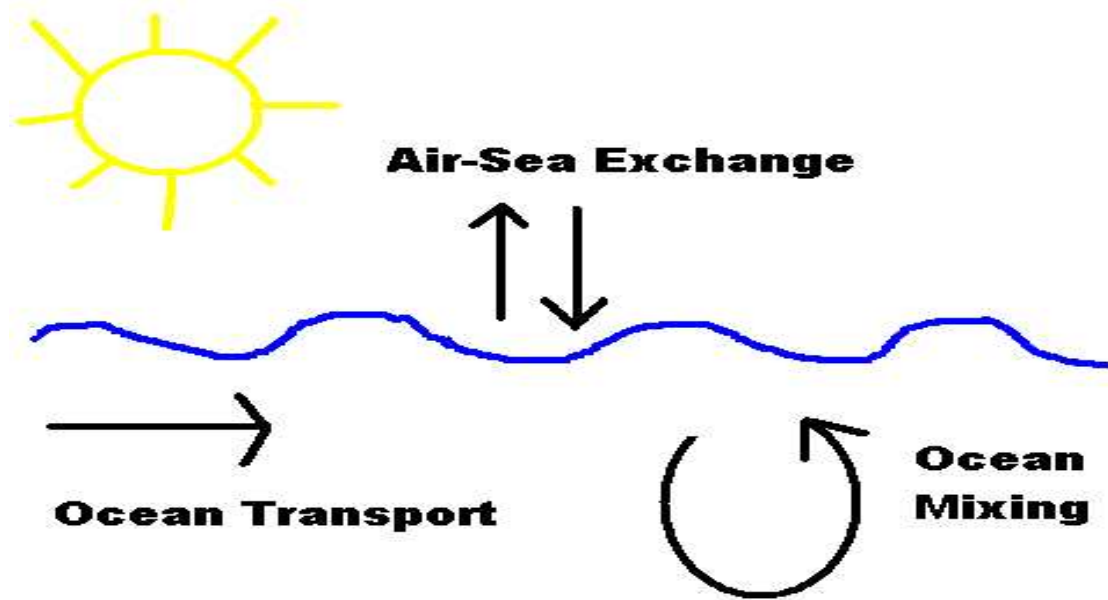
Figure 1.1: *A schematic diagram illustrating the various processes that influence SST in the ocean-atmosphere system.*

1.3   Oceanic Heat Budget

The heat budget of the oceanic mixed layer represents a balance of several terms [132]

$$z_{\mathrm{MLD}}\frac{\partial \theta_a}{\partial t} + z_{\mathrm{MLD}}(\boldsymbol{v_a}.\nabla\theta_a + \overline{\boldsymbol{v}'_a \cdot \nabla\theta'_a}) + (\theta_a - \theta_{z_{\mathrm{MLD}}})w_e + \nabla \cdot \int_{z_{\mathrm{MLD}}}^{0} \hat{\boldsymbol{v_a}}\hat{\theta}_a dz = \frac{Q + Q_{z_{\mathrm{MLD}}}}{\rho c_p}. \tag{1.1}$$

From left to right the terms represent, local storage, horizontal advection (split into mean and eddy terms), entrainment, vertical temperature and velocity covariance, and the combination of net atmospheric heating and vertical turbulent diffusion at the base of the mixed layer, where z_{MLD} is the mixed layer depth, θ_a and $\boldsymbol{v_a} = (u_a, v_a)^T$ are the mixed layer depth averaged sea temperature and horizontal velocities, over-bar represents a time mean, θ_a' and $\boldsymbol{v_a'}$ are deviations from the mean, $\hat{\theta}_a$ and $\hat{\boldsymbol{v_a}}$ represent deviations from the vertical average. The entrainment velocity w_e can be replaced by $\frac{\partial z_{\mathrm{MLD}}}{\partial t} + \nabla \cdot z_{\mathrm{MLD}} \boldsymbol{v_a}$ following [132]. The net surface heat flux without solar radiation, denoted Q, can be split into the following

$$Q = Q_E + Q_B + Q_H. \tag{1.2}$$

From left to right these components represent the latent heat flux, the net surface long-wave radiation and the sensible heat flux, with units Wm^{-2}. The term $Q_{z_{\mathrm{MLD}}}$ can be separated as follows

$$Q_{z_{\mathrm{MLD}}} = I_0 - I_{z_{\mathrm{MLD}}} + \rho c_p \overline{w'\theta'}_{Z_{\mathrm{MLD}}}, \tag{1.3}$$

where I_0 denotes the net surface solar radiation, with units Wm^{-2}. The mixed layer does not absorb all of I_0, a fraction $I_{z_{\mathrm{MLD}}}$ penetrates below depth z_{MLD}. The final entry is turbulent diffusion at the base of the mixed layer.

Simplifications to this complete heat budget and a more in-depth look at the various sources and sinks are presented in Chapter 3.

1.4   Observations

1.4.1   In-Situ Observations

A limited number of in-situ observations of SST are available from ocean moorings, buoys, and ship observations. Argo floats [47] provide vital profile information of temperature and salinity needed to initialise ocean models. In this thesis a few research moorings providing intensive periods of observations are used to validate an ocean model and develop assimilation routines.

1.4.2   Satellite Derived SST

SST measured from Earth observation satellites is increasingly required for use in the context of operational monitoring and forecasting of the ocean, for assimilation into coupled ocean-atmosphere model systems and for applications in short-term NWP and longer term climate change detection. The wealth of satellite SST data now available for scientific research opens the possibility of large improvements to SST estimation. Currently there are many different operational SST data products available; most are derived at least in part from satellite systems [106]. Space borne SST observations are derived from brightness temperatures as measured by infrared (IR) or microwave (MW) radiometers. The performance of infrared radiometers is hampered by cloud cover, whereas the microwave radiation is able to propagate through clouds, but observations can be contaminated by heavy rainfall (see Section 6.3 for more information).

1.5   Diurnal Variability

The optimal use of such data, however, is not straight forward. Donlon et al [32] discusses the difficulties in validation of satellite SST measurements; they argue that a better understanding of the spatial and temporal variability of thermal stratification of the upper-ocean layers especially during low-wind speed conditions is fundamental for this validation. To utilise the full range of SST observations available (satellite IR and MW, buoys, and ship measurements) extreme care must be taken to account for the different depths and local times of each observation.

1.5.1   Temporal Variability

Diurnal warming was reported by Stommel [134] in 1969 and has since been investigated by a number of authors at various locations e.g. [23], [104], [105], [151], and [136]. Intense diurnal warming of the surface of the ocean commonly occurs in low wind and clear sky conditions, when the wind-driven turbulence is insufficient to erode the near-surface re-stratification caused by absorption of solar radiation during the day. This buoyant highly stratified warm layer leads to an afternoon (local time) diurnal

peak, after which the amplitude decays as surface cooling triggers oceanic convection and surface stress causes vertical shear, breaking down the diurnal thermocline [104]. Warming in favourable conditions can be 3.5 °C [135], although an astounding diurnal variability of over 6 °C has been recorded [40]. In contrast, when an active wind-driven mixed layer is present, the diurnal amplitude of surface temperature seldom exceeds a few tenths of degrees. Indeed even under favourable conditions a sharp wind burst is often enough to break down the near surface stratification [138].

Since SST retrievals by satellites are sensitive to a thin surface layer, this diurnal warming effect strongly influences these measurements. Often the local time of SST observations are not taken into account when merging satellite data to produce observational products, e.g. Reynolds [112]; this leads to biases in these products. Problems are also encountered when assimilating SST observations as current ocean models do not try to resolve these diurnal effects so a diurnally 'corrupted' observation assimilated into the model could result in a misleading signal. A more sensible approach beginning to be adopted is to flag observations that are taken during the day in low wind speed conditions; this reduces the likelihood of a bias due to diurnal warming, e.g. OSTIA (see Section 5.3.5).

1.5.2 Spatial Variability

As the solar heating warms and stabilises the upper ocean, limiting the downward penetration of turbulent wind mixing, the thermal response produces a warm stratified layer in which air-sea fluxes of heat and momentum are surface trapped. The trapping depth is set by the opposing effects of stabilising heat flux and destabilising surface stress [104]. This warm layer is associated with the rise in SST and decrease in mixed layer depth. This phenomenon results in daily variability of the upper ocean vertical temperature profile. An idealised typical day and night profile is seen in Figure 1.2.

A variety of SST observations from various sources are often used in conjunction without taking into account the depth at which these temperature observations are representative. Satellite observations especially, represent a near surface layer; however, these observations are assimilated into ocean models that do not resolve such fine

spatial structure. The SST at 5 metres (the depth at the centre of the top grid box in a typical high resolution ocean model) can be several degrees cooler than the near surface temperature. Without knowing the temperature differences at the relevant depths we can not utilise all the information content available in observations.

1.5.3 Definitions

Evidently care needs to be taken in how the term 'SST' is used and defined. What follows is a classification of SSTs that takes into account the vertical temperature structure of the upper ocean. These were introduced by Donlon et al [32] and used by the GODAE High Resolution Sea Surface Temperature Pilot Project (GHRSST-PP) and shall be adopted throughout this thesis.
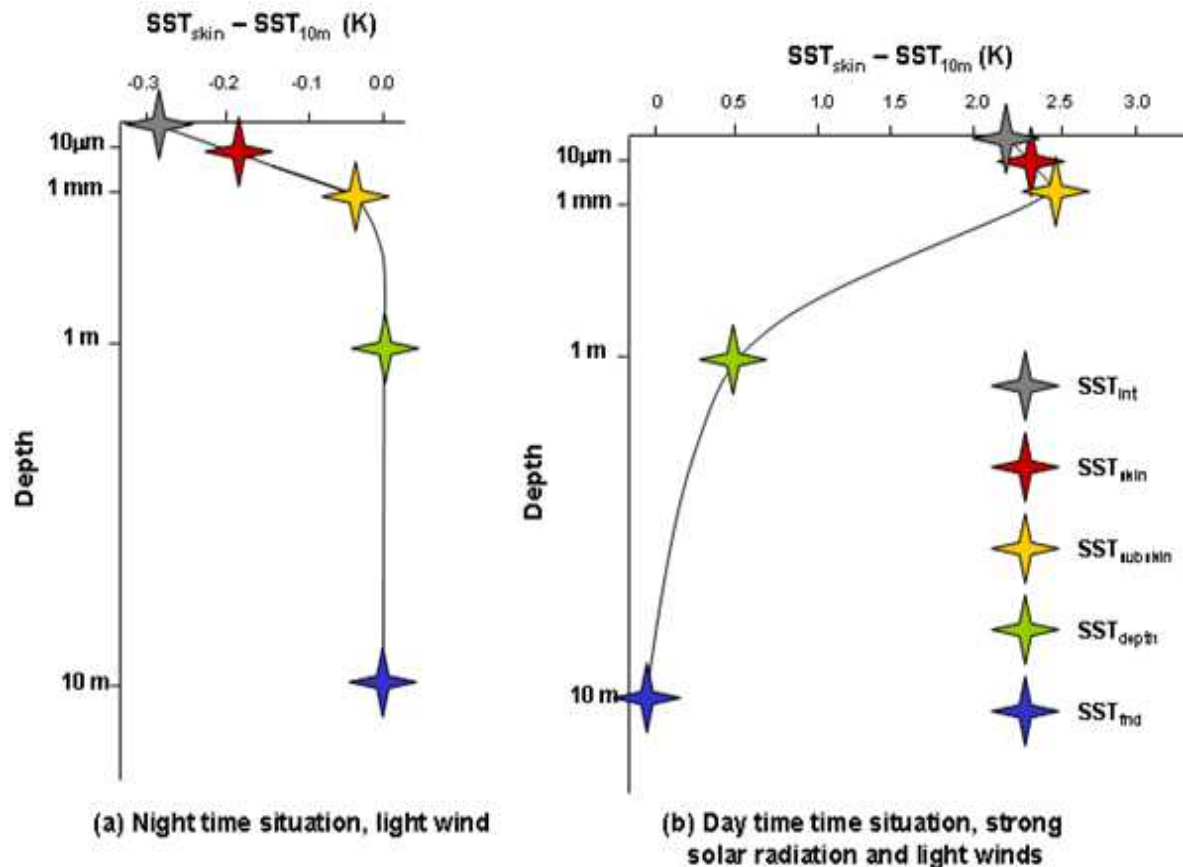
Figure 1.2: *A schematic diagram showing a typical vertical temperature structure of the upper ocean at a) night and b) day. This schematic is reproduced from [107]*

- The interface SST, (θ_{int}), is a theoretical temperature at the precise air-sea interface. θ_{int} is of no practical use because it cannot be measured using current technology.

- The skin SST, (θ_{skin}), is defined as the temperature measured by an infrared radiometer operating in the 10–$12\,\mu$m spectral wave-band. As such, it represents the actual temperature of the water across a very small depth of approximately $20\,\mu$m. This definition is chosen for consistency with the majority of infrared satellite and ship mounted radiometer measurements. As seen in Figure 1.2 the skin SST is slightly cooler than the interior temperature just below; this is because of evaporative and radiative cooling (see Section 3.5.9).

- The sub-skin SST, $(\theta_{\mathrm{subskin}})$, represents the temperature at the base of the thermal skin layer. The difference between θ_{int} and $\theta_{\mathrm{subskin}}$ is related to the net flux of heat through the thermal skin layer. For practical purposes, $\theta_{\mathrm{subskin}}$ can be well approximated to the measurement of surface temperature by a microwave radiometer operating in the 6–$11\,$GHz frequency range. $\theta_{\mathrm{subskin}}$ is the temperature of a layer $1\,$mm thick at the ocean surface.

- θ_{depth} or $\theta(z)$, is the terminology adopted by GHRSST-PP to represent an in-situ measurement near the surface of the ocean that is typically reported simply as SST or "bulk" SST. For example θ_{6m} or $\theta\,(6\mathrm{m})$ would refer to an SST measurement made at a depth of 6 metres.

- The foundation SST, is defined as the top temperature in the water column free of diurnal temperature variability. This will be equal to the $\theta_{\mathrm{subskin}}$ in the absence of any diurnal signal. It is named to indicate that it is the foundation temperature from which the growth of the diurnal thermocline develops each day. The foundation SST product provides an SST that is free of any diurnal variations (daytime warming or nocturnal cooling).

1.6   The Influence of Diurnal Variability

The diurnal cycle is a fundamental signal in the climate system [157]. Increasingly it is being seen to have an impact on longer time scales. Many authors have commented on the significance of the diurnal cycle to the ocean-atmosphere coupled system (see the discussion in Sections 1.6.1–1.6.4). This is particularly true in the western Pacific warm pool, which experiences large diurnal amplitudes. The implications of a deeper understanding of the diurnal variability will benefit several areas.

1.6.1   Consequences for SST

Bernie et al [9] used a one-dimensional mixed layer model of the ocean forced with measurements from the intensive observing period of the Tropical Ocean Global Atmosphere Coupled Ocean-Atmosphere Response Experiment (TOGA COARE). Comparing model outcomes produced from hourly fluxes with those using daily mean fluxes they concluded that in the western warm pool the rectification of the diurnal cycle of SST onto the daily mean SST accounted for one third of the magnitude of intra-seasonal variability of SST. This built on the earlier findings by Shinoda and Hendon [128] who from similar experiments indicate that the diurnal variation of short-wave radiation significantly affects the amplitude and phase of the intra-seasonal SST variation. Danabasoglu et al [26] included an idealised diurnal cycle of solar forcing in the Community Climate System Model. The daily mean solar radiation received in each daily coupling interval was distributed over 12 daylight hours. They found that the mean equatorial SST in the Pacific was warmed by as much as $1\,°C$, in better agreement with observations.

1.6.2   Impact on Fluxes

The key paper in the study of diurnal warming effects is that by Price and Weller [104]. A major conclusion from this paper is that the process of diurnal cycling plays an important role in shaping the long term response of the upper ocean to atmospheric forcing. Diurnal effects on mean SST are noticed in the calculated air-sea heat fluxes

which then have a feedback effect on future SSTs. NWP and climate simulations use standard SST datasets such as Reynolds et al [111] which produce monthly or weekly mean fixed bulk SSTs. These SSTs are used in the calculation of the air-sea fluxes. This process can lead to two sources of errors. Firstly the bulk SST is not the temperature at the interface and therefore should not be used in any flux calculations; earlier we noted that skin to bulk temperature differences can be significant. This is something that was addressed by Fairall et al [35] who developed a bulk flux algorithm that incorporated a warm layer and cool skin effect (see Section 3.5.8). The second source of error stems from the use of mean SST values which smooth out any diurnal variations in SST. Ledvina et al [75] showed that monthly, weekly, and daily averaged bulk meteorological parameters can lead to serious errors in fluxes especially in equatorial, temporally variable wind regimes. In another study in the western Sargasso Sea by Cornillon et al [23], they found that diurnal effects produced a monthly mean SST that was $0.2\,°C$ higher and resulted in a decrease of $5\,\mathrm{Wm}^{-2}$ in the mean heat flux entering the ocean. Webster et al [151] reveal that a $1\,°C$ change (or error) in SST would result in a change (or error) of $27\,\mathrm{Wm}^{-2}$ in the net surface heat flux of the tropical western Pacific. This is greater than the mean air-sea heat flux $(17.5\,\mathrm{Wm}^{-2})$ observed over a five month period in this region [154]. Using the NCAR Community Climate Model Wei et al [153] showed that an improved simulation of the intraseasonal variability in the western Pacific was found with model runs forced by weekly SSTs with a parameterised diurnal cycle [151] over those without a diurnal cycle. As explained in the section above Danabasoglu et al [26] found that diurnal coupling in the Community Climate Systems Model produced as much as $1\,°C$ warming to SSTs in the tropical oceans. However a simple rectification of the diurnal cycle can explain less than $0.1\,°C$ of this warming. They state that the atmospheric response to the warm SST anomalies display a very different heat flux signature and therefore that large scale air-sea coupling is a prime mechanism for amplifying the rectified, daily averaged SST signals seen by the atmosphere.

1.6.3 Repercussions for Mixed Layer Depth

Shinoda and Hendon [128] reported that the inclusion of the diurnal cycle of insolation produces a shallower, warmer mixed layer overlying a colder sub-mixed layer, as compared to that produced by daily mean insolation in modelling studies in the western Pacific. Danabasoglu et al [26] found the mean boundary layer reduced in their diurnal forcing experiments with the Community Climate Systems Model. Similarly, McCreary et al [80] found that diurnal forcing in the Arabian Sea was an important aspect of mixed layer dynamics and biology. With a three-dimensional physical-biological model they show that diurnal forcing alters the mixed layer and biological responses, among other things, by lengthening the time that the mixed layer is thick during the Northeast Monsoon, by strengthening the spring and fall blooms and delaying them by 3 weeks, and by intensifying phytoplankton levels during inter-monsoon periods. In another recent modelling study in the western Pacific, Bernie et al [9] state that the inclusion of the diurnal cycle enhances the strength of mixing across the thermocline by the proper representation of the night-time deep mixing in the ocean implying a rectification of the diurnal cycle onto the mean climate of the tropical ocean. Also in the western equatorial Pacific Shinoda [127] identifies upper-ocean mixing processes during night-time as the mechanism by which the diurnal cycle modulates the intra-seasonal SST. Surface warming during daytime creates a shallow diurnal warm layer near the surface, which can easily be eroded by surface cooling during night-time. Further cooling beyond eroding the previous days warming is difficult because it requires substantial energy to entrain deeper water into the mixed layer. Since the shallow mixed layer is not formed in experiments with daily mean surface fluxes, the SST for the hourly forcing case is warmer most of the time due to the diurnally varying solar radiation.

1.6.4 Effect on Horizontal SST Gradients

Katsaros and Soloviev, in [66] and [67], have illustrated how horizontal SST discontinuities occurring at fronts, eddies, and in storm wakes are diminished by diurnal variability. Numerical modelling and some field results were used to show that if both

sides of a horizontal SST discontinuity experience identical clear sky, low wind speed conditions, then the warmer side will produce a weaker diurnal SST signal than the cooler side. This is because on the warmer side the greater SST will cause a larger heat release (resulting from long-wave radiation and latent and sensible heat flux losses) from the ocean and thus dampen diurnal warming when compared with the colder side of the front. Thus, in this situation, remotely sensed data of the sea surface taken during the day would reveal a much reduced or even vanished horizontal gradient when compared to the initial (pre diurnal warming) horizontal gradient. However, the true horizontal gradient would still be present below the shallow diurnal thermocline. This masking or camouflaging of horizontal gradients in remotely sensed SST data could have adverse effects for users of such data e.g. the fishing industry, in the estimation of acoustic transmission, and the forecasting of hurricane development.

1.7 Diurnal Variability Modelling

Attempts to model the upper ocean response to diurnal heating, cooling, and wind mixing are limited in number. Accurately modelling diurnal variability is difficult as it involves the complex non-linear interaction between ocean and atmosphere. However, attention should focus on a few core issues: the choice of mixing parameterisations, flux forcing resolution, vertical grid resolution, and the penetration of solar radiation. In this section a review of studies that have specifically focused on modelling the diurnal cycle of SSTs is presented, focusing on the above issues.

The first detailed modelling study of the diurnal cycle was by Price et al [104] who developed a bulk model dependent on the generation of shear instability at the base of the mixed layer. This model was also used by Shinoda to model diurnal variability in the western equatorial Pacific [128] and [127]. Hallsworth [50] compared the Price bulk mixed layer model with a turbulence closure model called GOTM (See Chapter 2) at two mooring sites and consistently found GOTM performing better at modelling the diurnal cycle of near surface temperatures. An alternative earlier bulk model by Kraus and Turner [72] was compared to the diffusion model of Kantha and Clayson

[62] in a study on modelling the diurnal thermocline by Horrocks et al [52]. They found that the Kraus-Turner model reasonably indicated when diurnal thermoclines should be expected, but was inadequate at predicting the magnitude. The main limitation was the reliance on mechanical and buoyancy driven mixing, which under strong solar heating and low wind speed is non existent and thus leads to heat build up with no mechanism, such as diffusion or conduction, to draw heat downwards. Whereas the Kantha-Clayson model was far more effective at predicting diurnal amplitudes.

Essential to modelling a diurnal cycle of SST is to force the model with diurnally varying surface fluxes especially the solar radiation. However high frequency forcing data are not always available; this presents a major restraint on diurnal modelling. Diurnal modelling studies have often been based at the TOGA COARE site ([151], [127], and [9]) where high resolution observed meteorology (every 15 minutes) is available. Bernie et al [9] performed experiments with varied flux frequencies and concluded that to capture 90% of the diurnal variability of SST, 3 hourly flux forcing was required. However Horrocks et al [52] used 6 hourly surface fluxes from the Met Office NWP analysis and converted the solar flux to a finer resolution. This was done by using an integral equation to find a peak insolation value from the 6 hourly means. The peak insolation value was assumed to occur at noon with a smooth variation in time either side of the peak. A similar technique was also used by Hallsworth [50] who used 6 hourly NWP solar fluxes to adjust a clear sky value at a finer resolution. The use of NWP data in diurnal variability modelling is far from ideal, particularly with regards to the 6 hourly mean wind stress, as the diurnal cycle can be extremely sensitive to fine scale wind structure [138]. This limitation has to be accepted; however, we are required to do the best we can within these constraints.

Mixed layer models can easily be set-up to run with a fine near surface vertical grid, needed to capture the diurnal thermocline. In the western Pacific warm pool an upper layer thickness of order 1 metre is required to capture 90% of the diurnal variability [9]. The diurnal variability described in [9] is that obtained from temperature observations measured at a depth of 0.45 metres. Satellite observations measure a much finer near surface; this is why Horrocks et al [52] had a top grid layer thickness of 2 cm, increasing

exponentially to 60 cm at the 60$^{\text{th}}$ layer, when comparing model output to AATSR observations. Hallsworth [50] had a vertical grid with thickness of order centimetres near the surface decreasing to order metres at deeper depths.

Another area of importance for diurnal cycle modelling is the penetration of solar radiation into the ocean (see Section 3.3). In [104] they used a parameterisation by Paulson and Simpson [100] (see Section 3.3). This parameterisation is still widely used in diurnal modelling studies e.g. [9] and [127] in spite of its inappropriateness for accurate representation of diurnal warming, presumably because it is still used in the majority of current climate models. Improvements are, however, made by Horrocks et al [52] who implement the more appropriate 9 band parameterisation [101]. Hallsworth [50] experimented with several parameterisations including decomposing the full spectral range into 278 intervals. However, the absorption of SWR in the upper ocean is highly dependent on classification of water type (see Section 3.3). In [84] C. Donlon and G. Wick recommend that more of a focus on the biological impact of solar penetration should be taken as this is a known issue for strong diurnal variability and modification of the vertical profile. Webster et al [151] implemented a parameterisation of 3 spectral intervals with coefficients determined from the ocean's bio-optical state [89] (see Section 3.3).

1.8   Thesis Aims

The complex interactions across and in the vicinity of the marine boundary layer have been highlighted and a detailed description given of the physical processes at play in the development of the diurnal cycle of SSTs. Although the physics are known in some detail, modelling this non-linear system is still very much in its infancy. Developments in mixed layer models have been seen in recent decades (e.g. [104], [74], [62], and [149]), but rarely has this focused on modelling the diurnal cycle of SSTs (see the above section). As such the first aim of this thesis is to improve and develop modelling capabilities in this area.

Another issue highlighted in this introduction is how satellite observations of SST

represent temperatures at the skin and sub-skin layer which are very much influenced by diurnal stratification, whereas top grid boxes in climate and ocean models represent a temperature at a much deeper depth without any (or a much reduced) diurnal variability. This discrepancy is a concern for weather forecasting, four-dimensional data assimilation, and ocean-atmosphere coupled modelling, and is only beginning to be addressed as illustrated by the recent article of Zeng and Beljaars [158], who develop a prognostic scheme of sea surface skin temperature for modelling and data assimilation. The second aim of the thesis is therefore to provide an accurate bridge between skin and bulk temperatures, and to develop an observation operator for use in the data assimilation process by providing an accurate transformation from observation space to model space.

The difficulty in utilising the wealth of satellite SST observations is not only accounting for errors associated with the diurnal cycle and skin to bulk differences, but deciding how actually to best assimilate the observations into the model. This difficulty emanates from the question of how to sensibly adjust prognostic variables, and how information transfers from the surface into the ocean depths (this is discussed in more detail in Section 5.3). Thus the third aim of this thesis will be to develop novel techniques for making judicious use of available SST data in assimilation.

With an effective model that accurately captures diurnal variability and a data assimilation scheme that maximises the use of information content from the satellite observations, the final aim will be to produce spatial diurnal variability maps. It is hoped these products will provide valuable insights into the global extent and seasonal change in diurnal warming patterns, which, as explained earlier, has been increasingly seen to have importance on longer timescales.

1.9 Thesis Outline

The following is a brief outline of the remainder of the thesis.

Chapter 2 introduces the numerical model that is used throughout this work. A presentation is made of the system equations including turbulence closure and their

numerical discretisation. An outline of previous uses of the model is also given in this chapter.

In Chapter 3 the theory behind the methods for calculating the forcing, needed to drive the model, are described in detail. This includes deriving parameterisations for short-wave radiation, ocean radiant heating, long-wave radiation, and the turbulent air-sea fluxes.

Chapter 4 is the start of the new results. Here findings are presented from initial experiments performed using data from three upper ocean mooring sites. At these sites the model is tested with different air-sea flux algorithms and radiant heating parameterisations. Results are presented at each site. Further scenarios are also tested including changing cloud cover and using a reduced resolution of forcing data.

In Chapter 5 the topic of data assimilation is introduced. Firstly a general data assimilation formulation is derived. Following this, a review of current SST data assimilation techniques and their applications is provided. This chapter then moves on to present novel results gained from exploring various different approaches to the assimilation of SST. These routines were tested using the buoy data sets and a discussion of the success and difficulties involved in this work is presented.

In Chapter 6 the work is extended by using global operational forecast and analysis data to force and initialise the model on a much larger scale. Findings are presented on the sensitivity of the model to various model set-up and input options, and the model is suitably adapted and refined for the purposes of modelling diurnal variability. By comparison to remotely sensed SST observations it is shown how this tailored model can be used as a tool to produce spatial diurnal variability maps, and the significance of these new results are discussed.

Chapter 7 outlines a new data assimilation algorithm which assimilates satellite observations into the modelled diurnal cycle by correcting the forcing data. This algorithm was applied over a wide area using a combination of IR and MW satellite observations. Results produced by this new method are presented and a discussion of the improvements to SST estimation is given.

The final chapter provides a summary of the thesis and draws general conclusions

from the work. Areas for further research that could build on the foundations laid in this thesis are also identified.

Chapter 2

The Model

2.1 Introduction

One-dimensional modelling of the oceanic mixed layer has been widely used in the development of turbulence and air-sea flux parameterisations. Full scale ocean and climate models are computationally expensive and are time consuming to run; thus an advantage of the single column model is the ability to perform multiple model simulations in a relatively short amount of time. The oceanic mixed layer model also has reduced complexity and size which allows the user to become fully acquainted with the model. These characteristics provide the malleable framework for testing parameterisations. One-dimensional mixed layer models are particularly suitable for modelling the diurnal variability of SST because much greater near surface vertical resolution can be achieved compared with larger ocean models where computational limits are apparent. This fine vertical resolution is essential for the ability to capture the diurnal thermocline which is of paramount importance in estimating SST over diurnal time-scales, whereas the horizontal scales of three-dimensional ocean models are of limited importance in the development of the diurnal cycle of SST.

Vertical exchange processes across the air-sea boundary, as well as vertical mixing within the water column, are likely to affect the local conditions much more rapidly and effectively than horizontal advection and horizontal mixing [93]. This is the assumption adopted when using a one-dimensional model where horizontal gradients are

not considered.

Ocean mixed layer modelling can generally be categorised into two broad approaches: bulk and diffusion. Bulk models attempt to model the mixed layer in an integral sense (e.g. [72] and [104]). The governing equations of heat and momentum are integrated over the mixed layer and the balance of heat and momentum over the entire mixed layer is adjusted by the effects of momentum and buoyancy fluxes. On the other hand diffusion models directly parameterise the turbulent mixing and diffusion in the mixed layer (e.g. [83], [74], and [62]).

For this thesis a diffusion type model called the General Ocean Turbulence Model (GOTM) was chosen. This model is freely available for download together with documentation at [85]. Originally published in 1999 [15] it has been regularly extended since then [149].

2.2 System Equations

The system equations consist of PDEs for momentum (a 1-D approximation to the Navier-Stokes equation), heat, and salinity (1-D diffusion equations) combined with a 2-equation turbulence model. The state variables: horizontal sea water velocities, $\boldsymbol{v} = (u, v)^T$; potential sea temperature, θ; and salinity, S are all assumed to be horizontally homogeneous. The system equations are as follows

$$\frac{\partial \boldsymbol{v}}{\partial t} = \frac{\partial}{\partial z} \left((\nu_t + \nu^m) \frac{\partial \boldsymbol{v}}{\partial z} \right) - C_f \boldsymbol{v} \sqrt{u^2 + v^2}, \tag{2.1}$$

$$\frac{\partial \theta}{\partial t} = \frac{\partial}{\partial z} \left((\nu_t' + \nu^\theta) \frac{\partial \theta}{\partial z} \right) + \frac{1}{c_p \rho_0} \frac{\partial I}{\partial z}, \tag{2.2}$$

$$\frac{\partial S}{\partial t} = \frac{\partial}{\partial z} \left((\nu_t' + \nu^S) \frac{\partial S}{\partial z} \right), \tag{2.3}$$

with initial conditions

$$\boldsymbol{v}(0) = \boldsymbol{v}_0, \tag{2.4}$$

$$\theta(0) = \theta_0, \tag{2.5}$$

$$S(0) = S_0, \tag{2.6}$$

18

and Neumann type (flux) surface and benthic boundary conditions

$$\left(\nu_t + \nu^m\right) \frac{\partial \boldsymbol{v}}{\partial z} = \frac{1}{\rho_0}\boldsymbol{\tau} \quad \text{at} \quad z = 0 \qquad \text{and} \qquad \left(\nu_t + \nu\right)\frac{\partial \boldsymbol{v}}{\partial z} = 0 \quad \text{at} \quad z = -H, \quad (2.7)$$

$$\left(\nu_t' + \nu^\theta\right) \frac{\partial \theta}{\partial z} = \frac{1}{c_p\rho_0}Q \quad \text{at} \quad z = 0 \qquad \text{and} \qquad \left(\nu_t' + \nu^\theta\right)\frac{\partial \theta}{\partial z} = 0 \quad \text{at} \quad z = -H, \quad (2.8)$$

$$\left(\nu_t' + \nu^S\right) \frac{\partial S}{\partial z} = 0 \quad \text{at} \quad z = 0 \qquad \text{and} \qquad \left(\nu_t' + \nu^S\right)\frac{\partial S}{\partial z} = 0 \quad \text{at} \quad z = -H. \quad (2.9)$$

The first terms on the right hand sides of equations (2.1), (2.2), and (2.3) generate the mixing. Fixed values have been prescribed for the molecular diffusivities of momentum, heat, and salt denoted ν^m, ν^θ, and ν^S respectively. The computation of the turbulence diffusivity parameters ν_t and ν_t' is discussed in Section 2.3.

Bottom friction is treated implicitly using the second term on the right hand side of equation (2.1).

The source term in equation (2.2) and the surface boundary conditions (2.7) and (2.8) are discussed in detail in Chapter 3. The reference sea water density ($1025\,\text{kgm}^{-3}$) is denoted ρ_0 and the specific heat capacity of sea water at constant pressure is denoted c_p and taken to be $3994\,\text{Jkg}^{-1}\text{K}^{-1}$.

2.3 Turbulence Closure

2.3.1 Introduction

The Oxford Concise Science Dictionary [54] defines turbulence as:

> *A form of fluid flow in which the particles of the fluid move in a disordered manner in irregular paths, resulting in an exchange of momentum from one portion of a fluid to another.*

A measure of turbulence in a fluid is the Reynolds number

$$Re = \frac{Ul}{\nu} \tag{2.10}$$

where U is the mean fluid velocity, l a characteristic length scale, and ν is the kinematic fluid viscosity. In high Reynolds number regimes, irregular and ephemeral closed flow

structures arise called eddies. Eddy motion is complex and the details little understood, however stochastic average properties of the flow (averages over many realisations in statistical theory) can be formulated [145].

2.3.2 Turbulent Kinetic Energy (TKE)

To complete closure of equations (2.1), (2.2), and (2.3) we need to compute the turbulence parameters ν_t and ν_t'. As described in [145], these can be expressed as

$$\nu_t = c_\mu k^{\frac{1}{2}} l, \tag{2.11}$$

where k is the turbulent kinetic energy, l is a typical length scale, and c_μ is a stability function (replace c_μ with c_μ' for computing ν_t'). We employ a so-called 2-equation model, whereby both k and l are computed from partial differential equations. The turbulent kinetic energy transport equation, known as the k-ϵ equation is written as

$$\frac{\partial k}{\partial t} = \frac{\partial}{\partial z}\left(\frac{\nu_t}{\sigma_k}\frac{\partial k}{\partial z}\right) + P + B - \epsilon, \tag{2.12}$$

where P is the production of k by mean shear,

$$P = \nu_t \left(\frac{\partial^2 u}{\partial z^2} + \frac{\partial^2 v}{\partial z^2}\right), \tag{2.13}$$

and B is the production of k by buoyancy given by

$$B = g\alpha\nu_t'\frac{\partial\theta}{\partial z}. \tag{2.14}$$

The length scale equation is formulated via the related length scale determining variable ϵ, the rate of dissipation, which is obtained by solving

$$\frac{\partial\epsilon}{\partial t} = \frac{\partial}{\partial z}\left(\frac{\nu_t}{\sigma_\epsilon}\frac{\partial\epsilon}{\partial z}\right) + \frac{\epsilon}{k}\left(c_{\epsilon_1}P + c_{\epsilon_3}B - c_{\epsilon_2}\epsilon\right). \tag{2.15}$$

The length scale is then computed from

$$l = \left(c_\mu^0\right)^3 \frac{k^{\frac{3}{2}}}{\epsilon}. \tag{2.16}$$

This follows the model of Rodi [115] who used constants $c_\mu^0 = 0.5577$, $\sigma_k = 1.0$ (the Schmidt number for k), $\sigma_\epsilon = 1.3$ (the Schmidt number for ϵ), $c_{\epsilon_1} = 1.44$, $c_{\epsilon_2} = 1.92$, and c_{ϵ_3} is 1.0 for unstable stratification and 0.035 for stable stratification. For a more detailed description of the turbulent closure scheme and the solution procedure refer to [147] and [149].

2.3.3 Wave Breaking

The k–ϵ 2-equation turbulence model has been modified such that the analytical concept of a wave-enhanced layer located on top of the classical law-of-the-wall layer is reproduced. This follows work by Craig and Banner [24] who suggested modelling the flux of TKE due to breaking waves into the water column as proportional to the cube of the surface friction velocity. In order to implement this parameterisation into the k–ϵ 2-equation turbulence model, Burchard [11] modified two features of the dissipation rate equation for ϵ: the surface boundary condition and the turbulent Schmidt number σ_ϵ. It should be noted that wave breaking should only be used in conjunction with near surface resolution of O(cm), and that the physics of this region of complex dynamics is still in its infancy. The use of this option was tested in Section 6.5.1.

2.3.4 Internal Wave Mixing

Internal wave mixing is another area where the physics is not adequately understood enough to confidently parameterise. In this model we follow the suggestion of Kantha and Clayson [62] who imposed eddy viscosity and diffusivity characteristic of internal wave activity and shear instability when there is extinction of turbulence.

2.4 Grid

For the purposes of this study we construct a non-uniform grid for GOTM which consists of 150 vertical levels resolving a depth down to 150 metres. This grid has much finer spacing near the surface in order to resolve the diurnal thermocline. The top temperature represents a mean value over a grid box of 0.030 metres thickness, whereas the bottom temperature represents a mean value over a grid box with thickness 3.015 metres. This grid zooming is applied according to the formula

$$h_i = 150\frac{\tanh\left(\frac{i}{50}\right) - \tanh\left(\frac{i-1}{50}\right)}{\tanh(3)}, \tag{2.17}$$

where h_i represents the thickness of the ith layer as illustrated in Figure 2.1. This grid distribution results in 67 model layers within the top 10 metres of ocean.
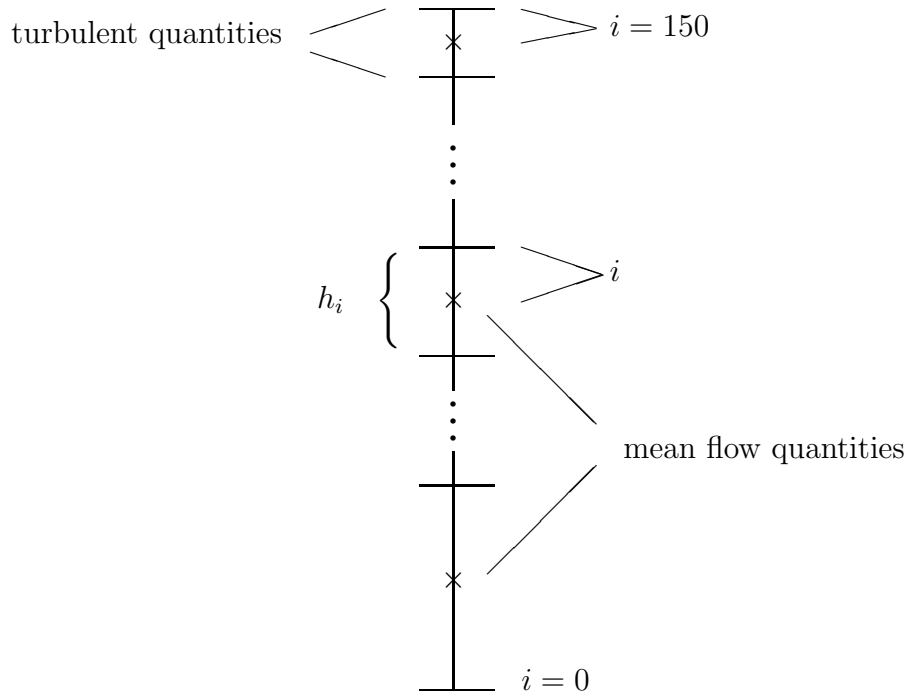
Figure 2.1: *A sketch of the model grid made up of 150 non-uniform layers.*

2.5   Numerics

Equations ((2.1), (2.4), and (2.7)), ((2.2), (2.5), and (2.8)), and ((2.3), (2.6), and (2.9)) can essentially be written in the form of a simple diffusion equation with Neumann boundary conditions:

$$\frac{\partial X}{\partial t} = \frac{\partial}{\partial z}\left(\nu \frac{\partial X}{\partial z}\right), \tag{2.18}$$

$$\nu \frac{\partial X}{\partial z} = F_s \qquad \text{for} \quad z = 0, \tag{2.19}$$

$$\nu \frac{\partial X}{\partial z} = F_b \qquad \text{for} \quad z = -H. \tag{2.20}$$

These equations are discretised semi-implicitly using the θ-method

$$\frac{X_{150}^{n+1} - X_{150}^{n}}{\Delta t} = \frac{F_s - \nu_{149}^{n}\left(\frac{X_{150}^{n+\theta} - X_{149}^{n+\theta}}{\frac{1}{2}(h_{150}+h_{149})}\right)}{h_{150}}, \tag{2.21}$$

$$\frac{X_i^{n+1} - X_i^n}{\Delta t} = \frac{\nu_i^n \left(\frac{X_{i+1}^{n+\theta} - X_i^{n+\theta}}{\frac{1}{2}(h_{i+1}+h_i)} \right) - \nu_{i-1}^n \left(\frac{X_i^{n+\theta} - X_{i-1}^{n+\theta}}{\frac{1}{2}(h_i+h_{i-1})} \right)}{h_i}, \qquad (2.22)$$

$$\frac{X_1^{n+1} - X_1^n}{\Delta t} = \frac{\nu_1^n \left(\frac{X_2^{n+\theta} - X_1^{n+\theta}}{\frac{1}{2}(h_2+h_1)} \right) - F_b}{h_1}, \qquad (2.23)$$

for $1 < i < 150$, where the layer thickness h_i is given in Equation (2.17). The semi-implicit time level is defined by

$$X^{n+\theta} = \theta X^{n+1} + (1 - \theta)X^n. \qquad (2.24)$$

The value of θ is chosen to be 0.6 which is slightly more implicit than the Crank and Nicolson scheme [25], in order to obtain asymptotic stability. Because of the implicit treatment of vertical diffusion and the absence of advection there are no limitations by Courant numbers. The resulting linear system of equations (2.21) – (2.23) has a tri-diagonal matrix structure which is solved by means of the Thomas algorithm (a simplified Gaussian elimination).

The numerical discretisation of equations (2.12) and (2.15) are slightly different from those above, due to the constraint that turbulent quantities are generally non-negative. Equations (2.12) and (2.15) can be written in the simple form,

$$\frac{\partial X}{\partial t} = P - QX, \quad P, Q > 0, \qquad (2.25)$$

with X denoting a non-negative quantity, P a non-negative source term, QX a non-negative linear sink term, and t denoting time. P and Q depend on X and t. A simple discretisation of (2.25) would be

$$\frac{X^{n+1} - X^n}{\Delta t} = P^n - Q^n X^n, \qquad (2.26)$$

which to keep the solution positive would require an unreasonable time step restriction of

$$\Delta t < \frac{X^n}{X^n Q^n - P^n}. \qquad (2.27)$$

Therefore a quasi-implicit numerical procedure [99] is applied

$$\frac{X^{n+1} - X^n}{\Delta t} = P^n - Q^n X^{n+1}, \qquad (2.28)$$

which always yields a non-negative solution for X^{n+1}

$$X^{n+1} = \frac{X^n + \Delta t P^n}{1 + \Delta t Q^n}.$$ (2.29)

The mean flow variables u, v, θ, and S are located at the centre of vertical layers as they represent interval means, whereas the turbulent quantities k, ϵ, l, P, and B are positioned on the grid layer interfaces, see Figure 2.1.

2.6 Model Validation

GOTM has been utilised as a research tool for the scientific community with many published test cases and results [86]. GOTM has been widely used as a platform for the study of turbulence [12], [147], and [148], and has been developed for various applications including biogeochemical modelling [13] and [1]. It has been used as the basis for a variety of different process and case studies including [108], [133], [16], and [14]. Most relevant to this thesis is the work of S. Hallsworth [50] who has recently utilised GOTM specifically for the purpose of modelling the diurnal variability of SST (see Section 1.7).

Chapter 3

The Forcing

3.1 Introduction

The dynamic coupling of oceanic and atmospheric processes is inextricably linked to the fluxes across the marine boundary layer. Knowledge of their variability on different space-time scales is therefore crucial for understanding ocean-atmosphere interaction. Thermodynamic interactions across the air-sea interface are complex and varied. The sea surface receives short-wave solar radiation of which an amount is reflected while the remainder penetrates into the oceanic surface layer. Long-wave radiation is emitted from the ocean surface into the atmosphere, as well as from the atmosphere into the ocean surface. Alongside the radiative transfers, are sensible and latent heat transfer. Sensible heat raises or lowers air temperature by conduction. The larger component is the latent heat transfer due to evaporation. Momentum transfer is also in operation generated as the winds blow across the air-sea interface.

3.2 Short-wave Radiation

Short-wave radiation (SWR) is considered as the radiation whose source is the sun, and is comprised of a spectrum of wavelengths. The down-welling SWR at the sea surface, otherwise known as the surface insolation, can be obtained from measured observations using a pyranometer, prescribed from operational analyses, or calculated

as follows. The surface insolation under clear skies may be split into a direct and diffuse component

$$I_\downarrow = I_{\text{dir}} + I_{\text{diff}}. \tag{3.1}$$

These components are then calculated following the approach of Rosati and Miyakoda [116]. The direct component is written as

$$I_{\text{dir}} = S_0 \cos(\omega) \tau^{\sec(\omega)}, \tag{3.2}$$

where S_0 denotes the solar constant estimated to be around $1370\,\text{Wm}^{-2}$, and ω is the solar zenith angle (the angle measured at the earth's surface between the sun and the zenith). The cosine of the solar zenith angle can be written as

$$\cos(\omega) = \sin(\phi)\sin(\delta) + \cos(\phi)\cos(\delta)\cos(h), \tag{3.3}$$

where ϕ denotes latitude, δ denotes the sun declination angle (the angle between the Earth-sun line and the equatorial plane), and h denotes the sun's hour angle (which is the angular distance, expressed in hours, minutes, and seconds (one hour equals 15 degrees), measured westward along the celestial equator from the observer's celestial meridian to the hour circle of the object being located). Finally τ (in Equation (3.2)) denotes the atmospheric transmission coefficient which represents the attenuation of I_{dir} by the atmosphere and is set at 0.7. The diffuse clear sky radiation has been approximated by

$$I_{\text{diff}} = \left((1 - A_a)S_0\cos(\omega) - I_{\text{dir}}\right)/2. \tag{3.4}$$

This says that when scattering occurs, half is scattered downward and the other half back. A_a represents water vapour and ozone absorption taken to be 0.09. Next a modification to $I_\downarrow$ due to cloud cover is needed. A comparative study of these methods by Dobson and Smith [31] found that the Reed formula [109] gave the best long-term mean insolation values. The Reed formula has been widely used in the oceanographic community and is surprisingly accurate for such a simple expression [97]. The Reed formula is as follows

$$I_0 = I_\downarrow\left(1 - C_n n + 0.0019\beta\right)\left(1 - \alpha\right), \tag{3.5}$$

where n is the fractional cloud cover, c_n the cloud cover coefficient set as 0.62, β the solar noon angle, and α the albedo calculated as a function of sun altitude as described by Payne [102]. This formula is used only for $0.3 \leq n \leq 1$, with $I_0 = I_\downarrow (1 - \alpha)$ otherwise, [43].

Numerous studies have evaluated the accuracy of Equation (3.5) (e.g. [31], [120], and [70]) finding small, but different, regional biases and generally supporting its use for long time average insolation over the sea. Calibration based on radiometric measurements can improve the accuracy of the formula for particular regions. For example this was done by Schiano [120] over the Mediterranean Sea where the transmission coefficient, τ, was reduced from 0.7 to 0.66 due to a regional misevaluation of aerosols and water vapour attenuation. Schiano also showed how the coefficient A_a could vary according to measured water vapour density. This was only done in the clear sky case indicating an error not in the cloud correction of Reed, but the transmission coefficient originally chosen by Seckel and Beaudry [122]. A correction using an inverse method and direct ocean transport estimates by Isemer et al [55] over the North Atlantic Ocean also slightly reduced the transmission coefficient from 0.7 to 0.69 but also increased the cloud cover coefficient, C_n, from 0.62 to 0.636. However an empirical formula such as this cannot be universally calibrated and its accuracy will always be restricted because the surface insolation is determined by not only the portion of cloud cover, but also the optical thickness of the cloud, which varies widely under the same cloud amount.

3.3 Oceanic Radiant Heating

In the Heat Equation (2.2) we have a source term which is known as the radiant heating rate

$$\frac{1}{c_p \rho} \frac{\partial I}{\partial z}, \tag{3.6}$$

where

$$I = I_0 f(z), \tag{3.7}$$

I_0 is the total net flux of surface solar radiation and $f(z)$ is the solar transmission which describes the change in solar flux with depth. Solar transmission gives the fraction of

the incident surface irradiance that exists at depth. This can be parameterised as a sum of exponentials

$$f(z) = \sum_{i=1}^{n} A_i \exp\left(-K_i z\right).$$ (3.8)

The difficulty in modelling radiant heating comes from determining the coefficients A_i and exponents K_i as well as how and why they vary. The most widely used approach is that of Paulson and Simpson [100] who separated light into two distinct wave-band groups (red light and visible blue/green light) to account for their different attenuation lengths. This two band parameterisation has a first term which characterises the rapid attenuation of light in the upper 5 m due to absorption of the long-wave (red) spectral components while the absorption of visible (blue/green) spectral components below a depth of 10 m is characterised by the second term. The coefficient and exponent values are determined empirically as a function of the Jerlov water type [57] (a classification of six different water types with increasing turbidity). This technique was extended by Paulson and Simpson [101] to the full spectral range including the near-infrared, which can be a significant fraction of the total irradiance. They derived parameters for nine wave-band groups based on pure water data and noted improvements in the radiant heating over previous parameterisations. More recently with the advent of ocean colour sensors in space such as SeaWiFS (Sea-viewing Wide Field-of-view Sensor) more sophisticated solar transmission parameterisations have been developed. These parameterisations, for example by Morel and Antoine [89] and Ohlmann and Siegel [95], allow for variations in parameters based on remotely sensed data of chlorophyll-a pigments in phytoplankton which are the dominant attenuators of visible energy in oligotrophic open ocean waters [130], [88].

3.4   Long-wave Radiation

Long-wave Radiation (LWR), denoted by Q_B, is considered as radiation whose source is the emission of thermal infrared by atmosphere and sea surface. The net LWR is split into down-welling and up-welling components. The down-welling radiation originates from the emission by atmospheric gases (mainly water vapour, carbon dioxide, and

28

ozone), aerosols, and clouds. The up-welling radiation is emission from the sea surface, depending on surface emissivity and θ_{skin}, augmented by a small contribution due to reflection of the down-welling LWR. Therefore we have

$$Q_B = \epsilon\sigma\theta_{\text{skin}}^4 - (1 - \alpha_L)\,Q_B^{\downarrow}. \tag{3.9}$$

The largest component is the up-welling part, which is most accurately computed using the Stefan-Boltzmann Law, $(\epsilon\sigma\theta_{\text{skin}}^4)$ where ϵ is the surface emissivity taken to be 0.98, σ is the Stefan-Boltzmann constant $(5.67 \times 10^{-8}\,\text{Wm}^{-2}\text{K}^{-4})$, and α_L is the long-wave reflectivity taken to be 0.045. To compute the LWR either measured observations of $Q_B^{\downarrow}$ (the down-welling component) from a pyrgeometer can be used, or Q_B can be obtained from operational analyses. Alternatively the LWR can be parameterised; in GOTM a formula by Clark is used [21]:

$$Q_B = \epsilon\sigma\theta_{\text{skin}}^4(0.39 - 0.05e^{0.5})(1 - \lambda_n n^2) + 4\epsilon\sigma\theta_{\text{skin}}^3(\theta_{\text{skin}} - T_a), \tag{3.10}$$

where e is the water vapour pressure in surface air with units of millibars, n is the fractional cloud cover, T_a the air temperature in Kelvin and λ_n is a latitude dependent cloud cover coefficient. Many other parameterisations are also in existence but, a review by Katsaros [65] found Equation (3.10) to be most accurate with a bias of only $-5.5\,\text{Wm}^{-2}$. More recent parameterisations by Bignami [10] and Josey [58] have been shown to be more accurate but only in certain areas e.g. the Mediterranean and mid-high latitudes respectively.

3.5   Turbulent Fluxes

3.5.1   Introduction

The turbulent fluxes consist of the latent and sensible heat fluxes and the two components of the wind stress. The turbulent fluxes are extremely difficult to measure and so are computed from parameterisations using readily available basic variables such as wind speed and air temperature.

3.5.2 Reynolds Averages

This is a technique that allows us to decompose a flow into components of means and fluctuations. For example a meteorological variable x can be split into components $\overline{x}$, representing a time or spatial average and x', a fluctuating part about that mean, so that $x = \overline{x} + x'$.

A conservation equation for the ensemble mean of variable x, denoted as X, is

$$\frac{\partial X}{\partial t} = -\nabla_h X \cdot U_h - \frac{\partial(\overline{w'x'})}{\partial z} + \overline{I_x}, \qquad (3.11)$$

where the subscript h denotes horizontal components and I_x is the source term. In brackets we have a Reynolds flux $\overline{w'x'}$ defined by the Reynolds averages described above.

3.5.3 Observations

Direct observation of a Reynolds flux can be achieved via two separate instruments at a single level, recording continuous high resolution time series of w' and x'. This is not easy and measurements at sea have particular difficulties related to salt and sea spray, ship motion, and air-flow distortion. A less direct technique for observing fluxes called inertial dissipation (see [38]) has also been developed. However, because these observations require great care and attention and are not routine, surface fluxes for numerical models are calculated indirectly using the so called bulk formulae described next.

3.5.4 Monin-Obukhov Similarity Theory (MOST)

The Reynolds flux can be computed by an application of MOST. This is a method to superpose the effects of two types of forcings, first described by Monin and Obukhov [87]. A surface flux can be represented by mean quantities of measured atmospheric properties. For instance, continuing the example of the conservation equation, (3.11) above, we now introduce the scaling parameter $x_* = \overline{w'x'}$, which is based upon mean quantities $x_* = C_x U \Delta X$. Here ΔX is the air-sea difference in the mean value of x, U is the mean wind speed, and C_x the transfer coefficient.

3.5.5 Bulk Formula

Using the above theory, we are now able to express our turbulent fluxes for wind stress $\boldsymbol{\tau} = (\tau_x, \tau_y)^T$, latent heat Q_E, and sensible heat Q_H as follows,

$$\boldsymbol{\tau} = \rho_a \overline{w' \boldsymbol{u}'} = -\rho_a |\boldsymbol{u}_*| \boldsymbol{u}_*, \tag{3.12}$$

$$Q_E = \rho_a L_v \overline{w' q'} = -\rho_a L_v |\boldsymbol{u}_*| q_*, \tag{3.13}$$

$$Q_H = \rho_a c_{pa} \overline{w' T'} = -\rho_a c_{pa} |\boldsymbol{u}_*| T_*. \tag{3.14}$$

Here w', T', q', and $\boldsymbol{u}'$ represent the turbulent fluctuations of vertical wind, temperature, water vapour mixing ratio, and the horizontal wind components $\boldsymbol{u} = (u, v)^T$ respectively; and $\boldsymbol{u}_*$, q_* and T_* are the related Monin-Obukhov similarity scaling parameters.

The standard bulk expressions for the fluxes are then written as

$$\boldsymbol{\tau} = \rho_a C_D \left(|\boldsymbol{u}(h_u)| - |\boldsymbol{v_s}| \right) \left(\boldsymbol{u}(h_u) - \boldsymbol{v_s} \right), \tag{3.15}$$

$$Q_E = \rho_a L_v C_E \left(|\boldsymbol{u}(h_u)| - |\boldsymbol{v_s}| \right) \left(q(h_q) - q_s \right), \tag{3.16}$$

$$Q_H = \rho_a c_{pa} C_H \left(|\boldsymbol{u}(h_u)| - |\boldsymbol{v_s}| \right) \left(T_a(h_T) - \theta_{\text{skin}} \right). \tag{3.17}$$

The functions C_D, C_E, and C_H are known as the transfer coefficients; $\boldsymbol{u}(h_u)$, $q(h_q)$, and $T_a(h_T)$ are the observed wind velocities, water vapour mixing ratio (obtained from observed relative or specific humidity), and observed air temperature at measurement heights h_i; $\boldsymbol{v_s}$, q_s, and θ_{skin} are the surface values; and L_v is the latent heat of vaporisation.

3.5.6 Transfer Coefficients

To derive equations for the transfer coefficients we start with the dimensionless profile equations

$$\frac{\kappa h}{\boldsymbol{u}_*} \frac{\partial < \boldsymbol{u} >}{\partial h} = \phi_m, \tag{3.18}$$

$$\frac{\kappa h}{q_*} \frac{\partial < q >}{\partial h} = \phi_q, \tag{3.19}$$

$$\frac{\kappa h}{T_*}\frac{\partial <T_a>}{\partial h} = \phi_T. \tag{3.20}$$

The quantities in angular brackets represent mean values in time, κ denotes the von Karman constant, and ϕ_i are functions of the stability parameter $\zeta = h/L$, where L is the Monin-Obukhov length defined as

$$L = \frac{T_v|\boldsymbol{u_*}|^3}{g\kappa\langle w'T_v'\rangle}, \tag{3.21}$$

T_v denotes the virtual air temperature and h the height above the surface. Integrating (3.18) – (3.20) from the surface to the measurement height gives

$$\boldsymbol{u}(h_u) = \boldsymbol{u_s} + \frac{\boldsymbol{u_*}}{\kappa}\left[\ln\left(\frac{h_u}{z_0}\right) - \Psi_m\right], \tag{3.22}$$

$$q(h_q) = q_s + \frac{q_*}{\kappa}\left[\ln\left(\frac{h_q}{z_{0q}}\right) - \Psi_q\right], \tag{3.23}$$

$$T_a(h_T) = \theta_{\text{skin}} + \frac{T_*}{\kappa}\left[\ln\left(\frac{h_T}{z_{0T}}\right) - \Psi_T\right], \tag{3.24}$$

where the functions Ψ_i (the integrals of ϕ_i) are stability corrections to the profile. The quantities z_0, z_{0q}, and z_{0T} are the roughness lengths (the heights at which the extrapolation of the logarithmic profiles reach the respective surface value under neutral conditions, see [98] or [73] for discussions on this topic).

Therefore using equations (3.22) – (3.24) together with equations (3.15) – (3.17) the transfer coefficients can be written as

$$C_D = \kappa^2\left[\ln\left(\frac{h_u}{z_0}\right) - \Psi_m\right]^{-2}, \tag{3.25}$$

$$C_E = \kappa^2\left[\ln\left(\frac{h_q}{z_{0q}}\right) - \Psi_q\right]^{-1}\left[\ln\left(\frac{h_u}{z_0}\right) - \Psi_m\right]^{-1}, \tag{3.26}$$

$$C_H = \kappa^2\left[\ln\left(\frac{h_T}{z_{0T}}\right) - \Psi_T\right]^{-1}\left[\ln\left(\frac{h_u}{z_0}\right) - \Psi_m\right]^{-1}. \tag{3.27}$$

This complex system of equations essentially provides surfaces in $\boldsymbol{u_*}$, q_*, and T_* for given quantities $(\boldsymbol{u}(h_u) - \boldsymbol{v_s})$, $(q(h_q) - q_s)$, and $(T_a(h_T) - \theta_{\text{skin}})$. The triplet $(\boldsymbol{u_*}, q_*, T_*)$ chosen for computing the fluxes in equations (3.12) – (3.14) will be the intersection of these surfaces.

3.5.7   Kondo

Deriving parameterisations to calculate air-sea fluxes is very difficult. Many approximations are needed and much of the physics is not well understood. A plethora of different approaches have been developed and implemented over the years. A good reference guide to many of the methods is presented in [97]. In the public domain version of GOTM the method of Kondo [71] is used. In this method the transfer coefficients under neutral conditions are approximated by a quadratic function of the 10 metre wind speeds. These are then used together with an approximate stability formula to find the transfer coefficients proper. Much advancement in the science of parameterising turbulent fluxes has been achieved since Kondo's publication. Therefore we implemented a more recent and advanced algorithm (see Section 3.5.8 below) into GOTM.

3.5.8   TOGA-COARE Algorithm

A newer scheme devised and updated by Fairall et al, ([37] and [36]) for the TOGA COARE region has been found to be accurate within 5% for wind speeds of 0–$10\,\mathrm{m\,s^{-1}}$ [36], and is considered state-of-the-art. This scheme was studied and implemented into GOTM as an alternative to Kondo.

The algorithm is based on the Liu-Katsaros-Businger [76] method with the added sophistication of a skin SST [35], (the true interface temperature), and a gustiness velocity factor to account for sub-grid scale variability.

The transfer coefficients are computed using an iterative cycle where scaling parameters and stability functions are estimated and then re-estimated in a loop until convergence. Figure 3.1 is a scatter plot of the computed drag coefficient, C_D, as a function of wind speed for a data set used in this thesis. It has a minimum of about 1.25×10^{-3} at $3\,\mathrm{m\,s^{-1}}$ then increases rapidly for lower winds to about 2×10^{-3}, and then increases more gently to over 2×10^{-3} for winds of up to $15\,\mathrm{m\,s^{-1}}$. The other transfer coefficients show a similar pattern.
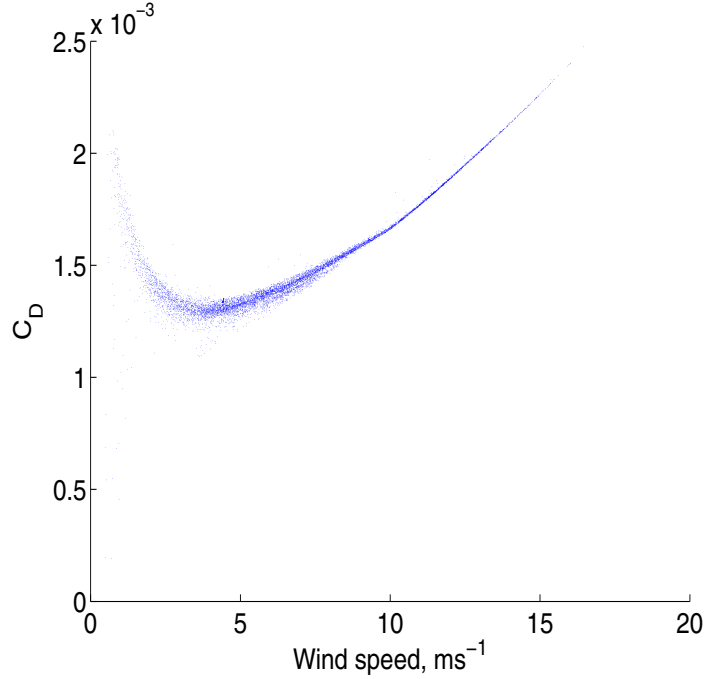
Figure 3.1: *A scatter plot of the drag coefficient, C_D versus wind speed.*

3.5.9 Cool Skin Effect

As defined in Chapter 1 the skin temperature, θ_{skin}, represents the sea temperature in the molecular boundary layer which is typically a few tenths of a degree cooler than θ_{subskin} (the temperature just below the molecular boundary layer) [113]. This is a result of vertical heat flux through the air-sea interface. As the intact sea surface inhibits turbulent motion, heat transport occurs through molecular conduction which, being small, leads to large temperature gradients [113]. Molecular conduction is the basis of the Saunders model [119] which describes a cool-skin temperature change ΔT confined to a region of thickness δ

$$\Delta T = \frac{Q_N \delta}{k}, \tag{3.28}$$

where Q_N is the net heat flux and k is the thermal conductivity of sea water. From dimensional arguments, Saunders assumed that δ is given by

$$\delta = \frac{\lambda \nu}{u_*}, \tag{3.29}$$

where λ is an empirical coefficient, ν is the kinematic viscosity of water, and u_* is the friction velocity of the water. The difficulty comes in estimating λ. Saunders initially estimated a value between 5 and 10. More recently Fairall et al [35] developed a λ with a dependence on wind speed including a smooth transition from a shear-driven to a free convection regime as wind speeds asymptote to zero. The skin temperature represents the true interfacial temperature at which heat exchange between the ocean and atmosphere occurs, and thus its inclusion in air-sea flux algorithms was an important development [35]. This cool skin parameterisation is used in the TOGA COARE air-sea flux algorithm described above.

Chapter 4

GOTM Experiments Without Assimilation

4.1 Introduction

In this chapter the mixed layer ocean model GOTM is developed for the purpose of modelling the diurnal variability of SSTs. The ability of the model to capture the evolution of the upper ocean with particular emphasis on the SST is tested using data from various intensively observed upper ocean mooring sites. At these sites the observed meteorological data is required to force the model and the observed sea temperatures are used for initialisation. Various comparisons are made between the modelled sea temperature output and the sea temperature observations to demonstrate the credibility of the model. In order to maximise the potential of the model to accurately capture the diurnal variability of SST the sensitivity of the model with regards to various set-up options are examined. This includes choosing the best suited air-sea flux and ocean radiant heating parameterisations. An account of the sensitivity of SST estimates and diurnal variability to a reduction in the frequency of available forcing data as well as changes in cloud cover are also presented.

4.2 Mooring Sites

Meteorological and sea temperature observations are obtained from the Woods Hole Oceanographic Institute (WHOI) upper ocean mooring data archive; this is publicly available at [5]. Work presented here uses time series from three of these deployments. Details of the locations, duration, and frequency of data for each time series is given in Table 4.1. The meteorological variables consist of the wind speed components u and v, air temperature T_a, relative humidity q_{rh}, and air pressure p. These variables are needed in the air-sea flux parameterisations (see Section 3.5). The sea temperature observations, $\theta^{obs}(z)$, at various depths z (within the top $150\,\mathrm{m}$ there are 29 observation depths at Arabian Sea, 34 at COARE, and 12 at Subduction) are linearly interpolated onto the model grid and are used to initialise the model simulations. The observed temperature time series are further used to assess how well the model performs by making model-observation comparisons.

Sites	Location	Duration	Frequency
Arabian Sea	15 °N 61 °E	17/10/94 – 17/10/95	$\theta^{obs}(z)$ every 15 min u, v, T_a, q_{rh}, and p every 7.5 min
COARE	1 °S 156 °E	01/11/92 – 01/03/93	$\theta^{obs}(z)$ every 15 min u, v, T_a, q_{rh}, and p every 7.5 min
Subduction	26 °N 29 °W	24/06/91 – 16/06/93	$\theta^{obs}(z)$ every 15 min u, v, T_a, q_{rh}, and p every 15 min

Table 4.1: *Locations, deployment duration, and data frequency at the three mooring sites.*

COARE

The Tropical Ocean Global Atmosphere Coupled Ocean Atmosphere Response Experiment (TOGA COARE) was conceived in order to improve understanding of the principal processes responsible for coupling of the ocean and atmosphere in the western tropical Pacific warm pool region. The COARE field program included a wide variety

of platforms and sensors. A surface mooring was deployed during the COARE intensive observation period for the determination of surface fluxes and upper ocean structure near the centre of the warm pool [154]. This warm pool region has been under intense scrutiny because of its importance in world climate [152]; over a decade of work has greatly increased our understanding of this region [44]. One dimensional mixed layer models using this data have contributed to several of these studies e.g. [151], [2], and [128].

Arabian Sea Site

A moored array was deployed in the Arabian Sea in order to improve understanding of air-sea interaction in the region, and in particular to investigate the oceanic response to the strong, large-scale atmospheric forcing associated with the summer and winter monsoons. A full account of the Arabian Sea data set is given by Weller et al [155]. The Arabian Sea has two monsoon periods, the Northeast Monsoon, characterized by moderate wind speeds, clear skies, and comparatively dry air from early November to mid-February, and the Southwest Monsoon, characterized by strong wind speeds, cloudy skies, and moist air from early June to mid-September. Air and sea temperatures show two periods of cooling coincident with the monsoon seasons. Figure 4.1 shows the time series for wind speed, air and sea temperature, and relative humidity, where these characteristics can clearly be seen.

Subduction Experiment Region

Located in the sub-tropical Atlantic Ocean, this is a preferred region for convergence of the wind-driven (Ekman) circulation which leads to subduction, a process by which mixed layer water is injected into the main thermocline. The data set is compared with climatological and global model products by Moyer and Weller [90]. This deployment had an array of five moorings, in this thesis only data from the central buoy is used.
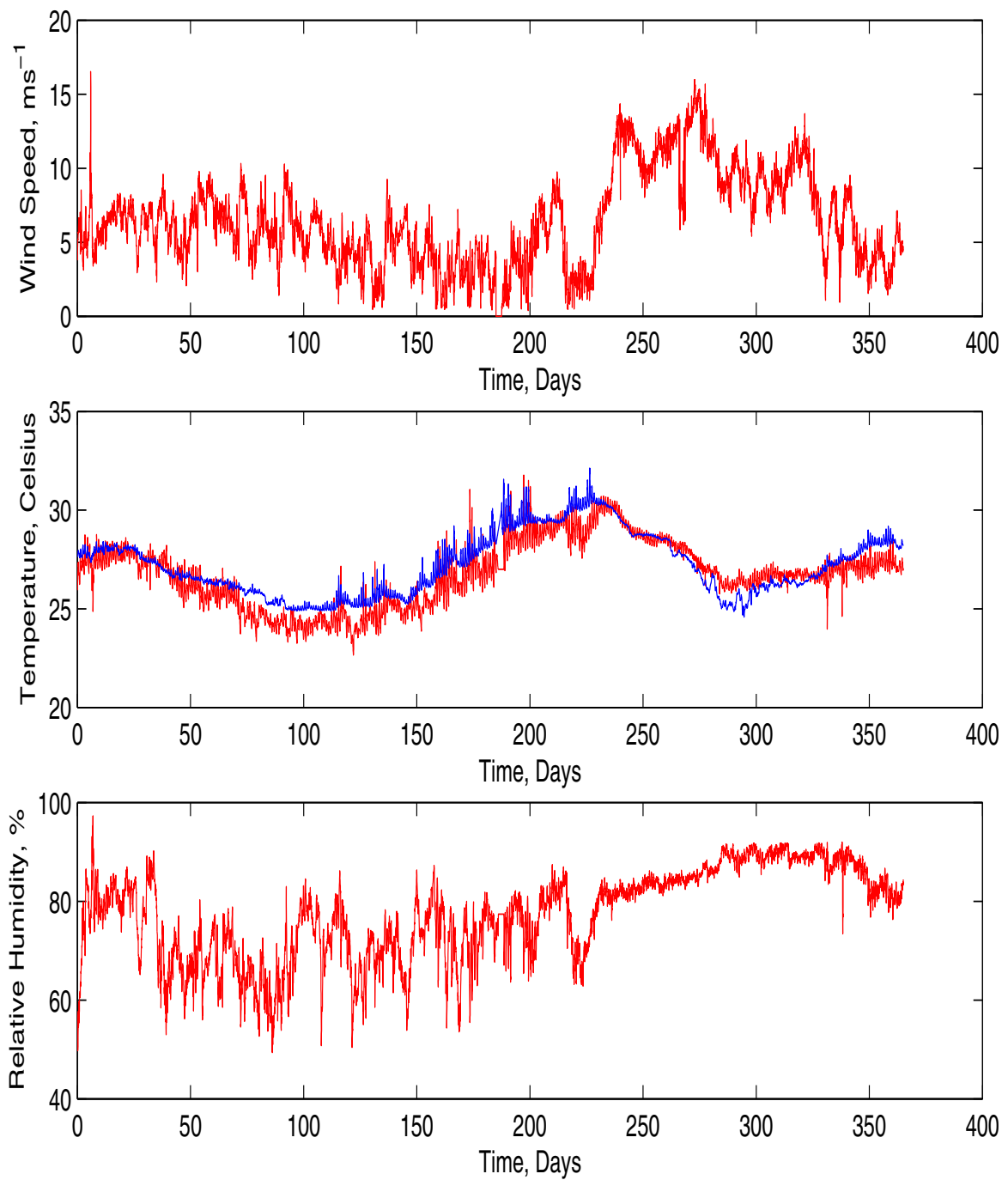
Figure 4.1: *Time series of observables from the Arabian Sea buoy. From the top: wind speed, air (red) and sea surface (blue) temperatures, and relative humidity. All are one hour averages, starting 17/10/94 and ending 17/10/95.*

4.3 Modelling the Upper Ocean

This chapter presents modelling results at the three mooring sites. The ability of the model to replicate the sea temperature records, given the observed forcing, can be assessed in various ways. Comparisons are made between the observed and modelled sea temperatures at various or all depths in the water column. Particular interest is paid to the depth of the shallowest measurement (0.45, 0.17, and 1.0 metres at COARE, Arabian Sea, and Subduction respectively) and the ability to model the near surface variability. In this thesis the magnitude of diurnal warming is defined as the maximum SST (at the shallowest observed depth, z_1^{obs}) minus the minimum SST over a 24 hour window starting at 00:00 GMT

$$\Delta\theta_{z_1^{\mathrm{obs}}} = \max_{0-24} \theta_{z_1^{\mathrm{obs}}} - \min_{0-24} \theta_{z_1^{\mathrm{obs}}}. \tag{4.1}$$

A diurnal warming signal of zero is given if the SST at the start remains the maximum over the day; this eliminates the misinterpretation of a cooling trend.

Quantifying the near surface stratification can be another measure of the ability of the model to reproduce the fine near surface detail. This is calculated by recording the difference between the temperatures at the shallowest observation point and at the 10 m depth as follows

$$\text{stratification} = \theta_{z_1^{\mathrm{obs}}} - \theta_{10\mathrm{m}}. \tag{4.2}$$

Choosing an appropriate definition for the mixed layer depth (MLD) to allow comparisons between in-situ observations and turbulent model output is not straight forward [64]. A MLD can be diagnosed from the temperature measurements and compared with model output. Here we define the MLD as the grid level depth at which the modelled/observed sea temperature is $0.1\,^{\circ}\mathrm{C}$ below the maximum modelled/observed sea temperature in the top 20 m. This is the same criterion used by Weller et al [156], but many others could have been adopted (see Table 1 in [64] for various criteria used by others and also Table 2 in [2] for MLD definitions used in the warm pool region).

Another useful measure to validate the model is to compare the temporal evolution of total column integrated heat content calculated from observed and modelled temperatures. This is obtained by integrating the Heat Equation (2.2) from the surface

40

to the maximum modelled depth, $z = 150\,\text{m}$, and then integrating again over different times, T, to give the evolution

$$c_p \rho_0 \int_0^T \int_{150}^0 \frac{\partial \theta}{\partial t} dz dt = \int_0^T I + Q dt. \tag{4.3}$$

The two sides of this equation were evaluated from model results at the three mooring sites over the whole time series giving values of $3.2 \times 10^8\,\text{Jm}^{-2}$ at COARE, $2.1 \times 10^9\,\text{Jm}^{-2}$ at Arabian Sea, and $4.8 \times 10^8\,\text{Jm}^{-2}$ at the Subduction site. The balance of both sides of Equation (4.3) demonstrates that the model conserves heat entering and leaving through the surface boundary. Another comparison is made by comparing the left hand side of Equation (4.3) evaluated using observed temperatures and modelled temperatures (see Section 4.5). This is not expected to be identical as the complete Heat Equation (1.1) has been severely simplified to give Equation (2.2). The modelled temperatures do not represent all processes that are going on in the real world and this measure can be used to assess the validity of the model assumptions.

4.4 Sensitivity of Model to Parameterisations

The air-sea flux parameterisations discussed in Sections 3.5.7 and 3.5.8 and the ocean radiant heating parameterisations discussed in Section 3.3 are compared at the mooring sites. The sensitivity of the modelled SST and diurnal cycle to changes in the parameterisations are examined.

4.4.1 Kondo vs Fairall

Air-sea fluxes were calculated at the three mooring sites using the two different algorithms introduced in Sections 3.5.7 and 3.5.8 and referred to as Kondo and Fairall respectively. A comparison of the results from applying the two algorithms in terms of the resulting SSTs is given in Figure 4.2, and statistics presented in Table 4.2.

In Figure 4.2 (a) a divergence in the two modelled SSTs is only noticeable just after day 80. In contrast in plot (c) the offset of the two modelled SSTs is noticeable almost immediately. At the Arabian Sea site, plot (b), major divergences occur around day 10
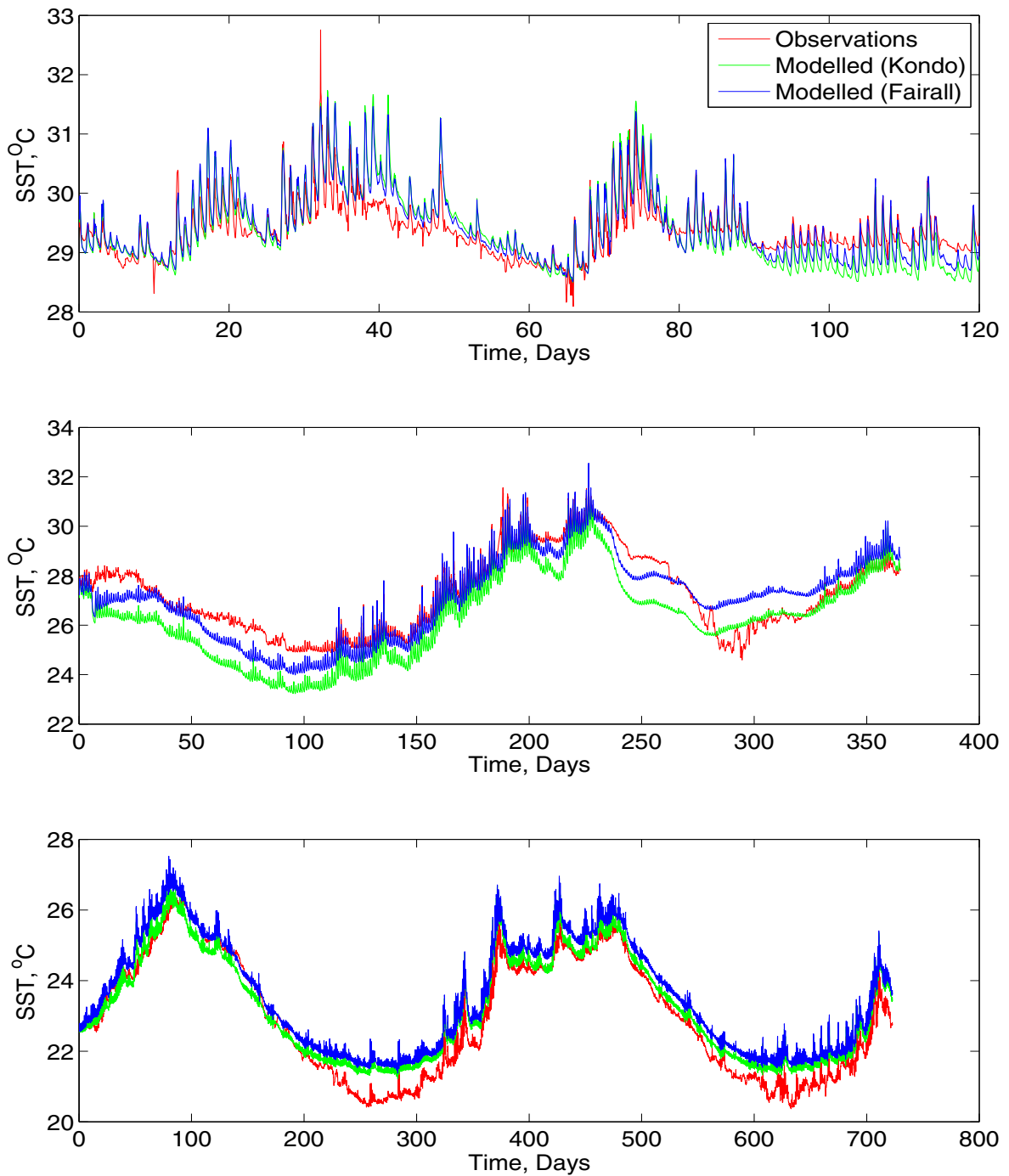
Figure 4.2: *A one year SST comparison between observed (red) and modelled, using Fairall (blue) and Kondo (green) air-sea flux algorithms. From top a) COARE, b) Arabian Sea, and c) Subduction site.*

		RMS Errors		
Site	Flux Scheme	SST	Diurnal Warming	Stratification
COARE	Kondo	0.36	0.36	0.25
COARE	Fairall	0.29	0.36	0.22
Arabian Sea	Kondo	1.15	0.28	0.26
Arabian Sea	Fairall	0.71	0.26	0.23
Subduction	Kondo	0.48	0.17	0.14
Subduction	Fairall	0.66	0.18	0.14

Table 4.2: *Statistics from comparisons derived from observations and model simulations at the mooring sites using the Kondo and Fairall air-sea flux schemes. Values in °C.*

and day 230. It is interesting to compare these times in Figure 4.1 where in both cases the wind speeds rise sharply. For the first case, around day 10, there is a sharp spike in the wind speeds, mentioned in [156] as a squall. The second case, around day 230, is the onset of the Southwest Monsoon with typically strong winds. At all three sites the Kondo algorithm produces lower SSTs than the Fairall algorithm. This is associated with the larger latent and sensible heat release calculated by Kondo when compared to Fairall, as seen in Table 4.3. The results in Table 4.2 show an improvement in the resulting SST when using the Fairall algorithm, except at the Subduction experiment site. The diurnal warming estimates remain relatively unchanged, and the improvements in the stratification are slight. Similar improvements in SST were also found by Hallsworth [50] when comparing modelled SSTs forced with fluxes from Kondo and Fairall at the COARE and Arabian Sea sites. It should be stated that the modelled SSTs feedback to the calculated latent and sensible heat fluxes. This feedback effect is eliminated by using the observed SSTs in the air-sea flux algorithms; these results are presented in brackets in Tables 4.3 and 4.4.

No air-sea flux measurements were taken at the mooring sites and so a comparison between the modelled and observed fluxes is not possible. However, we can analyse some of the differences in the air-sea fluxes calculated from the two algorithms and

these are presented in Tables 4.3 and 4.4. The values in these tables are calculated from hourly output. The mean air-sea flux values over the whole observational time-series at each mooring site, as shown in Table 4.3, are different for the two algorithms. The Fairall values are generally smaller in each case. The largest difference occurs in the sensible heat flux, which on average over the three mooring sites is 39% smaller for the Fairall estimate compared to Kondo. The root mean square differences between the two schemes as shown in Table 4.4 are also relatively large. Again this is particularly true for the sensible heat flux where the differences between the Fairall and Kondo scheme can be over 50% of the mean value.

		Mean Values		
Site	Flux Scheme	Q_E (Wm^{-2})	Q_H (Wm^{-2})	$|\boldsymbol{\tau}|$ (Nm^{-2})
COARE	Kondo	-101.99 (-102.42)	-10.44 (-10.49)	0.05 (0.05)
COARE	Fairall	-104.38 (-102.94)	-7.87 (-7.57)	0.04 (0.04)
Arabian Sea	Kondo	-124.31 (-142.21)	7.32 (-3.09)	0.1 (0.1)
Arabian Sea	Fairall	-107.32 (-111.06)	0.48 (-0.44)	0.1 (0.1)
Subduction	Kondo	-119.65 (-116.39)	-12.6 (-9.44)	0.08 (0.08)
Subduction	Fairall	-117.3 (-102.38)	-11.57 (-6.09)	0.07 (0.07)

Table 4.3: *Mean air-sea fluxes (latent heat, Q_E; sensible heat, Q_H; and wind stress, $|\boldsymbol{\tau}|$) calculated using the Kondo and Fairall algorithms. Values in brackets use the observed SST as opposed to the modelled SST to calculate the air-sea fluxes.*

The results shown in this thesis use the TOGA COARE algorithm developed by Fairall et al which is widely appreciated as being significantly more accurate [97]. The evidence presented here is limited as no flux observations are available for comparison. However, results from comparing modelled SSTs, from the two flux methods, to observations seem to favour the Fairall algorithm. Results presented in this section also show that the instantaneous differences between the calculated fluxes of the two methods are significant.

	RMS Differences		
Site	Q_E (Wm^{-2})	Q_H (Wm^{-2})	$|\boldsymbol{\tau}|$ (Nm^{-2})
COARE	35.39 (35.47)	4.00 (4.07)	0.01 (0.01)
Arabian Sea	31.25 (40.34)	9.39 (3.09)	0.01 (0.01)
Subduction	14.45 (20.23)	2.56 (3.77)	0.01 (0.01)

Table 4.4: *Root mean square differences between the air-sea fluxes of latent heat, sensible heat, and wind stress as calculated from the Kondo and Fairall parameterisations. Values in brackets use the observed SST as opposed to the modelled SST to calculate the air-sea fluxes.*

4.4.2 Radiant Heating Parameterisations

An introduction to ocean radiant heat parameterisations is given in Section 3.3. The public domain version of GOTM uses the 2-band parameterisation of Paulson and Simpson [100]. This is wholly inadequate for the purposes of modelling near surface temperature variability and so Paulson and Simpson's extension to a 9-stream parameterisation [101] was implemented into GOTM by S. Hallsworth [50]. This division of solar radiation incident at the surface into further discrete wavelength bands provides much needed additional resolution of the rapid attenuation of larger wavelengths at the near surface. Improvements in the near surface temperature profiles were found when using the 9-band over the 2-band parameterisation. Results from using the 2-band (with Jerlov water type 1, the most representative of the open ocean [129]) and 9-band schemes were compared by performing model simulations forced with SWR and LWR observations at the three mooring sites. RMS error in SST over all model-observation differences at every observation depth in the top 10 metres (0.45, 0.55, 1.1, 1.58, 2.0, 2.5, 6.94, 7.44, and 9.77 metres at COARE; 0.17, 0.43, 0.92, 1.37, 1.41, 1.8, 1.91, 2.4, 3.5, 4.5, 5.0, and 10.0 metres at the Arabian Sea; and 1.0 and 10.0 at the Subduction Site) were then calculated. The RMS error improvements in favour of the 9-band radiation scheme at the Arabian Sea is 2.37 °C to 2.49 °C and at the Subduction site 0.93 °C to 0.95 °C. However, the COARE site showed the 2-band scheme reduced the

errors from 0.76 °C to 0.62 °C. The results at the mooring sites presented in this thesis use the 9-band parameterisation.

4.5 Model Results and Discussion

In this section a more detailed analysis of the model results at the three mooring sites is presented. In these experiments the model is initialised with observed sea temperatures at the start of the time series and forced with air-sea fluxes calculated from the surface meteorology (Table 4.1) using the Fairall air-sea flux algorithm, together with down-welling SWR and LWR observations every 15 minutes.

4.5.1 COARE

Given in Figure 4.3 are plots of SST, daily maximum MLD, and the total column heat content. Comparisons are made from modelled output and observations. Over the 120 days the RMS of $(\theta_{0.45\mathrm{m}} - \theta_{0.45\mathrm{m}^{obs}})$ is 0.29 °C (recorded in Table 4.5). There is a slight model warming bias of 0.07 °C over the whole time series. A warming bias is particularly noticeable during days 30–60 and this coincides with a shallower MLD in the model compared to observations. However, the cooling bias in modelled SST from day 80 to the end also seems to be coincident with a shallower MLD. The diurnal variability of the SST from observations and model can be seen in Figure 4.3 (a). These diurnal warming cycles are expected to be large in this tropical region where the mean daily peak SWR over the time series is $828\,\mathrm{Wm^{-2}}$. The mean diurnal warming from the 0.45 m observed temperatures $(\Delta\theta_{0.45\mathrm{m}}^{obs})$ is 0.57 °C and the daily mean modelled value is larger at 0.71 °C. The RMS of $(\Delta\theta_{0.45\mathrm{m}} - \Delta\theta_{0.45\mathrm{m}}^{obs})$ is 0.36 °C.

The MLD is consistently under predicted with a RMS error of 14.85 m. In Figure 4.3 (b) it is seen that the low frequency pattern and changes to MLD over the time period are well represented by the model. There are days (5, 25, 45, and 90) when the full extent of the mixed layer deepening is not matched by the model. This shallower MLD starting ($\sim$ day 5) is likely to be the cause of the warming bias seen in the modelled SST over the first 75 days. A shallower mixed layer warms/cools quicker when the ocean

Figure 4.3: *Model-observation comparisons at COARE. From the top: (a) model simulation of $\theta_{0.45m}$ (blue) and observations (red), (b) the daily maximum MLD derived from observed (red) and modelled (blue) temperatures, and (c) the temporal evolution of total column integrated heat content derived from observed (red) and modelled (blue) temperatures (the signal is filtered through a 24 hour mean).*

gains/loses heat and thus causes temperatures to rise/fall faster within the mixed layer.

The evolution of the total column integrated heat content is seen in Figure 4.3 (c). In these heat content plots what is important is not the distance between the observed and control lines, but the difference in the rate of change of the heat content, or the gradient of the lines. Such a difference in gradient is visible just after day 60 with a drop in the observed heat content and its subsequent increase again around day 85. These differences highlight signals in the observed data not captured by the model. Comparing these days (65–90) on the other plots in Figure 4.3 it is noted that at these times the MLD and the variability of SST is modelled very well, illustrating that the departure of modelled heat content from the observed is likely caused by the temperatures below the mixed layer.

4.5.2 Arabian Sea Site

Figure 4.4 shows the oceanic response to the strong, large-scale atmospheric forcing associated with the summer and winter monsoons, as mentioned in Section 4.2, producing this unique double cooling trend. The occasions of the largest error in SST occur during the monsoon periods. During the winter or NE Monsoon, days 14–121, the modelled SST has a cold bias, whereas for the summer or SW Monsoon, days 226–333, the modelled SST is initially much cooler but around day 275 becomes significantly warmer, as it is unable to match the amount of cooling that occurred in the observed temperatures.

It is noted that the period of very low wind speeds ($\sim$ days 130–230, as seen in Figure 4.1) in the inter-monsoon warming phase produces large diurnal variability in the SST. Over the year the mean diurnal warming ($\Delta\theta_{0.17\text{m}}^{obs}$) was $0.48\,^\circ$C with a modelled value of $0.62\,^\circ$C. The RMS $\left(\Delta\theta_{0.17\text{m}} - \Delta\theta_{0.17\text{m}}^{obs}\right)$ was $0.26\,^\circ$C, as shown in Table 4.5.

The period of cooler modelled than observed SSTs coincided with a shallower MLD than that derived from observed temperature profiles. Much of the warm SST bias also coincides with a deeper MLD than that derived from observations, as seen in Figure 4.4 (b). Times of large changes to the observed MLD are coincident with large changes
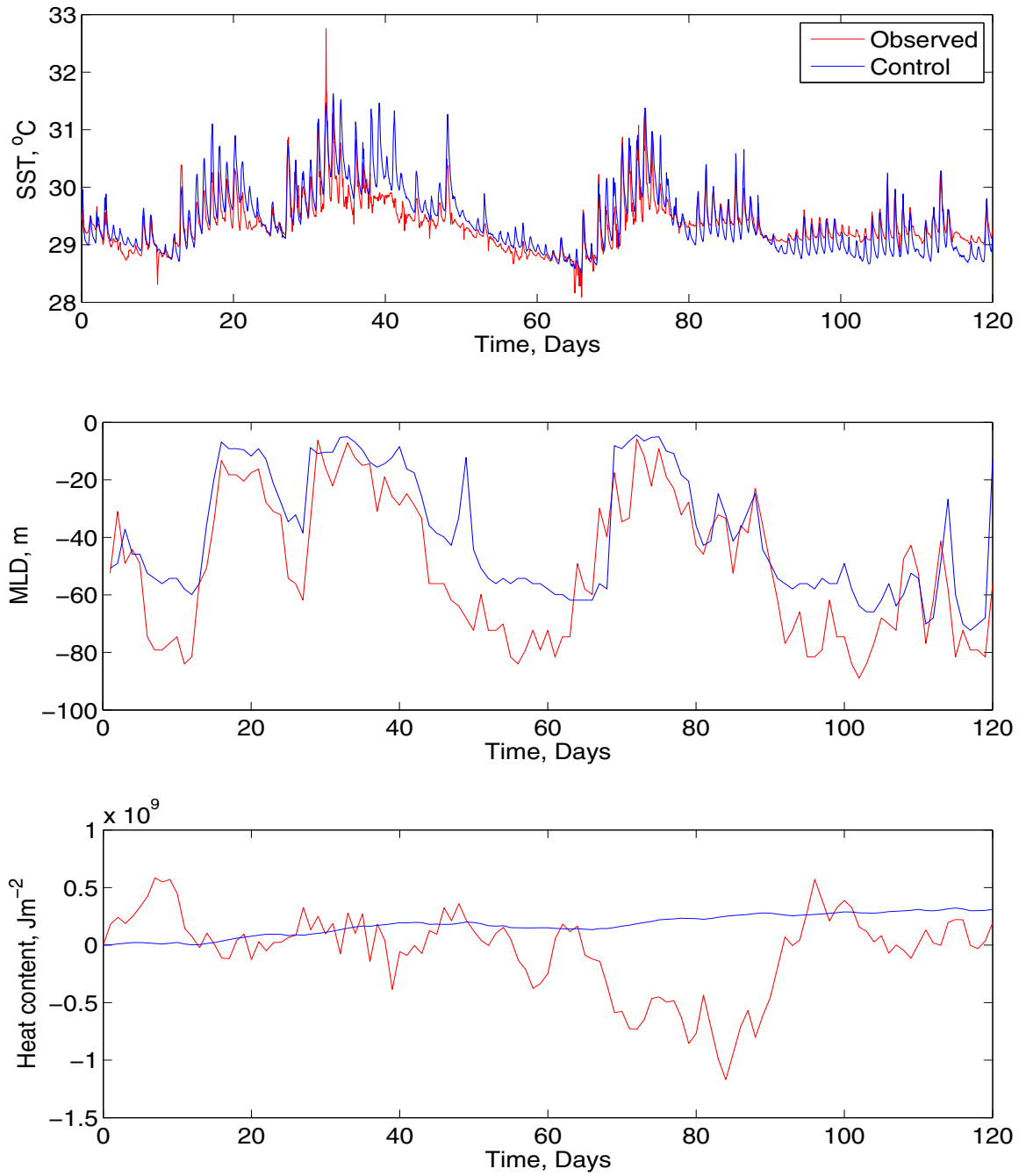
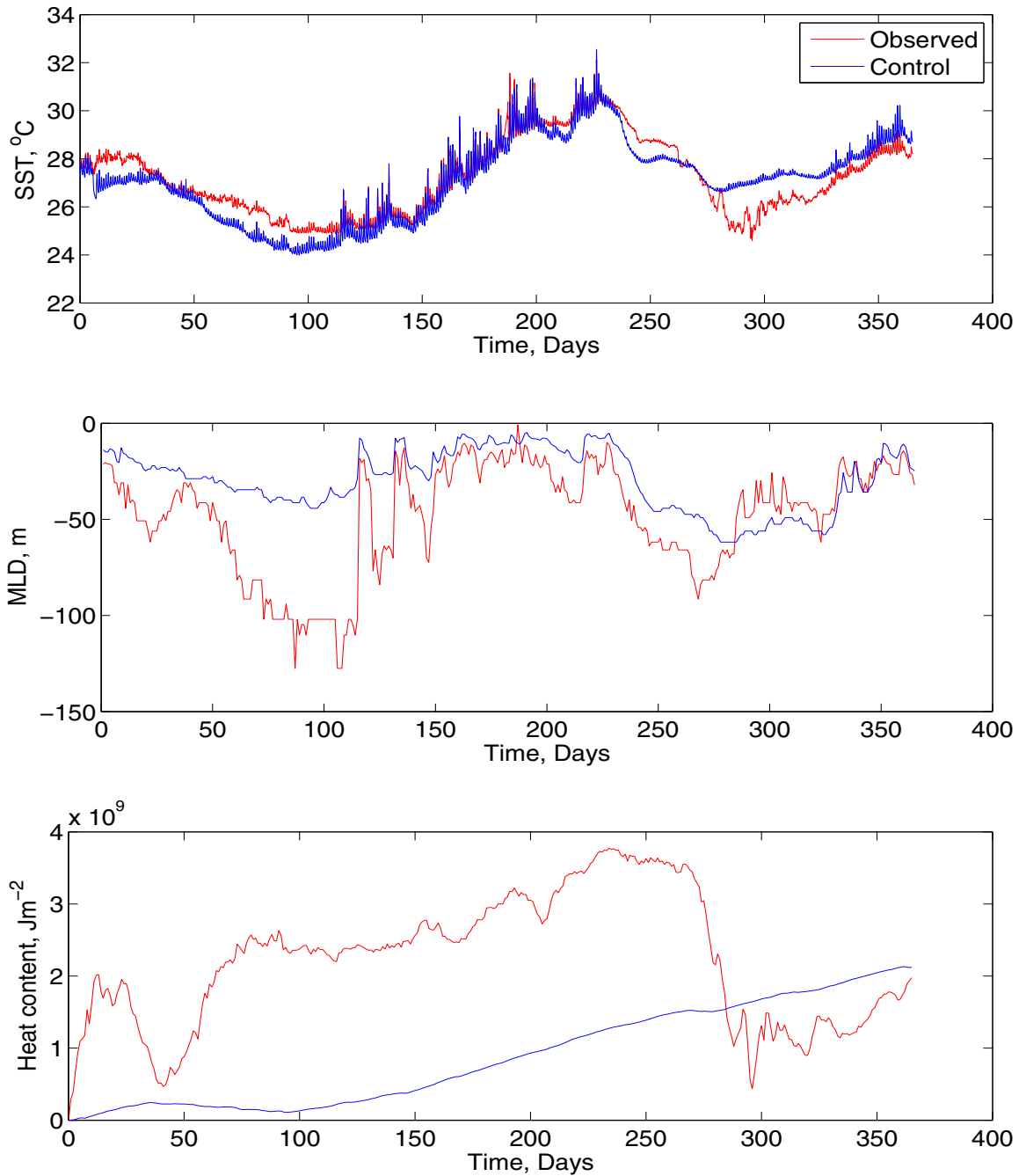Figure 4.4: *Model-observation comparisons at Arabian Sea. From the top: (a) model simulation of $\theta(0.17m)$ (blue) and observations (red), (b) the daily maximum MLD derived from observed (red) and modelled (blue) temperatures, and (c) the temporal evolution of total column integrated heat content derived from observed (red) and modelled (blue) temperatures (the signal is filtered through a 24 hour mean).*

to the observed heat content. It is clear that on these occasions the evolution of the modelled and observed heat content are rather different. In Equation (4.3) it is shown that the modelled value is determined by the total heat flux $I + Q$, this being the only supply of heat to the system. Here $I + Q$ is calculated from observed down-welling SWR and LWR values with parameterised values of latent and sensible heat flux and up-welling LWR (see Sections 3.4 and 3.5). The use of parameterisations could be a source of potential error in the modelled heat content. However, on the occasions when the two lines in Figure 4.4 (c) significantly diverge (e.g. between days 0–10, 25–80, and 270–280) the errors are so large that uncertainties in Q_E, Q_H, and $Q_B^\uparrow$ can be ruled out as the major contributing factor to this divergence of heat content. For example, in the first 10 days the heat content derived from temperature observations increases by approximately $1.5 \times 10^9 \, \mathrm{Jm^{-2}}$ over the modelled heat content, this would represent an increase in surface heat fluxes of over $1700 \, \mathrm{Wm^{-2}}$ for this period, clearly impossible. However, if advection is important, i.e. $\boldsymbol{v} \cdot \nabla \theta$ is large on these occasions, then our modelling assumption breaks down and we might expect these kinds of differences.

A paper by Fischer [39] using the same data, in addition to remotely sensed data of the region demonstrates that the observed temperature trend over the whole period is roughly balanced when the heat budget includes the surface forcing, but also strong episodic modulation from mesoscale variability in the horizontal advection. The paper concludes that this mesoscale modulation took two forms, one for each monsoon period. During the NE Monsoon (days 14–121) the heat budget was influenced by the passage of a series of mesoscale eddies with large variations in thermocline depth, but little surface signature. Then during the SW Monsoon (days 226–333) cool, coastal up-welled water transported to the moored site by mesoscale eddies was deemed a major contributor to the upper ocean heat budget. These features can clearly be seen in Figure 4.5. The deficiencies in the model during the monsoon seasons, as seen in Figures 4.4 and 4.5, can be explained to a great extent by the nature and timing of advection events described in [39], but missing from this model. However during the inter-monsoon periods the Arabian Sea experiences little or no advection, and model behaviour is in good agreement with the observations.
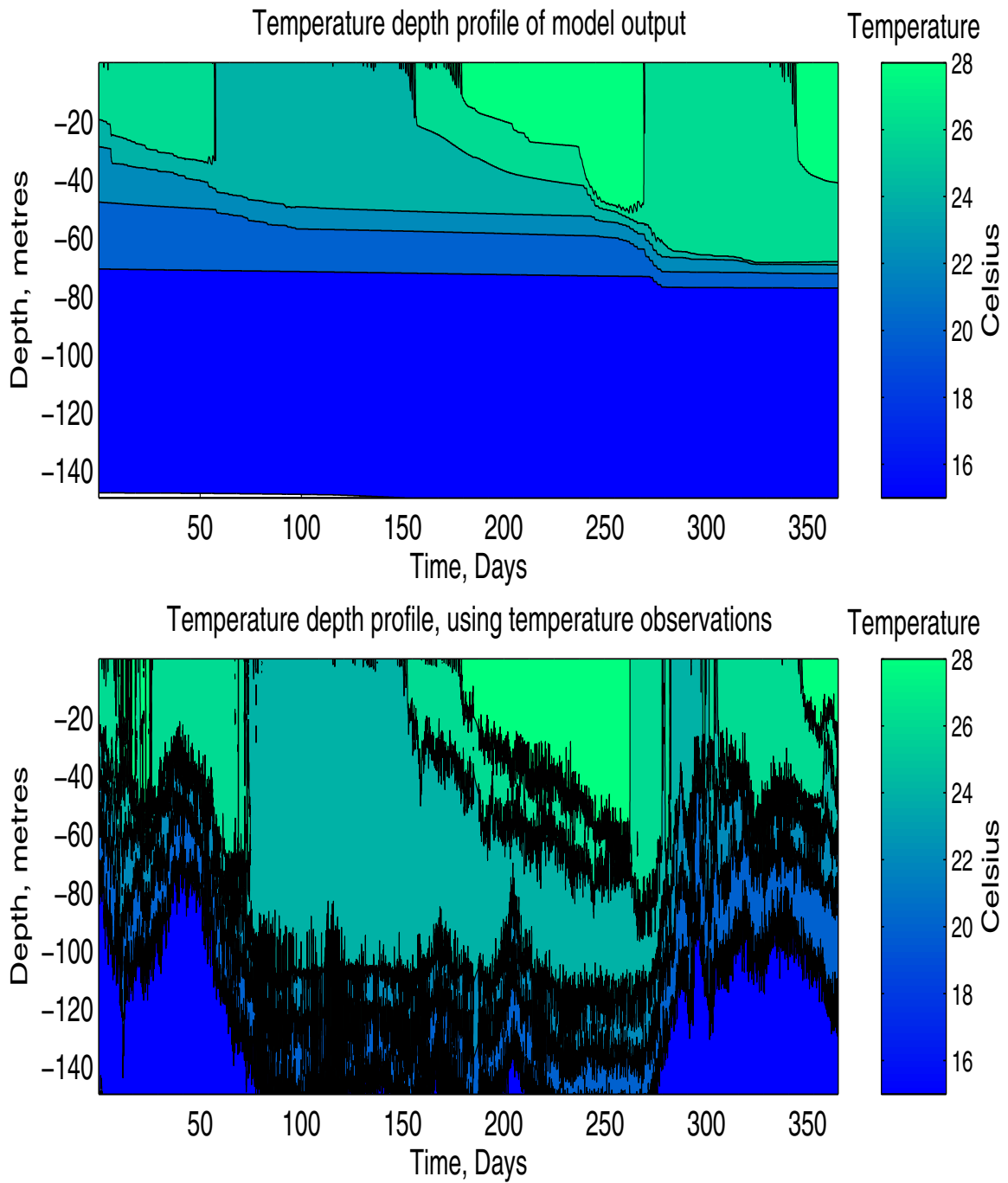
Figure 4.5: *One year temperature depth profile comparing model temperatures (top) with observed temperatures (bottom).*

4.5.3   Subduction Experiment Region

Figure 4.6 (a) shows that the modelled SST warms in relation to the observations at around day 150 coincident with a decrease in observed heat content (see Figure 4.6 (c)). Over the whole time series the modelled 1 metre SST has a warm bias of 0.58 °C. The RMS of $(\theta_{1m} - \theta_{1m}^{obs})$ over the time series is 0.66 °C, see Table 4.5. The mean diurnal warming signals at this depth are 0.26 °C for the observations and 0.36 °C for the model. The annual deepening and shoaling of the mixed layer is again well represented by the model over this long simulation. In the heat content plot in Figure 4.6 (c) the observed and modelled values of the first 100 days are closely matched. However after this time the heat content derived from the temperature observations significantly decreases with respect to the model derived values, and from this point the model contains much more heat than is observed.

Site	SST (°C)	RMS Errors Diurnal Warming (°C)	MLD (m)	Stratification (°C)
COARE	0.29	0.36	14.85	0.22
Arabian Sea	0.71	0.26	23.81	0.23
Subduction	0.66	0.18	26.19	0.14

Table 4.5: *Statistics from comparisons derived from observations and model simulations at the mooring sites.*

4.6   Effects of Different Cloud Forcing

In this section an investigation is made into the impact of cloud effects on the upper ocean. The SWR is the largest component of the ocean heat budget and the amount of radiation received at the sea surface is significantly affected by cloud cover which acts as a barrier preventing the sun's radiation from reaching the sea surface. Cloud cover also influences the down-welling component of the LWR, as clouds emit thermal infrared radiation.
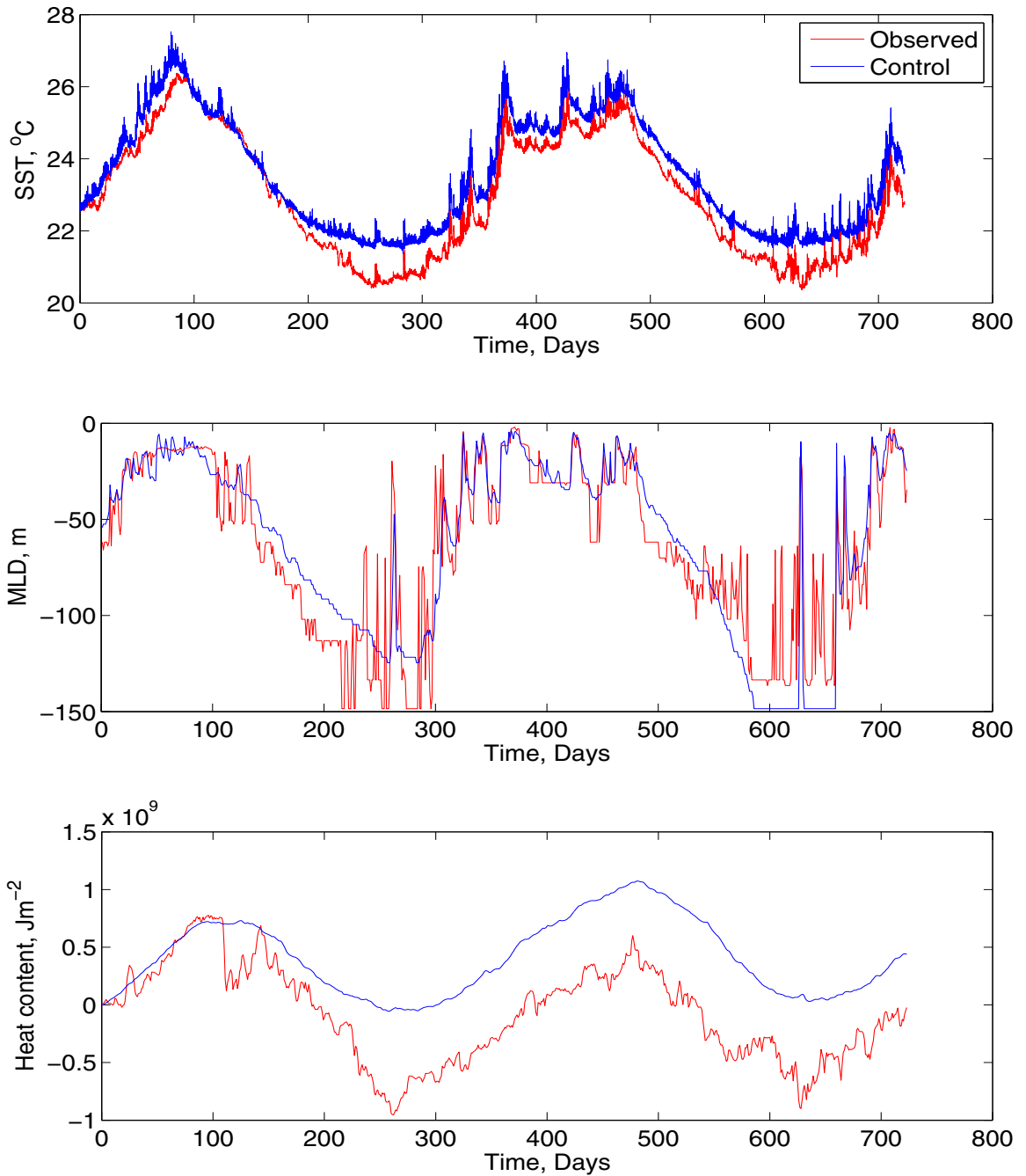
Figure 4.6: *Model-observation comparison at Subduction. From the top: model simulation of θ(1.0m) (blue) and observations (red), the daily maximum MLD derived from observed (red) and modelled (blue) temperatures, and the temporal evolution of total column integrated heat content derived from observed (red) and modelled (blue) temperatures (the signal is filtered through a 24 hour mean).*

At the Arabian Sea site the down-welling components of SWR and LWR were observed and this data was used to force the model and the outcomes compared with output from the parameterized clear sky SWR and LWR. The improvements achieved by the inclusion of the SWR and LWR observations are demonstrated in Figure 4.7.
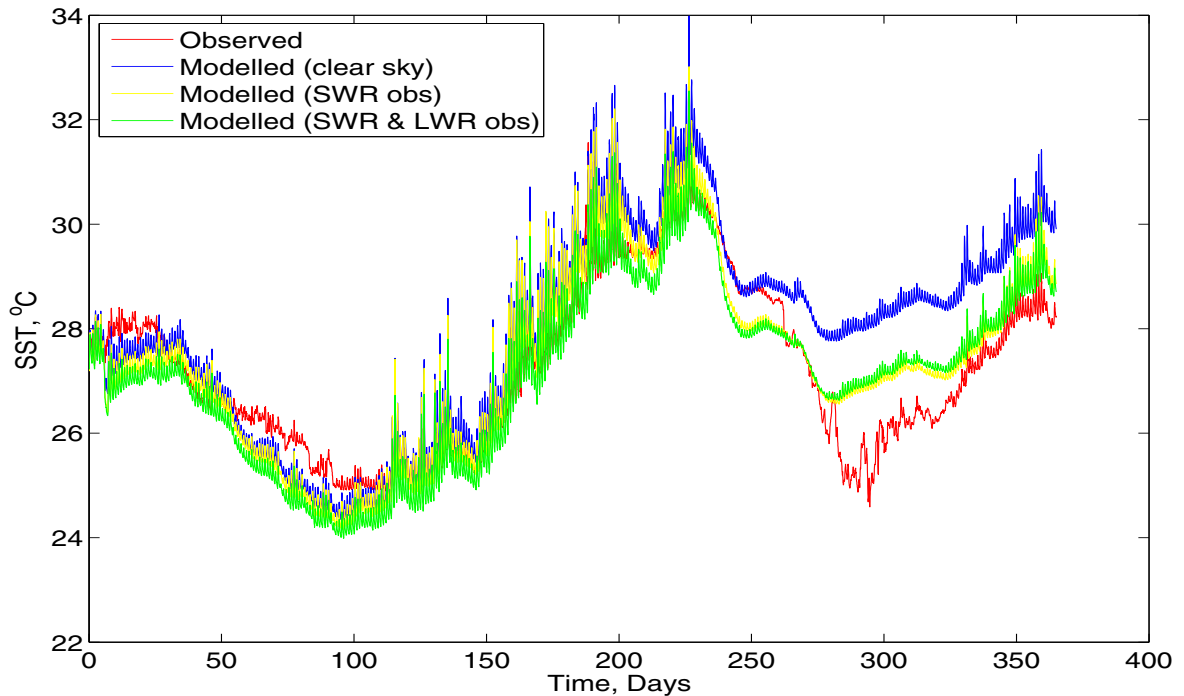
Figure 4.7: *A one year SST comparison between observed (red) and modelled using clear sky conditions (blue), SWR observations (yellow), and SWR and LWR observations (green).*

The inclusion of SWR and LWR observations within the model eliminates the difficulty in quantifying the cloud cover. In Figure 4.7 it is clearly seen that the use of SWR observations in the model simulations leads to large improvements in the estimated SST, particularly during the summer monsoon period (days 220–365) when typically cloudy conditions are known to occur [155]. Table 4.6 shows larger biases and root mean square errors for both the SST and the diurnal amplitudes when clear sky conditions were assumed. The further inclusion of LWR observations actually seems to deteriorate the solution slightly, although this must highlight the true errors from other sources. As discussed in Section 4.5.2 it has been shown that the remaining error

is primarily caused by advection events at these times.

	Mean Error		RMS Error	
	SST	DW	SST	DW
SWR & LWR Observations	0.13	−0.14	0.71	0.26
SWR Observations	−0.12	−0.15	0.65	0.28
Clear Sky Conditions	−0.66	−0.2	1.17	0.31

Table 4.6: *A table showing the modelled SST and diurnal warming (DW) accuracy, in* °C, *at the Arabian Sea forced with SWR and LWR down-welling observations, SWR down-welling observations with clear sky for LWR, and clear sky conditions for SWR and LWR.*

The sensitivity of the model to the cloud parameter can further be seen at the COARE site where SWR values are high, and large diurnal warming events are evident, as shown in Figure 4.8. The day to day variability in the SWR observations (as can be seen in Figure 5.3), primarily due to changes in cloud cover, are large and on occasions over $150 \, \text{Wm}^{-2}$, which can be half the daily mean SWR value on some days. If the model is forced with a constant cloud cover value, then day to day variability in SWR is not present and this can significantly effect the modelled diurnal cycle (see Table 4.7).

As is mentioned in Section 3.2 the Reed formula (Equation (3.5)) and the clear sky parameterisation have been found to have biases at specific sites. The recommendation, as discussed in Section 3.2, is to use radiometric observations to optimise the parameterisation at specific locations. Following the suggestions of [120] and [55] the transmission coefficient and the cloud cover coefficient are adjusted based on the SWR observations taken at the mooring sites. To ensure over 90% of the SWR observations fall between the clear sky and full cloud limits of the Reed parameterisation, the transmission coefficient was kept at 0.7 at the Subduction site, reduced to 0.63 at the COARE site, and increased to 0.74 at the Arabian Sea. The cloud cover coefficient remained 0.62 at the Subduction and Arabian Sea sites, but was increased to 0.72 at the COARE site.

Clear sky and full cloud conditions are applied at the COARE site and the resulting

SST values are shown in Figure 4.8. It is important not only to notice the drift in SST with zero cloud cover, but also the exaggerated diurnal cycle compared with the observed trends and peaks. The converse is also noted: simulating full cloud conditions leads to an underestimation of SST and its diurnal amplitudes. The mean diurnal warming from observations, clear sky, and full cloud are as follows: $0.48\,°C$, $0.85\,°C$, and $0.33\,°C$. This shows how uncertainty in cloud cover could substantially effect the modelled diurnal cycle. Error statistics are presented in Table 4.7.
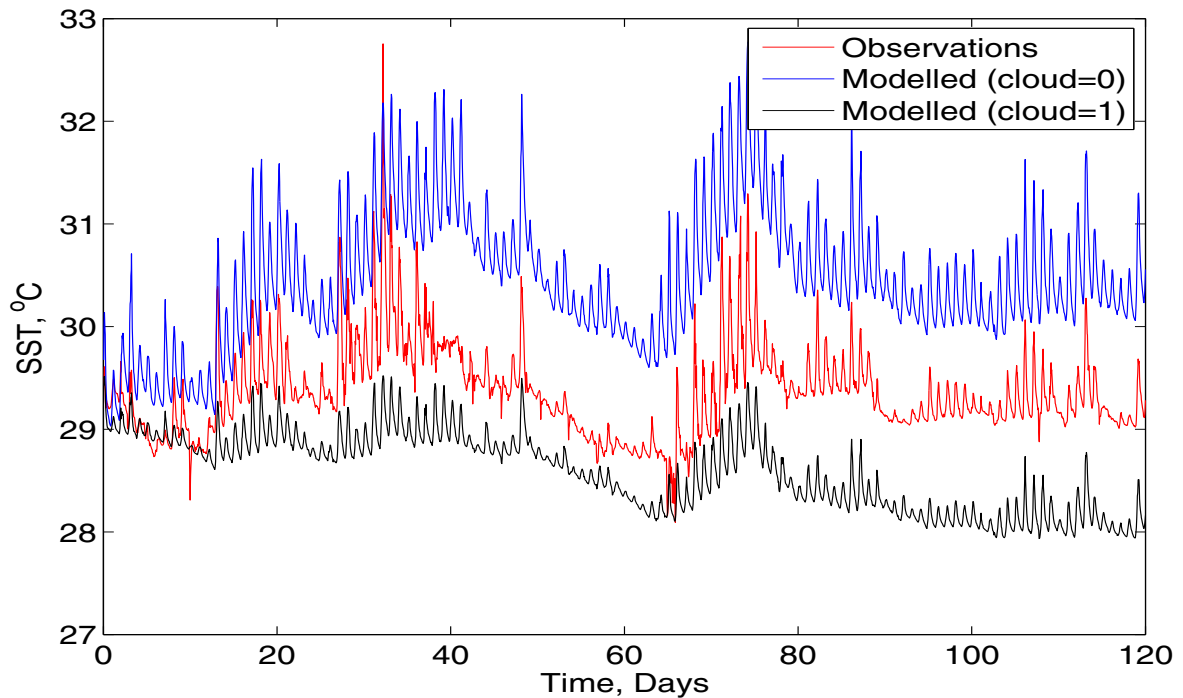
Figure 4.8: *A comparison between model runs with the cloud parameter set at the extremes of no cloud (blue) and full cloud (black) against the observed (red) for the TOGA COARE region.*

To correct the warming drift in SST when the parameterised clear sky SWR is used the ratio of the mean SWR observations to the mean clear sky SWR over the whole period was calculated. A model simulation was then performed in which the parameterised clear sky SWR values were multiplied by this ratio, calculated to be 0.70 at COARE. Hence the mean SWR over the 120 days would be the same for model and observation ($196.32\,\mathrm{Wm}^{-2}$), this ratio could be thought of as an average cloud cover

correction (with an effective mean cloud cover value of 0.30, following [41]) to the clear sky SWR over the whole period. Results from this experiment, shown in Table 4.7, reveal that the SST no longer has a drift and the SST bias is of the same magnitude as when using the SWR observations. The RMS errors have also significantly reduced from the clear sky and full cloud SWR cases becoming similar to the SWR observation case, as would be expected. This mean correction to the clear sky SWR was also calculated at the Arabian Sea and Subduction sites with values of 0.82 and 0.79 giving effective mean cloud cover values at these locations of 0.18 and 0.21 respectively.

	Mean Error		RMS Error	
	SST	DW	SST	DW
SWR & LWR Observations	−0.07	−0.14	0.29	0.36
SWR Observations	−0.04	−0.11	0.31	0.35
Clear Sky	−1.32	−0.31	1.39	0.47
Full Cloud SWR	0.29	0.13	0.39	0.37
Modelled SWR Without 120 Day Bias	0.04	0.01	0.25	0.34

Table 4.7: *A table showing the extent to which SST and its diurnal cycle match observations when using various SWR options. Results are at the COARE sites and values are in* °C.

4.7 Effects of Lowering Forcing Resolution

It is unusual to have complete very accurate high frequency forcing data over ocean areas and as such the data from the three mooring sites used in this chapter are very rare. In this next section the surface meteorological observations as well as the downwelling SWR and LWR from the buoys are averaged over 6 hourly periods. The model was then re-run using the 6 hourly mean meteorological values in the air-sea flux calculations. The 6 hourly mean observed SWR values are used a priori to derive 6 hourly mean cloud values by calculating the clear sky values (using the corrected atmospheric

transmission at the individual sites) and inverting the Reed formula (Equation (3.5))

$$n = \left(1 - \frac{\overline{I_{obs}}}{\overline{I_\downarrow}} + 0.0019\beta\right)/C_n. \tag{4.4}$$

Where over-bar denotes a 6 hourly mean value. This technique allows the SWR to be calculated at a much finer time resolution (at each model time step) with a 6 hourly fixed cloud correction performed using the Reed formula. The diurnal cycle of SST is a fundamental response to the solar forcing over the day, this technique is therefore an essential feature.

Unfortunately a similar technique is not possible for the wind forcing. It is acknowledged that there will be occasions when a complete representation of the phase and shape of the diurnal cycle will not be possible because of the sensitivity of the system to fine scale wind variability.

The results are presented in Table 4.8 and should be compared with results from the high frequency forcing simulations in Table 4.5. In all cases the root mean square errors increase when using the 6 hourly forcing, with the exceptions of SST at the COARE site and the MLD at the Subduction experiment site. The deterioration of accuracy however is slight, for example the RMS error of the diurnal warming measure increases by 8.9 % on average over the three sites. This gives hope that the diurnal cycle can be effectively modelled with 6 hourly forcing data. The standard output from operational weather forecasting centres is 6 hourly, therefore modelling the diurnal cycle of SSTs over the global ocean could be a possibility. This proposition is addressed in Chapter 6.

	RMS Errors			
Site	SST (°C)	Diurnal Warming (°C)	MLD (m)	Stratification (°C)
COARE	0.25	0.38	17.73	0.24
Arabian Sea	0.83	0.3	24.51	0.29
Subduction	0.94	0.19	25.97	0.17

Table 4.8: *Statistics from comparisons derived from observations and model simulations forced with 6 hourly data at the mooring sites.*

4.8 Summary

Several improvements to the public domain version of the GOTM have been presented in this chapter. It has been demonstrated that the replacement of the Kondo air-sea flux algorithm with the state-of-the-art TOGA COARE algorithm improves the turbulent forcing at the boundary. The 9-band ocean radiant heating parameterisation has also replaced the previous 2-band parameterisation. These adaptations to GOTM have improved the models capability in capturing diurnal variability. The model was then used in a detailed study of the upper ocean and its diurnal variability at three ocean mooring sites. The results show that the model performs well, although it is highlighted how advection can cause model drift, this was particularly the case on occasions at the Arabian Sea site. In this chapter sensitivity of the models performance to changes in the forcing were also tested and explored. Work is presented on the effects on the modelled SST of uncertainty in cloud values. Both the mean SST and the diurnal warming were shown to be highly sensitive to the SWR and in particular to the variation in the SWR due to cloud cover. In another experiment the forcing data at the mooring sites was reduced to 6 hourly mean values and the model forced with the reduced time resolution data. A technique to calculate the SWR at a finer scale is presented. Under these conditions the deterioration in modelling ability is shown to be slight, which suggests diurnal modelling of SSTs need not be limited to a few upper ocean mooring sites.

Chapter 5

The Assimilation of SST Data

5.1   Introduction

Data assimilation is the process of merging together in an optimal sense measured observations with a dynamical system model to gain maximum likelihood estimates of the required state. Data assimilation has its theoretical foundations in optimal control theory, a branch of mathematics first developed by Pontryagin [103]. It is extensively used in meteorology to find the initial conditions of the state variables for operational weather forecasting [60], but its appeal has spread across the Earth Sciences [139]. What follows in the next section is a short description of a general formulation of data assimilation for a nonlinear dynamical system.

5.2   General Formulation

A system is modelled by the discrete nonlinear equations

$$x_{k+1} = f_k(x_k, u_k), \qquad k = 0, \ldots, N - 1, \tag{5.1}$$

where $x_k \in \mathbb{R}^n$ denotes the model states and $u_k \in \mathbb{R}^{m_k}$ denotes the m_k inputs to the system at time t_k, and $f_k : \mathbb{R}^n \times \mathbb{R}^{m_k} \to \mathbb{R}^n$ is a nonlinear function describing the evolution of the states from time t_k to time t_{k+1}. Observations of this system are taken

and these may be expressed as

$$y_k = h_k(x_k) + \delta_k, \qquad k = 0, \ldots, N-1, \tag{5.2}$$

where $y_k \in \mathbb{R}^{p_k}$ denotes the vector of p_k observations at the time t_k and $h_k : \mathbb{R}^n \to \mathbb{R}^{p_k}$ is called the observation operator and is a nonlinear function that gives a transformation from model space to observation space, which may include grid interpolation. Here the observations are assumed to be unbiased and uncorrelated and $\delta_k \in \mathbb{R}^{p_k}$ represents Gaussian random observational errors with covariance matrices $R_k \in \mathbb{R}^{p_k \times p_k}$. A prior estimate of the initial state x_0, usually obtained from a previous model run, is denoted x_0^b where superscript b stands for background. Again we assume random Gaussian error $(x_0 - x_0^b)$ with covariance matrix $B_0 \in \mathbb{R}^{n \times n}$. Under the formalism of variational calculus the data assimilation problem can be expressed as follows.

Minimise, with respect to x_0, the cost function

$$J = \frac{1}{2} \left\| x_0 - x_0^b \right\|_{B_0}^2 + \frac{1}{2} \sum_{k=0}^{N-1} \left\| h_k(x_k) - y_k \right\|_{R_k}^2, \tag{5.3}$$

subject to x_k, $k = 1, \ldots, N-1$, satisfying the system equations (5.1) with initial states x_0.

(Notation: $\|\cdot\|_A^2 = \langle \cdot, \cdot \rangle_A$ is a 2-norm squared weighted by a covariance matrix A, with the weighted inner product defined as $\langle a, b \rangle_A = a^T A^{-1} b$)

This represents the maximum likelihood and as such the data assimilation equations may also be derived from a statistical viewpoint using Bayesian theory as in Rodgers [114]. Here the initial states are the required control variables in the optimisation. However, it is also possible to set-up the problem to control boundary conditions; for example see Le Dimet and Ouberdous [30]; model parameters, as discussed by Navon [92]; or a combination of the above as demonstrated by Lu and Hsieh [77]. Note that in the above we assume a perfect model and the system equations are treated as strong constraints. For a weak constraint setup see Sasaki [118]; or for the treatment of systematic errors see Dee and DaSilva [27], for bias correction in a 4D-Var system see Griffith and Nichols [48], and for bias correction applied to an operational ocean model see Bell et al [8].

The above problem can be solved directly giving a sequential data assimilation scheme, or indirectly to give a four-dimensional variational (4D-Var) assimilation scheme. Using the direct approach the solution can be expressed as (see Kalnay [60] for a derivation)

$$x_{k+1}^b = f_k(x_k^a, u_k), \tag{5.4}$$

$$x_{k+1}^a = x_{k+1}^b + K_k\left(h_k\left(x_{k+1}^b\right) - y_{k+1}\right), \tag{5.5}$$

where

$$K_k = B_k H_k^T \left(H_k B_k H_k^T + R_k\right)^{-1} \tag{5.6}$$

is called the gain matrix and $H_k = \frac{\partial h_k}{\partial x}\big|_{x_k^b}$ with $k = 0, \ldots, N-1$. Equation (5.4) represents a prediction for the background states produced from the model equations, and Equation (5.5) represents analysed states based on a correction to the background from model-observation differences. The observation operator, H_k, and the observation covariance matrix, R_k, are updated when required. The different, variously named, data assimilation schemes arise around how to best model the background covariance matrix, B_k. For example the Optimal Interpolation (OI) scheme has a static homogeneous background covariance matrix, $B_k \equiv B$, whereas the more sophisticated Kalman Filter [59] seeks to evolve the covariance structure in time; this of course leads to computational difficulties for large problems.

For 4D-Var, the problem (5.3), is first reduced to an unconstrained problem using the method of Lagrange [146]. Necessary conditions for the solution to the unconstrained problem then require that a set of adjoint equations together with the system equations (5.1) must be satisfied. The adjoint equations are given by

$$\lambda_N = 0, \tag{5.7}$$

$$\lambda_k = F_k^T(x_k)\lambda_{k+1} - H_k^T R_k^{-1}\left(h_k(x_k) - y_k\right), \qquad k = N-1, \ldots, 0, \tag{5.8}$$

where $\lambda_k \in \mathbb{R}^n$, $j = 0, \ldots, N$, are the adjoint variables and $F_k \in \mathbb{R}^{n \times n}$ and $H_k \in \mathbb{R}^{n \times p_k}$ are the Jacobians of f_k and h_k with respect to x_k. The gradient of the cost function (5.3) with respect to the initial data x_0 is then given by

$$\nabla_{x_0} J \equiv B_0^{-1}\left(x_0 - x_0^b\right) - \lambda_0. \tag{5.9}$$

This is solved iteratively and each step of the gradient iteration process requires one forward integration of the model equations (5.1) and one backward integration of the adjoint equations (5.8).

5.3   Assimilation of SST

In-situ SST data from buoy and ship measurements are few and far between and availability of data is a core issue for ocean data assimilation. However, it has been said by Craig Donlon, head of GHRSST-PP, that we are now in the golden era of SST measurements as we have access to a wealth of satellite data providing global coverage at very high spatial resolution. So far relatively little attention has been paid to the assimilation of SST, as opposed, for example, to altimetry data where assimilation routines are well understood e.g. [22] and [123]. A particular difficulty arises from how to extract information content about the sub-surface from surface sea temperature observations. To date no one has satisfactorily been able to correct the sub-surface ocean state from SST data. SST is a prognostic variable in ocean models and the general procedure has been to directly assimilate SST observations into models. What follows is an overview of the subject to date.

5.3.1   Ocean Circulation Models

Derber and Rosati [29] assimilated conventionally measured in-situ SST observations into a global ocean model with $1°$ horizontal resolution and 15 layers in the vertical. The SST data were assimilated over a 30 day window and simple horizontal correlations were used to smooth the data field. No vertical correlations were used, however vertical profiles were also assimilated where available.

Clancy et al in [20] and [19] combined synoptic ship, bathythermograph, buoy, and satellite data with the prediction of a mixed-layer model, using an optimal interpolation (OI) scheme to produce large scale synoptic thermal analyses.

An unusual example where only SST data are assimilated is that of Ezer and Mellor [34]. Correlation factors between variations in the surface data and variations in the

sub-surface temperature were used to project the surface information into the deep ocean, using data and model error estimates and an optimal interpolation approach to blend model and observed fields.

The UKMO 1° global FOAM has a top grid point temperature representing a mean value over the top 10 metres of ocean. The SST observations used for assimilation come from fixed surface buoys (TAU / TRITON), a coarse AVHRR gridded data set, drifting buoys, observing ships, and anything else that comes in over the GTS (Global Telecommunication System, a meteorological agency observations network). An OI assimilation system is used with horizontal and vertical correlation length scales [7].

5.3.2   ENSO Forecast Models

SST assimilation has been widely used for coupled ENSO forecast models (e.g. [18], [117], [141], and [142]). In these initialisation problems only horizontal correlations are assumed. Chen et al [18] and Rosati et al [117] nudge the modelled SST towards an observed SST field, often simultaneously with nudging towards the observed wind fields. Syu and Neelin [141] daily inserted Reynolds' SST anomaly information into the top three upper ocean layers and Tang and Hsieh [142] used a 3D Variational approach (although actually 2D because there are no vertical correlations). It was often found in these studies that the SST assimilation led to imbalances between the thermal and dynamical fields. This is because it does not correct the thermocline, the sub-surface thermodynamic structure which is governed primarily by the wind stress. Also large systematic differences in the spatial distribution of variance between the model SST field and the observed SST field have been noted. With the assimilation of observed SST, the structure of the model SST is quickly forced to resemble its observational counterpart. However, the model adjustment is relatively slow, especially for adjustment of the thermocline, which mainly determines the variability of SST anomalies in the equatorial central and eastern Pacific.

To alleviate the above problems Tang et al [143] and [144] proposed a new system which involved assimilating two proxy datasets, SST and sub-surface thermal data, into the ocean model. The proxy SST is given a similar variance distribution to the

model SST, but retains the observational information in the temporal variability. This is so that observational forcing was not made too strong in the regions where the model SST has a significantly different variance structure. In this 3D-Var assimilation scheme a linear relationship between any two neighbouring depths was derived using singular value decomposition and then applied to estimate the temperatures at deeper levels using the temperature analyses of shallower levels.

5.3.3 Shelf Sea Models

The transfer of information vertically through the water column was viewed as having greater importance than horizontal smoothing in a shelf sea assimilation scheme by Annan and Hargreaves [4]. They used a statistical interpolation scheme to assimilate AVHRR data as innovation increments into the mixed layer. The satellite data are compared with local in-situ observations to derive local error statistics, any bias in the satellite observations is then removed before the data are assimilated and the variance is used in the assimilation scheme. These error statistics include averaging over the mismatch between skin and bulk temperatures. This difference can vary widely from night-time to daytime and so the authors sensibly produce different error statistics for day and night to compensate for this. However such generalised statistics will ignore the differences that develop between various wind and insolation regimes. Annan and Hargreaves make the following assumptions when implementing their scheme. Firstly, that horizontal correlations are small enough to be ignored. Secondly, the turbulent kinetic energy is close to a quasi-equilibrium level and so temperature can be adjusted independently of the turbulent kinetic energy. Thirdly, that the water column is well mixed above and below the thermocline. The shelf sea model they used had a vertical resolution of order 5 metres.

This one-dimensional scheme has been thoroughly tested in the Proudman Oceanographic Laboratory Coastal Ocean Modelling System (POLCOMS) and the results are discussed by Andreu-Burillo et al in [3]. They concluded that for the Irish Sea and at scales resolved by the model, the assimilation improves the modelled SST. However, they also added that for a shelf sea context, using only IR SST observations, the prob-

lem could not be adequately approached in a one-dimensional framework. They noted that only errors in the air-sea heat flux are accounted for and that other sources of errors such as modelled horizontal advection and diapycnal mixing are not corrected. The results were shown to be particularly poor in shallow areas where the three-dimensional thermal distribution is strongly affected by tidal excursions and river inflow. Without any horizontal correlations, patches of observational data voids, due to cloud cover led to unrealistic gradients being generated after the assimilation, resulting in the creation of spurious currents on occasions.

5.3.4 Restoring Boundary Conditions

Traditionally ocean general circulation models are forced by restoring boundary conditions, wherein the top model temperature is restored to a target surface temperature to calculate the heat flux at the surface. This technique was originally proposed by Haney [51], but is often referred to as Barnier relaxation [6]. The surface heat flux, Q, over the ocean is approximated by the relaxation of the ocean surface temperature, θ_{surface}, to a target temperature, $\theta^*_{\text{surface}}$, usually observations or climatology, with the equation

$$Q = \lambda(\theta^*_{\text{surface}} - \theta_{\text{surface}}), \tag{5.10}$$

where λ is the feedback coefficient. The errors associated with this relaxation towards surface observations are discussed by Killworth et al in [69] and an improvement suggested by Kamenkovich and Sarachik [61]. In the literature this is never described as data assimilation, although clearly Equation (5.10) could be seen as making a correction to a background heat flux (here zero) based on model observation differences of SST, and as such could be viewed as a crude data assimilation algorithm.

Indeed a recently published data assimilation method by Manda et al [78] uses a similar surface restoring condition

$$Q = Q^* + \frac{\rho c_p \Delta z_1}{\tau} \left(\theta^* - \theta_{2.5\text{m}} \right). \tag{5.11}$$

The prescribed heat flux, Q^*, is corrected by an observed SST, θ^*. Here ρ denotes seawater density, c_p specific heat of seawater, Δz_1 the thickness of the first model layer

(5 metres), $\theta_{2.5\text{m}}$ the temperature in the first layer of the model, and τ the restoring time scale. This nudging method is validated as a feasible method with an ocean circulation model that incorporates a strongly nonlinear mixed layer model. Although this nudging method is statistically sub-optimal it was found by Manda et al [78] to have comparable skill to the statistically optimal method of the Ensemble Kalman Filter (EnKF). This is because they work in a similar way; the EnKF corrects the surface layer temperature and allows the subsurface layers to be adjusted according to the evolving model, whereas the nudging method corrects the temperature in the first layer as well as the surface heat flux, and again the subsurface temperatures adjust according to the evolving model. This is an important finding as the computational cost of the nudging method is a fraction of that required to implement an EnKF method.

5.3.5 Operational SST Products

Reynolds

The Reynolds SST analysis products [112], [111] are very popular and widely used (e.g. the ECMWF ocean model relaxes towards the Reynolds SST). The analysis uses 7 days of in-situ (ship and buoy) and satellite SST. The analyses are produced weekly and daily using optimum interpolation (OI) on a $1°$ grid. The data errors from ships are almost twice as large as the data errors from buoys or satellites and these error statistics are included as part of the OI scheme. The bias in satellite observations (when compared with in situ data), caused from stratospheric aerosols from volcanic eruptions [110], are removed before the assimilation by using a Poisson technique to provide a smooth correction field. Bias correction of all input data to the analysis procedure is critical to obtaining a valid output [111]. The daytime satellite data have been assigned higher error values than the night-time data. The diurnal cycle is not resolved in the OI analysis, and any diurnal signal will appear as noise to the analysis. Additional errors in the satellite data can occur when the assumed correlation between skin and bulk temperatures begins to break down. In this case, the satellite retrieval algorithm also breaks down.

HadISST

The UKMO Hadley Centre for Climate Prediction and Research (Hadley Centre) Sea Ice and Sea Surface Temperature data set, HadISST1, combines monthly globally complete fields of SST and sea ice concentration on a 1° latitude-longitude grid. The SST fields are created using a combination of in-situ and satellite measurements. The in-situ data are averaged and interpolated into a globally complete field, using reduced space optimal interpolation (RSOI) [63]. This field is then used to correct satellite derived SST data, for the purpose of removing biases, before its inclusion in HadISST1. These biases include the residual differences between skin and bulk SSTs and contamination by undetected aerosol and clouds. The satellite and in-situ fields are then averaged together and reconstructed as a 2° spatial resolution anomaly field. To make HadISST1 globally complete the gaps in the combined in-situ/satellite SST data are filled by RSOI. The satellite data come from two different sources, AVHRR and AATSR; O'Carroll et al [94] presents an overview of the influence these have on the HadISST global analyses. The AVHRR brightness temperature measurements have been tuned by a regression onto a set of drifting buoys and are thus considered equivalent to a one metre bulk temperature, whereas the AATSR are considered to measure a skin temperature. In the case of AATSR data a 1-D mixed layer ocean model forced with 6 hourly NWP fluxes is used to derive skin to bulk (one metre) temperature differences at the observation time, if this difference is greater than 0.2 °C then the observation is flagged. Details of this processing scheme are provided in [52].

OSTIA

The Ocean Sea Temperature and Ice Analysis (OSTIA) is a daily operational analysis product being developed at the National Centre for Ocean Forecasting (NCOF) [131]. It has a 1/20° resolution and uses GHRSST-PP data (SEVIRI, TMI, NAR, AVHRR, ATSR, and AMSRE) almost exclusively. Currently this product is produced without an ocean model and is purely persistence based. It fuses all observations over a 24-hour period valid from midnight GMT to midnight GMT each day. Daytime observations recorded with local wind speed less than 6 ms^{-1} are flagged, as they are considered

likely to be 'corrupted' by a diurnal signal. This is clearly not the ideal situation when wind speeds under $6 \, \mathrm{ms}^{-1}$ account for over 40% of the total occurrence of hourly averaged wind speeds over the ocean (see Figure 2.1 in [79]).

5.4 SST Assimilation Experiments in the GOTM

5.4.1 Introduction

The graphs of Figures 4.3, 4.4, and 4.6 show that the modelled SST on occasions drifts away from the observed SSTs and over or under estimates. The availability of SST observations would allow these errors to be constrained and corrected for. In this next section we use local midnight SST observations in assimilation routines. These data assimilation schemes were developed to use this additional piece of information (the daily SST observation) to improve the state of the system. We seek to achieve this by adjusting the temperature profile in a physically consistent and smooth manner. The aim is to utilise information content in the observations to highlight shortcomings in model processes and provide insight into how these may be improved, in the hope of reducing future model bias.

With the introduction of observations the first question to ask is whether the model can bring additional skill to the SST estimation, compared with the observations. The null hypothesis, assuming persistence from the daily observations without any physical model (using yesterdays SST observation to predict tomorrows SST), should provide a lower bound for the estimation skill. Table 5.1 compares results from a model simulation with that of persistence only. These control simulations are initialised with observations at the start only and forced with observed down-welling SWR and LWR observations and air-sea fluxes calculated from the surface meteorology.

It can be seen that in all cases persistence from the daily observations give better SST estimation than the model by itself can provide. However the persistence assumption leads to zero diurnal warming estimates, so in this respect the model by itself is shown to provide better estimates of diurnal warming in all cases. In data assimilation the aim is to merge observations with the dynamical model to produce an accurate

	RMS Error	
	SST	Diurnal Warming
COARE		
Modelled	0.29	0.36
Persistence	0.27	0.58
Arabian Sea		
Modelled	0.71	0.26
Persistence	0.29	0.56
Subduction		
Modelled	0.66	0.18
Persistence	0.14	0.28

Table 5.1: *RMS errors of SST and diurnal warming estimates, in °C, comparing model simulations with estimates based on persistence of a midnight SST observation.*

analysis. In this chapter the aim is to use the observations to prevent model drift, but preserve the dynamic evolution of SSTs over the day as predicted by the model equations. The credibility of these attempts will be assessed by the reduction in the root mean square errors given in Table 5.1.

5.4.2   Direct Insertion

A univariate data assimilation scheme is now described whereby the SST observation from the mooring site is directly inserted into the model. An increment between the SST observation and the model temperature at the observed depth (0.45m for COARE, 0.17m for Arabian Sea, and 1.0m for Subduction) is found each day at the time of the observation (midnight). This increment is then used to adjust all model temperatures within the mixed layer. This can be written mathematically in the formalism of data assimilation as follows

$$\theta_{k+1} = f_k(\theta_k, u_k), \qquad k = 0, \ldots, N-1. \tag{5.12}$$

With $\theta \in \mathbb{R}^{150}$ denoting the sea temperatures at 150 model levels, $u_k \in \mathbb{R}^n$ are the inputs to the system (e.g. surface forcing) at time t_k and $f_k : \mathbb{R}^{150} \times \mathbb{R}^n \rightarrow \mathbb{R}^{150}$ is the discrete nonlinear function describing the evolution of the model temperatures from time t_k to time t_{k+1}. We have a single observation of the SST at time t_k which is related to the state θ_k by equation

$$y_k = h_k(\theta_k), \qquad k = 0, \dots, N-1, \tag{5.13}$$

where $h_k : \mathbb{R}^{150} \rightarrow \mathbb{R}$ is a function that maps the state space onto the observation space; in this case a linear grid interpolation from the nearest model grid depths to the observation depth. We then define our state estimator as follows

$$\theta^a_{k+1} = \theta^b_{k+1} + K_{k+1}(y_{k+1} - h_{k+1}(\theta^b_{k+1})), \tag{5.14}$$

for $k = 0, \dots, N-1$. The column vector $K_{k+1} \in \mathbb{R}^{150}$ has column entries $K(i)$ defined by

$$K(i) = \begin{cases} 1 & \text{for} \quad z_{\text{MLD}} < z^i \leq z^{150} \\ 0 & \text{for} \quad z^1 \leq z^i \leq z_{\text{MLD}} \end{cases} \tag{5.15}$$

where z^i represents the model depth at grid level, i, with 150 being the top layer, nearest the surface, and z_{MLD} represents the MLD derived from modelled temperatures as defined in Section 4.3. The SST increment is determined by $y_{k+1} - h_{k+1}(\theta^b_{k+1})$.

This direct insertion method is based on physical assumptions that the temperatures within the oceanic mixed layer, defined by the depth of the mixed layer at local midnight, are well mixed, so that any temperature signal at the near surface will be merged into the near homogeneous layer through mixing. The SST increment will represent the temperature error throughout the mixed layer. It is assumed that the MLD is correctly known and that the temperature error was caused by incorrect heat fluxes into this mixed layer, whether by advection or surface boundary fluxes. The TKE is considered close to a quasi-equilibrium level and so the adjustment to temperatures happens almost instantly and the TKE is assumed to remain unchanged throughout the assimilation. It is expected that after assimilation the improvement in surface temperatures will lead to more accurate fluxes and thus reduce future drift.

The success of the assimilation method can be viewed in Figure 5.1 where a drift, as shown previously in Figures 4.3, 4.4, and 4.6, is no longer seen at any of the mooring sites. The model simulations use a fixed cloud value of one half, to introduce greater error in the model and make the assimilation routine work harder. It was found that the SST RMS error was reduced by $0.48\,°C$, $0.88\,°C$ and $0.36\,°C$ for the sites COARE, Arabian Sea, and Subduction respectively. For all cases the errors are significantly reduced below those values given in Table 5.1. However the error associated with the SST diurnal warming remain virtually unchanged in all cases. This is because only the initial condition is changed, the starting point of the days warming has improved, but the forcing over the day remains virtually unchanged (slight changes in latent and sensible heat flux and LWR occur because of the adjusted SSTs). The key factors that affect the shape and strength of the diurnal warming are the solar radiation, effected by changes in cloud cover and the wind stress, both of which remain fixed in this assimilation method.

The feedback between the atmosphere and ocean is represented by using the modelled interfacial (skin) temperature in calculating the LWR and latent and sensible heat flux. The improvement in these fluxes with the new temperatures at the Arabian Sea site is seen in Figure 5.2 and is particularly strong after day 260. A comparison with Figure 4.4 at this time shows the SST of the control to be significantly warmer than the observations. This warming bias causes the SST of the model to rise above air temperatures (not shown), thus changing the magnitude and direction of the sensible heat flux. The cooling of the SST in the assimilation run reduces the magnitude of the calculated long-wave radiation and latent heat flux which produces the divergence at day 260 in Figure 5.2.

5.4.3 Cloud Correction

At the mooring sites no observations of cloud cover were recorded and unless the observed SWR and LWR values are used to force the model this can be a major source of uncertainty in the modelled SST on both diurnal and longer timescales, as demonstrated in Section 4.6. In using the direct insertion method improvements in
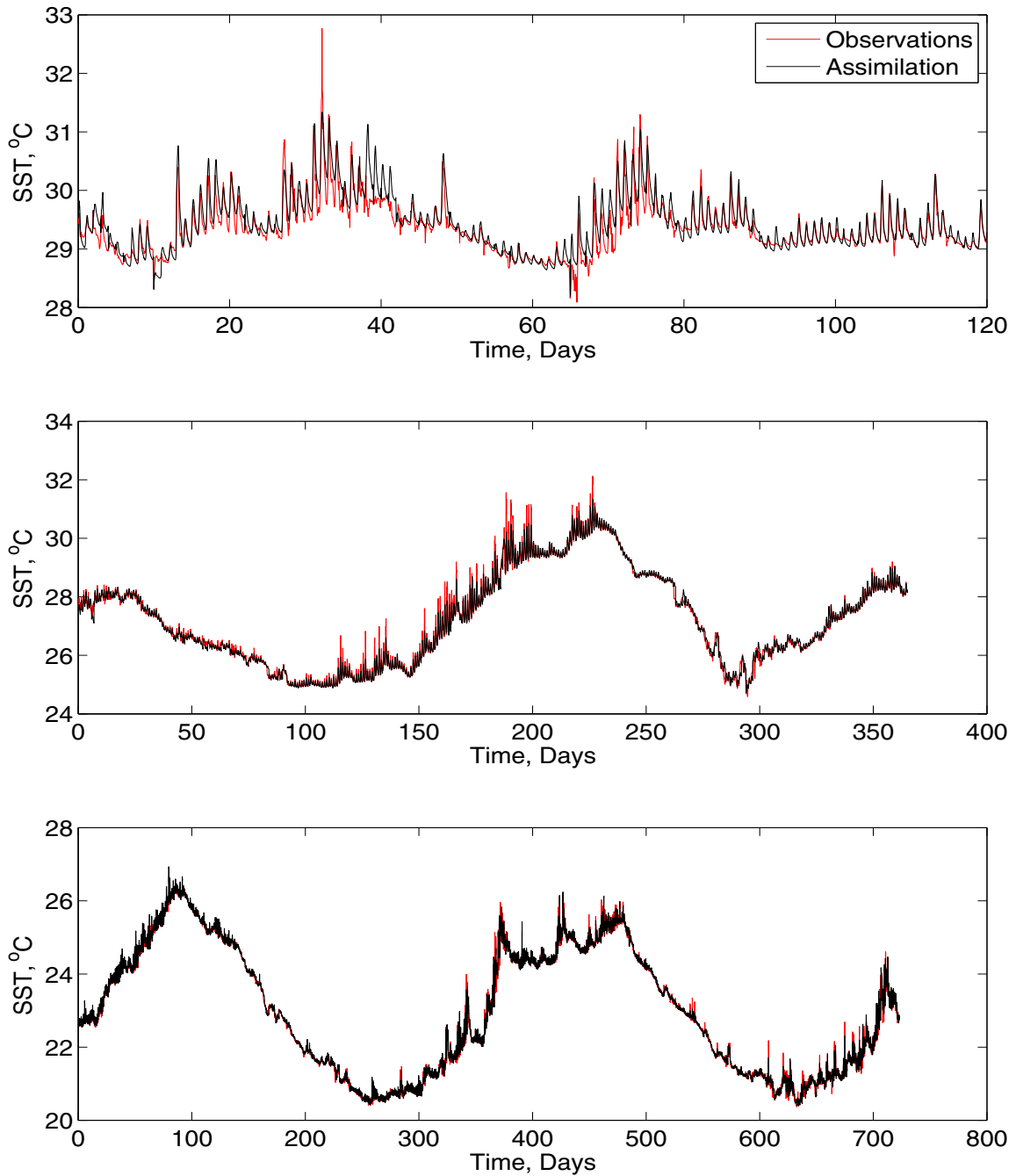
Figure 5.1: *Time series comparisons of the SST observations with the modelled SST using the direct insertion method. From top to bottom: COARE, Arabian Sea, and Subduction.*
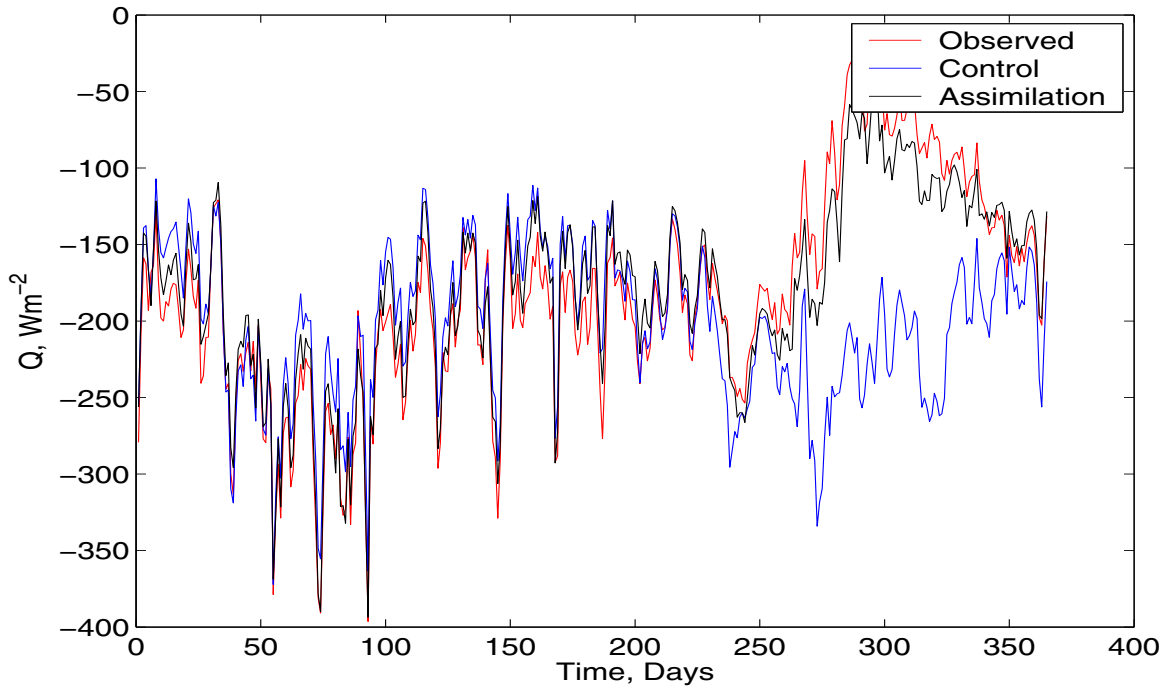
Figure 5.2: *Time series comparisons at the Arabian Sea site of the sum of the LWR, latent heat, and sensible heat fluxes calculated from the control run, the assimilation run, and observations (using the air-sea flux algorithm with all observed temperatures and observed downward LWR).*

the SST have been realised over the whole time period; however, estimates of the diurnal warming have remained unchanged. It was shown in Section 4.6 that the cloud forcing over the day was critical in the development of the diurnal cycle. If this can be improved during the assimilation then diurnal warming estimates will also improve. As was explained in Section 1.5 diurnal warming is highly sensitive to wind speeds; however, due to the high quality anemometer observations (typical instantaneous error of 5%, see Table A2 in [154]) this was not considered a major cause of the errors. In this next assimilation routine it was intended that the SST observations could be used, not only to correct for past errors in fluxes, as with the direct insertion method, but actually to account for the flux errors and reduce the likelihood of the same error occurring again.

In this cloud correction data assimilation algorithm it is assumed that all flux error

is caused by uncertainty in the daily cloud cover value. When the SST observations are assimilated using the direct insertion method heat is supplied to, or extracted from, the system. This can be quantified as follows

$$H = c_p \rho_0 \int_0^{24} \int_{z_{\mathrm{MLD}}}^{150} \left(\frac{\partial \theta^a}{\partial t} - \frac{\partial \theta^b}{\partial t} \right) dz dt. \tag{5.16}$$

A further determination can be made as to whether these errors in the heat budget accumulated over the day could have been rectified by an improved heat flux into the ocean for that day. The associated cloud value change needed to provide this rectification in heat flux is calculated as follows

$$S = \frac{-H}{0.62 \left(1 - f\left(z_{\mathrm{MLD}}\right)\right) \int_0^{24} I_\downarrow \left(1 - \alpha\right) dt}, \tag{5.17}$$

based on the Reed formula (see Section 3.2). This derivation assumes that the cloud has influence only on the SWR, i.e. neglects the much smaller cloud forcing component in the LWR. It also assumes that the surface heat flux without solar radiation, Q, does not escape below the MLD, z_{MLD}, because of the mixing at the base of the layer. However, a small fraction, $f\left(z_{\mathrm{MLD}}\right)$, of the net surface solar radiation, I, does penetrate below the mixed layer and this is taken into account in Equation (5.17). From Equation (5.17) an optimal cloud value over the day can be calculated

$$n_k^a = n_k^b + S_k, \qquad k = 0, \ldots, N - 1, \tag{5.18}$$

and a check is made to ensure the physical limits $0 \leq n_k^a \leq 1$ hold. This estimated cloud value then becomes the best estimate for the next day

$$n_{k+1}^b = n_k^a, \qquad k = 0, \ldots, N - 1. \tag{5.19}$$

This is essentially a sequential data assimilation scheme to estimate model parameters, where S is a function of the SST increments.

Figure 5.3 gives an indication as to how well we are able to estimate cloud cover values from the SST observations. The graph reveals day to day variations in the SWR obtained using the assimilation, whereas in the control there is none. The variations in cloud amounts introduced by the assimilation routine show some degree of correlation with those of the observed values. The assimilation, however, is limited by the

constraints of the SWR parameterisation, as it has a tendency to produce cloud values that oscillate between full cloud and no cloud.
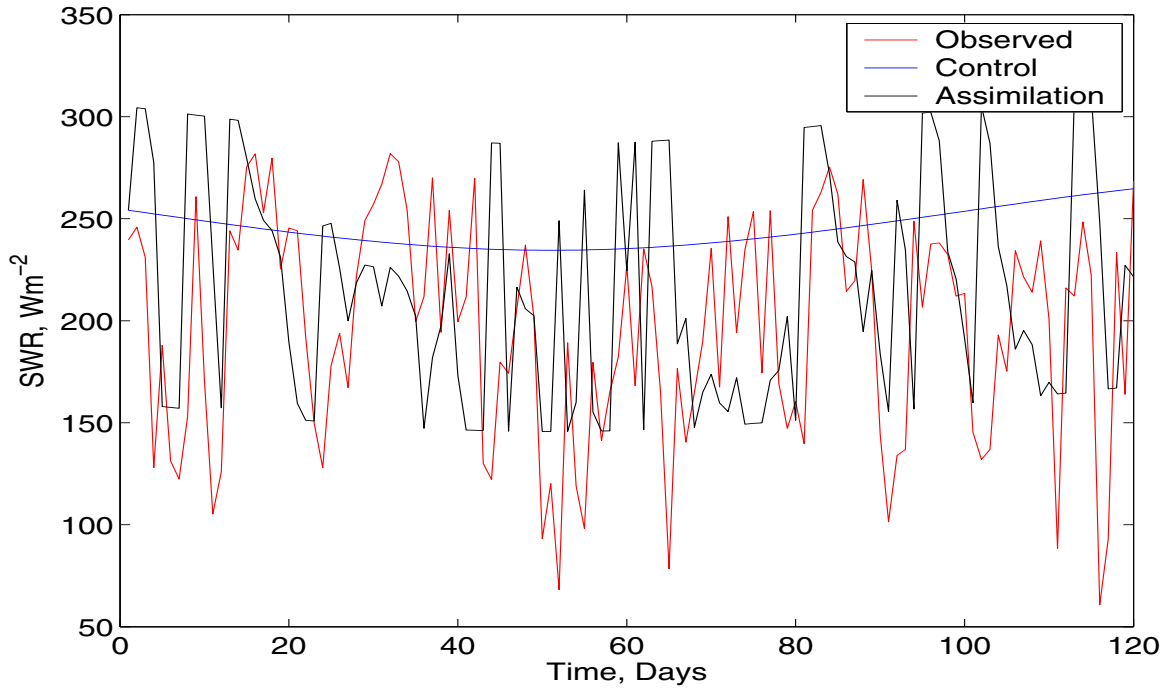
Figure 5.3: *A comparison of the daily mean total SWR at the COARE site using the observed downward radiation (red), the Reed formula with constant cloud value of one half (blue), and the cloud adjustment assimilation scheme (black).*

Using this cloud correction method to determine cloud values is not necessarily always physically realistic as the cloud amount is also compensating for other causes of error present in the model. This is particularly true when implementing the scheme at the Arabian Sea site where it is known that on certain occasions the major source of error is due to advection.

5.4.4 Advection

A major source of error in using the 1-D model to estimate SSTs is that created by advection. A comparison of the one-dimensional heat budget with the observed heat content changes, as given in Figures 5.4 and 5.5, is a good way of assessing this influence.

For the Arabian Sea (Figure 5.4) there are occasions (e.g. days 0–10, 25–40, 40–80, and 270–280) when changes in the 1-D budget are too large and advection plays a major role; corrections to mixed layer temperatures based on surface observations do not improve the heat budget. This is not true however at the Subduction site (Figure 5.5) where the SST assimilation in the mixed layer is able to constrain accurately all temperatures in the water column. This is because large advection events below the MLD are not in occurrence at the Subduction site.

Figure 5.4: *The temporal evolution of total column (to a depth of* $150\,m$*) integrated heat content calculated from observed and modelled temperatures at the Arabian Sea site.*

Profile Assimilation

The results from previous sections demonstrate that temperatures below the mixed layer are decoupled from surface temperatures and therefore cannot be adjusted in an SST assimilation scheme. It has also been shown that at the Arabian Sea site, advection into the water column does occur below the MLD and so the whole profile cannot be

Figure 5.5: *The temporal evolution of total column (to a depth of 150 m) integrated heat content calculated from observed and modelled temperatures at the Subduction site.*

sufficiently rectified by the SST assimilation. Therefore for accurate sea temperature modelling using a 1-D model at this site, re-initialisation of the temperature profile is needed, particularly after advection events. Presented in Figure 5.6 are the results of the improvement in the total column heat content at the Arabian Sea site when the full temperature profile is assimilated every 30 days. This highlights the importance of temperature information below the MLD and illustrates the necessity of temperature and salinity profiles, for example from ARGO floats [47], as well as SST observations in global ocean modelling and data assimilation.

To model diurnal warming on a day to day basis with limited interference from advection the correct initial condition is needed. Model simulations were performed where the observed sea temperature profiles were used to initialise the model at local midnight each day. Thus the diurnal cycle is allowed to develop each day from the given night time profile. The results from these simulations are given in Table 5.2. The results can be compared to those in Table 4.5 where the initial profile is only
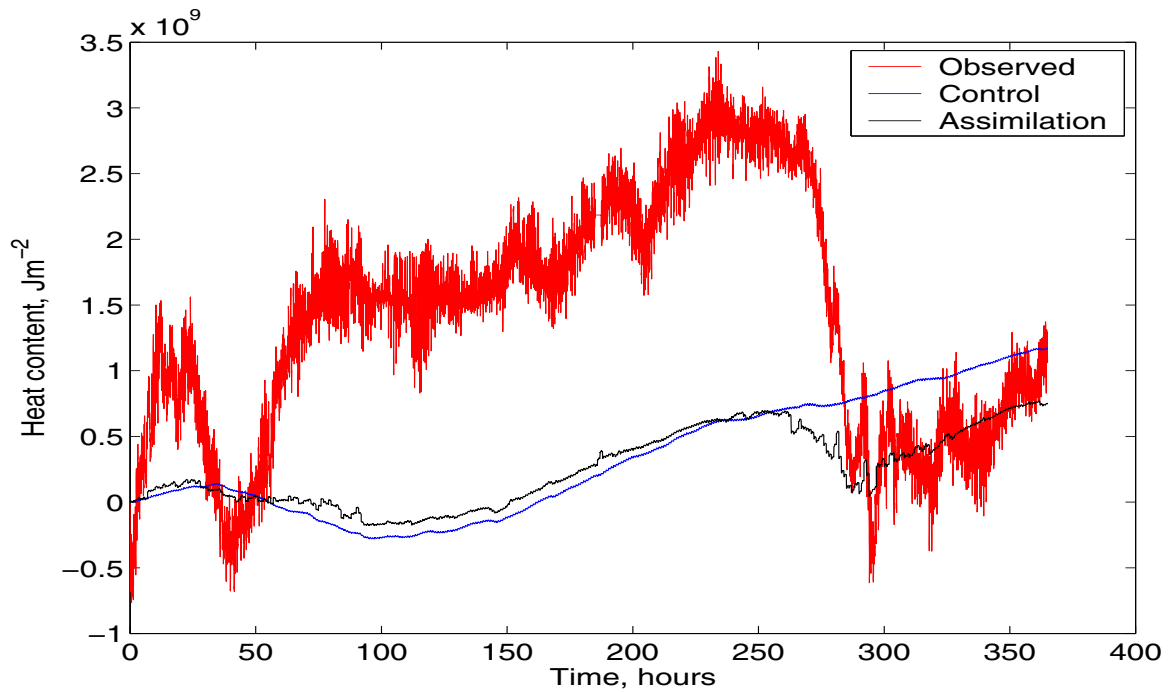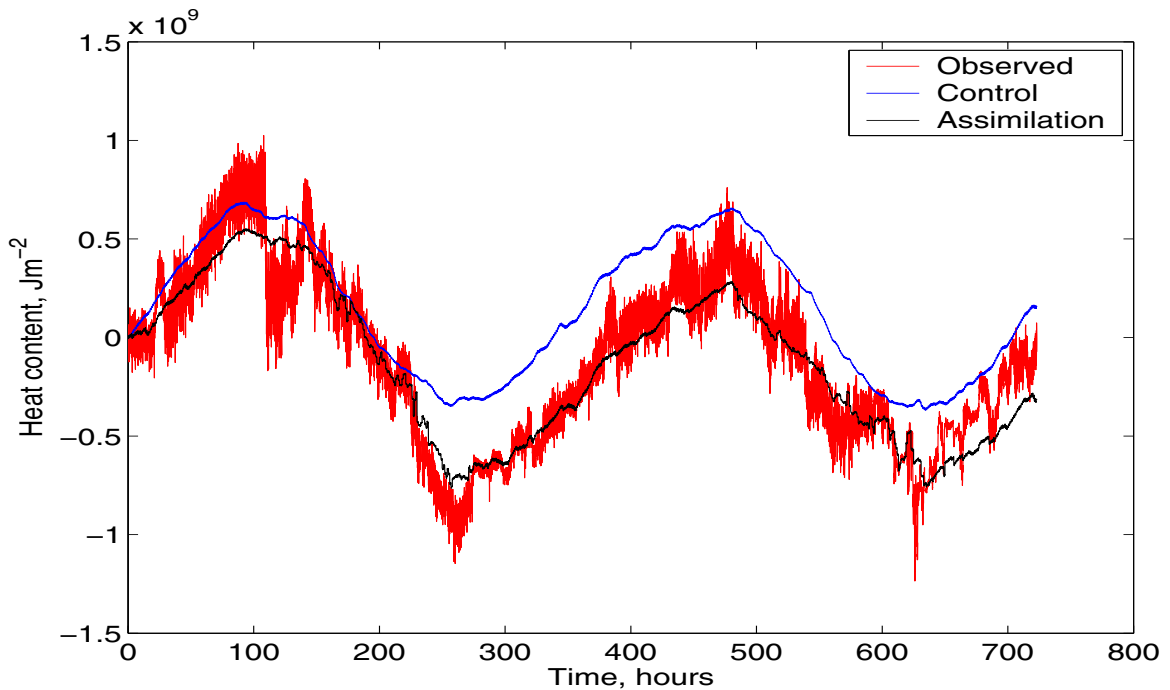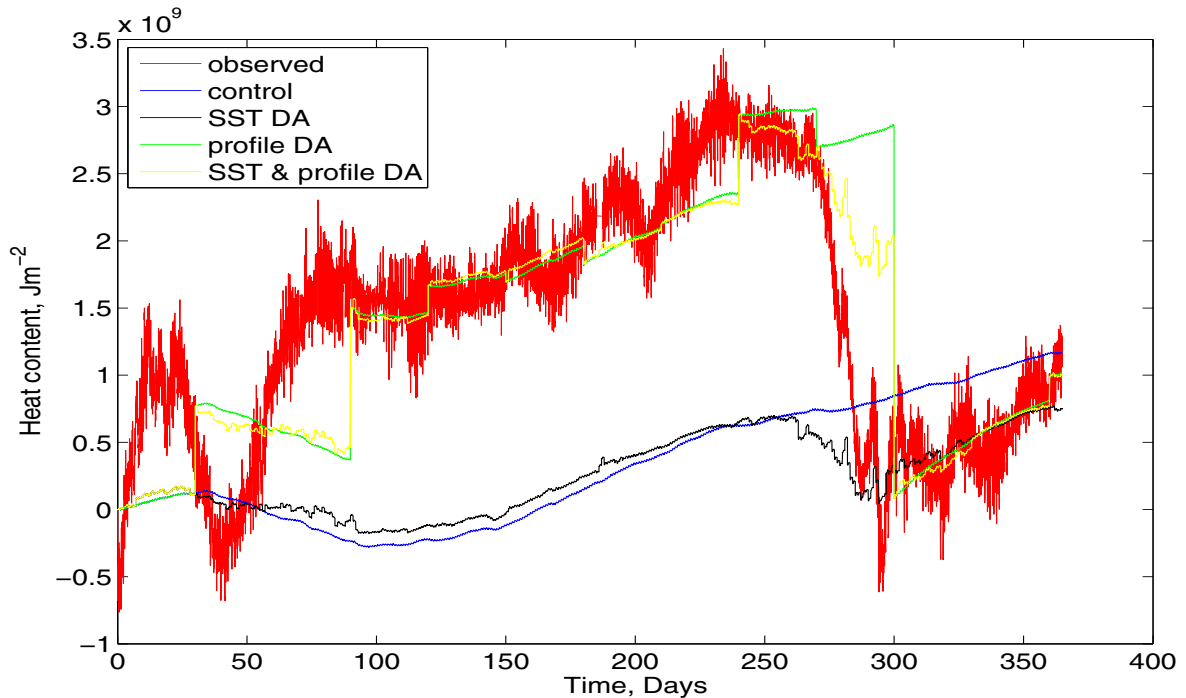
Figure 5.6: *The temporal evolution of total column (to a depth of $150\,m$) integrated heat content calculated from observed and modelled temperatures at the Arabian Sea site.*

given at the start. The RMS errors in SST over the whole period are significantly reduced, as would be expected as errors are only allowed to build up over a 24 hour period. They are also much lower than errors from the daily persistence as recorded in Table 5.1; this is especially the case at COARE and the Arabian Sea where the diurnal warming effects are much greater than at the Subduction site. The diurnal warming errors have slightly improved at the COARE and Arabian Sea sites, but as explained earlier in this chapter the initial condition is not a major determinant of the magnitude of diurnal warming, far more important is variability in SWR and wind stress. Large improvements are seen in the MLD, this is especially the case at the Arabian Sea where advection was known to be a major cause of MLD errors during the two monsoon seasons (see Figure 4.4 b). The stratification measure also shows good improvement with the 10 m and near surface temperature difference kept well below two tenths of a degree in RMSE.

	RMS Errors			
Site	SST (°C)	Diurnal Warming (°C)	MLD (m)	Stratification (°C)
COARE	0.19	0.34	13.4	0.17
Arabian Sea	0.15	0.24	11.06	0.13
Subduction	0.13	0.2	21.79	0.14

Table 5.2: *Statistics from comparisons derived from observations and model simulations initialised daily at the mooring sites.*

Results are also included when daily initialisation was used with 6 hourly forcing, as described in Section 4.7. These are presented in Table 5.3 and should be compared with Table 4.8. The differences are similar to those discussed above.

	RMS Errors			
Site	SST (°C)	Diurnal Warming (°C)	MLD (m)	Stratification (°C)
COARE	0.19	0.36	15.94	0.18
Arabian Sea	0.19	0.3	12.99	0.17
Subduction	0.14	0.22	24.62	0.15

Table 5.3: *Statistics from comparisons derived from observations and model simulations forced with 6 hourly data and initialised daily at the mooring sites.*

5.4.5   Mixed Layer Adjustment

The use of interactively calculated fluxes provides a feedback to the MLD. For example, if the MLD diagnosed from model output is too deep and there is a positive net heat flux into the ocean then the SST estimated is likely to be too cool, as the heat is mixed over a larger volume of water in the model than in reality. This cooler SST will then provide a weaker heat loss of LWR and latent and sensible heat fluxes, thus leading to greater stratification of the upper ocean and shoaling of the mixed layer. Therefore interactively calculated air-sea fluxes create a natural balance in the model between the

temperatures, air-sea fluxes, and ocean mixing. An example, at the Arabian Sea site, of how the SST assimilation can affect the MLD is shown in Figure 5.7. As observed in Figure 5.2 at around day 260 there is a large difference in the sum of LWR and latent and sensible heat fluxes calculated by the control run and the model run with data assimilation. This change in the heat flux total produces the shoaling in the MLD at around day 290 and thus better resolves the observed MLD at this time. However, this type of change in the MLD is not seen at other times of the year.
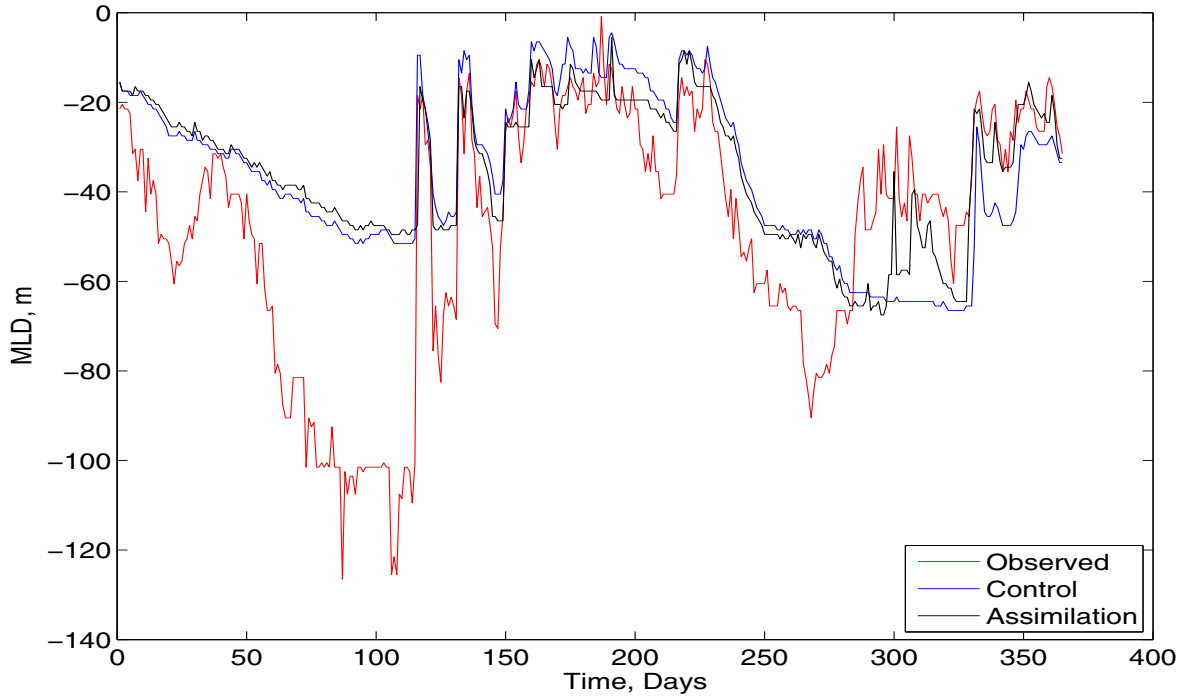
Figure 5.7: *The daily maximum mixed layer depth at the Arabian Sea site derived from observed temperatures (red), modelled temperatures from the control run (blue), and modelled temperatures with the direct insertion data assimilation scheme (black).*

The mixed layer heat budget can be approximated by the simple expression

$$c_p \rho_0 z_{\mathrm{MLD}} \frac{\partial \theta_a}{\partial t} = F, \qquad (5.20)$$

where F is the total surface heat flux, z_{MLD} the mixed layer depth, and θ_a the mean mixed layer temperature. If we fix F, but have two different MLDs, say z_{MLD}^1 and z_{MLD}^2 such that $z_{\mathrm{MLD}}^2 > z_{\mathrm{MLD}}^1$ then it would be expected that the change in mixed layer

temperatures would be greater in case 1 than case 2, i.e. $\left|\frac{\partial \theta_a^1}{\partial t}\right| > \left|\frac{\partial \theta_a^2}{\partial t}\right|$. Following this principle, at the Arabian Sea site during the NE Monsoon period, when the MLD is much shallower in the model than in reality (days 30–100), the change in temperature over a given day during this period should be greater in the model. This is a time when the temperatures are cooling and the ocean is losing heat and therefore a shallower MLD in the model leads to a faster cooling in mixed layer temperatures than is observed. This can indeed be seen in the SSTs from Figure 4.4.

This change is observable by using the SST observations and therefore a data assimilation routine could have the potential to rectify the MLD in the model. Equation (5.20) can be integrated over a 24-hour period and approximated by

$$c_p \rho_0 z_{\text{MLD}} \left(\theta_a(24) - \theta_a(0)\right) = \int_0^{24} (I_0 + Q)\, dt. \tag{5.21}$$

In the direct insertion method of Section 5.4.2 the mixed layer temperatures are initialised every 24 hours and so $\theta_a(0)$ is identical in the analysis and the background field; however, because of the assimilation, $\theta_a^a(24)$ is different from $\theta_a^b(24)$. It is assumed that the integrated fluxes are correct and so if they are kept fixed then a rearrangement will give

$$z_{\text{MLD}}^a = z_{\text{MLD}}^b \frac{\left|\theta_a^b(24) - \theta_a(0)\right|}{\left|\theta_a^a(24) - \theta_a(0)\right|}. \tag{5.22}$$

However, it was found that this scheme failed to improve the modelled MLD or the estimated temperatures. It may be that the mixed layer heat budget, Equation (5.20), is an over simplification for this purpose. More complexity could be added by allowing the MLD to evolve over the time period, and by taking into account the reduction in heat flux because of the penetration of SWR below the diagnosed MLD. Perhaps when the profile is corrected an adjustment in the TKE is also needed. Further experiments applying this principle on different timescales could also be tried. An area of future work is to utilise information that could be gained by comparing the evolution of modelled SSTs with those from observations, which is thought could provide insight on MLD. It is believed that this could become an effective method in which the structure of the temperature profile could be adjusted in a data assimilation method using only SST observations.

5.5 Summary

In this chapter we have given a brief introduction to data assimilation in general and provided an in depth review of the present state of SST data assimilation. Areas of weaknesses in these schemes are identified; these include scant attention given to the diurnal cycle of SSTs present in many observations and the lack of vertical correlations to spread surface information down into the water column. An important and open area of research is how information from surface temperature observations can be transfered deeper into the water column to provide information on temperatures at depth. Adjusting sea temperatures, which are prognostic variables in ocean models, in the assimilation can lead to imbalances between the thermal and the dynamical fields, and this issue needs to be further addressed.

With these issues in mind work is presented on the development of various data assimilation schemes. These schemes combine output from the modified GOTM and daily midnight SST observations at the mooring sites. It is shown how the availability of a daily SST observation for assimilation vastly improves SST estimation. In the direct insertion method the SST increment (model-observation difference) is used to correct all temperatures within the mixed layer. Through this procedure increased accuracy of the estimated SSTs provide improvements to the calculated air-sea fluxes and thus reduce the likelihood of future error. However this method is not able to improve the model's ability to replicate the diurnal variability of near surface temperatures. It was shown in Chapter 4 that a major cause of uncertainty on diurnal and longer timescales is the cloud cover value. In this chapter a sequential parameter estimation assimilation scheme is described that uses the SST observations to correct errors in fluxes by estimating an 'optimal' cloud cover value for each day. However it is was found that on some days the errors in the fluxes could not be accounted for by changes in cloud cover alone. Another source of possible error is the reproduction of the mixed layer depth, which can be wrong due to poor mixing parameterisations and the effects of advection. It is not clear how SST observations can provide information on temperatures below the mixed layer depth, and therefore on occasions profile

information is needed in order to constrain ocean heat content. Nevertheless a series of SST observations in time may contain information on the depth of the true mixed layer, although how this could be utilised was not established. A major problem with some of the assimilation methods developed in this chapter was the attribution of error to a single cause. At these various sites and at different times numerous sources of temperature errors have been identified. These include advection, cloud cover, and incorrect MLDs; however, it is very difficult to attribute a single daily SST error to a particular process. Therefore at this stage the best that can be done is to make corrections to mixed layer temperatures based on SST measurements, and whenever possible use profile information to improve initialisation. In Chapter 7 it is shown how SST observations taken over the day can be used to improve the modelled estimation of diurnal warming. But before, in the next chapter, our work at the mooring sites is extended to other areas by using operational data sets.

Chapter 6

Using Operational Forcing Data

6.1   Introduction

In the next two chapters the scope of this thesis work is extended beyond the focus of a few mooring sites. The model is set-up to use contemporary NWP data sets and is utilised on a larger spatial scale. The availability of global operational forecast and analysis data at 6 hourly intervals opens the possibility of the use of the model on a much wider scale. It has been noted that these NWP fields are far from optimal for the purposes of diurnal variability modelling [84] and [52], and so there was uncertainty as to how well the model would perform compared with more accurate and higher frequency forcing data. However, these are the constraints set by NWP and we have to work the best we can within these limitations. It was highlighted in Section 4.7 how the GOTM when forced with 6 hourly mean data at the mooring sites was still able to reasonably capture the observed diurnal variability. This was achieved by taking particular care to resolve the SWR at a much finer resolution than 6 hours. In this chapter it is demonstrated how operational data sets can be used to initialise and force the GOTM and produce modelled diurnal warming estimates at many locations. The model is applied over wide areas and spatial as well as temporal structure of the diurnal warming of SSTs can be analysed.

6.2   Global Data Sets

Data are needed to initialise and force the mixed layer model in order to produce SST estimates. For the work in the next two chapters this globally available data is provided by operational forecast centres. This included NCOF/UKMO FOAM global 1° analysis data of sea temperature and salinity (at depths: 5, 15, 25, 35, 48, 67, 96, and 139 metres) at 00:00 GMT; ECMWF 1° global forecast 6 hourly integrated fluxes at 18:00, 00:00, 06:00, and 12:00 GMT of surface solar radiation, surface thermal radiation (LWR), surface latent heat flux, surface sensible heat flux, east-west surface wind stress, and north-south surface wind stress; or alternatively 10 m wind speed components, 2 m air temperatures, and 2 m dew point temperatures as well as sea level pressure. These data were obtained from the Godiva data access server at ESSC [124].

6.3   GHRSST Observations

The Global Ocean Data Assimilation Experiment (GODAE) high-resolution sea surface temperature pilot project (GHRSST-PP) [106] provides a new generation of global high-resolution (< 10 km) SST data products to the operational oceanographic, meteorological, climate, and general scientific community, in real time and delayed mode. Every day, GHRSST-PP processing systems produce SST products from several complementary satellite and in-situ SST data streams to a common netCDF format. Both integrated observation (L2P) and analysis (L4) products are available.

GHRSST-PP Level-2 Pre-processed (L2P) format data products are netCDF files containing SST data, error estimates (bias error and standard deviation) for each pixel and a series of ancillary fields to help interpret and use the SST data themselves. The power of L2P lies in the fact that all satellite SST data are presented in a common easy to use data format so that only a single input/output utility is required to start using data rather than having to re-code and maintain code for ingestion of different satellite data. Currently satellite data is available from the following: AVHRR, AATSR, TMI, AMSRE, SEVIRI, NAR, and MODIS.

Unfortunately at the moment the only data in a gridded format, which is the format

immediately usable for our purposes, is from the SEVIRI, AMSRE, and TMI. These instruments and what they measure are described in more detail below. To use the other data sets would require the implementation of a search algorithm to find the data at the locations required, but considerable additional computer time would be needed.

The L2P GHRSST-PP data products come with Single Sensor Error Statistics (SSES). The satellite observations used for this thesis have the GHRSST estimated bias removed. Each GHRSST observation is provided with a proximity confidence value. Only data with values considered 'acceptable' and 'excellent' (values 4 and 5 respectively) for the infrared observations and 'acceptable' and 'diurnal' (values 12 and 13 respectively) for the microwave observations are accepted for inclusion in this work. This choice selects observations far from any corrupting influences, such as cloud for infrared and rain for microwave, but keeps observations that are potentially affected by a diurnal signal.

GHRSST-PP L4 products are designed to provide the best available estimate of the SST from a combined analysis of all available SST data. In-situ data form an important component of the L4 process as these data are used to correct for biases between the satellite data sets. L4 products capitalise on the synergy benefits of using in-situ, microwave satellite SST, and infra-red satellite SST. The GHRSST L4 products include the UKMO OSTIA product described in Section 5.3.5.

For more information on the data processing specifications adopted for the GHRSST products see [33]. The three SST data products used in this chapter and the next are now introduced.

6.3.1 SEVIRI

Radiometric measurements from the Spinning Enhanced Visible and Infrared Imager (SEVIRI) on-board Meteosat Second Generation (MSG) satellites (from Meteosat-8, launched August 2002, onwards) are used to derive SST observations. Imaging is achieved with a bi-dimensional Earth scan from a geostationary orbit. New images for each infrared channel are available every 15 minutes. The GHRSST product picks the 'best' measurement in a 3 hour period. As an infrared measurement the images are

contaminated by cloud cover so that good quality observations are only available in clear sky conditions.

6.3.2 TMI

The Tropical Rainfall Monitoring Mission (TRMM) is a joint NASA and JAXA mission launched in November 1997 and designed to monitor and study tropical rainfall. The TRMM has a near equatorial low inclination orbit and moves from west to east providing data at varying local times between $40\,^\circ$S and $40\,^\circ$N. On board TRMM is the TRMM Microwave Imager (TMI), which is a conical scan microwave radiometer with channels at separate frequencies: 10.7, 19.4, 21.3, 37, and $85.5\,$GHz and a spatial resolution of about $50\,$km. A combination of channels are used to retrieve SST through clouds, which are nearly transparent at $10.7\,$GHz. The measurement of SST through clouds by satellite microwave radiometers was an elusive goal for many years. The early radiometers in the 1980's were poorly calibrated, and the later radiometers lacked the low frequency channels needed by the retrieval algorithm. The ability of TMI to measure through clouds is a distinct advantage over the traditional infrared SST observations that require a cloud-free field of view. Ocean areas with persistent cloud coverage are now viewed on a daily basis. Furthermore, microwave retrievals are not affected by aerosols and are insensitive to atmospheric water vapour. However, the microwave retrievals are sensitive to sea surface roughness, while the infrared retrievals are not. A primary function of the TRMM SST retrieval algorithm is the removal of surface roughness effects. Microwave and infrared SST retrievals are very complementary and can be combined to obtain reliable global data sets. Error statistics, compiled from data available at [140], are given in Table 6.1. Here the satellite observations are compared with various types of in-situ observations as well as the Reynolds SST (see Section 5.3.5).

6.3.3 AMSRE

The Advanced Microwave Scanning Radiometer for Earth Observing Systems (AMSR-E) was launched in May 2002, aboard NASA's Aqua spacecraft which has a sun-synchronous orbit. JAXA provided AMSRE to NASA as an indispensable part of Aqua's global hydrology mission. Over the oceans, AMSRE is measuring a number of important geophysical parameters, including SST, wind speed, atmospheric water vapour, cloud water, and rain rate. A key feature of AMSRE, as with TMI is its capability to see through clouds, thereby providing an uninterrupted view of global SST and surface wind fields. It measures the temperature of the top layer of water approximately $1\,\text{mm}$ thick, (θ_{subskin}). Missing data can be due to sun glint, rain, sea ice, and high wind speed ($> 20\,\text{ms}^{-1}$). Error statistics are given in Table 6.1.

Match-ups	Bias (°C)	Standard Deviation (°C)	Dates
TMI – Reynolds	0.05	0.80	01/01/98 to 18/09/06
TMI – ship engine intake	−0.03	0.77	02/09/98 to 04/11/06
TMI – moored buoy	−0.08	0.57	02/09/98 to 04/11/06
TMI – drifting buoy	0.04	0.61	02/09/98 to 04/11/06
TMI – ship bucket	0.11	0.62	02/09/98 to 04/11/06
TMI – ship hull	−0.06	0.66	02/09/98 to 04/11/06
AMSRE – Reynolds	−0.05	0.76	30/05/02 to 04/11/06
AMSRE – ship engine intake	−0.01	0.75	30/05/02 to 04/11/06
AMSRE – moored buoy	−0.02	0.50	30/05/02 to 04/11/06
AMSRE – drifting buoy	−0.02	0.54	30/05/02 to 04/11/06
AMSRE – ship bucket	0.01	0.65	30/05/02 to 04/11/06
AMSRE – ship hull	−0.04	0.69	30/05/02 to 04/11/06

Table 6.1: *Mean validation statistics calculated from near real time daily collocated data sets at [140].*

6.4 Experimental Set-Up

The availability of global operational forecast and analysis data to force and initialise the model allows the freedom to run GOTM at any and many locations. An example for July 2005 in the North Atlantic is shown in Figure 6.1. Here GOTM is initialised daily at 00:00 GMT with $1°$ global FOAM temperature profiles and is forced by using ECMWF 6 hourly integrated prescribed fluxes.
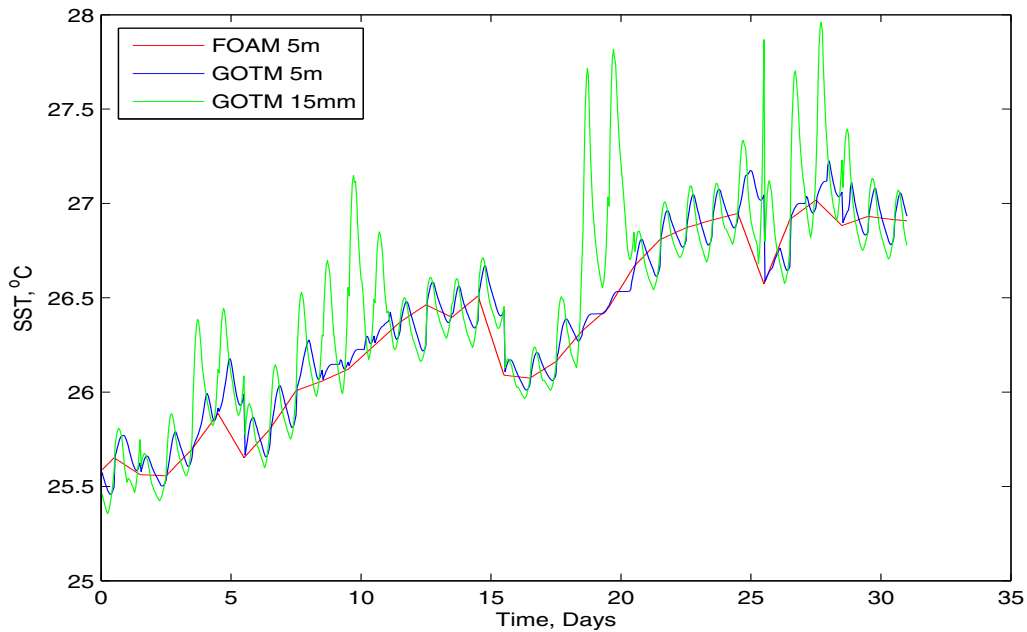
Figure 6.1: *A comparison of SSTs, at different depths, from FOAM and GOTM in the North Atlantic at (30°N, 310°E) for July 2005.*

As in Section 4.7 care was again taken to convert the solar flux to a finer time resolution to allow better representation of the diurnal cycle. In this case the ECMWF SWR is given as a 6 hourly integrated value, as opposed to a mean value as was the case in Section 4.7. The approach presented here is an improvement on similar techniques adopted by Horrocks et al [52] and Hallsworth [50]. The clear sky insolation, $I_\downarrow$, is calculated a priori, as described in Section 3.2 using equations (3.1)-(3.4), at each 30 second time step. Then to calculate the net surface SWR at each time over the day the

Reed parameterisation (Equation (3.5)) is used. Integrating this over a 6 hour window gives

$$\int_T^{T+6} I_0 dt = \int_T^{T+6} I_\downarrow \left(1 - 0.62n + 0.0019\beta\right)\left(1 - \alpha\right) dt, \tag{6.1}$$

where T are the 6 hourly forecast times. The left hand side of equation (6.1) is set equal to the ECMWF value, and Equation (6.1) can be rearranged to find an effective mean cloud value over this window,

$$n = \frac{(1 + 0.0019\beta)\int_T^{T+6} I_\downarrow(1 - \alpha)dt - \int_T^{T+6} I_0 dt}{0.62 \int_T^{T+6} I_\downarrow(1 - \alpha)dt}. \tag{6.2}$$

If it is night time, so that $\int_T^{T+6} I_\downarrow(1 - \alpha)dt = 0$, then persistence $n_k = n_{k-1}$ is assumed. A check is also made to enforce the physical cloud limits $0 \leq n \leq 1$. The net surface SWR, I_0, used in the model run is calculated using the Reed formula (3.5) with the 6 hourly cloud values derived from the 6 hourly integrated ECMWF net surface SWR as described above. The other integrated fluxes (net surface LWR, sensible heat, latent heat, and surface wind stress components) are converted to a mean over the 6 hour period and this constant value is then used in the model simulation.

In Figure 6.1 the FOAM 5 m temperatures have been linearly interpolated to clearly demonstrate how the diurnal cycle as modelled in GOTM sits on top of this base temperature that is used for initialisation each day. A diurnal cycle is seen not only in the top grid level of GOTM (0.015 m), but also a much reduced warming signal is evident at the 5 m depth.

Direct observations of individual diurnal warming signals are highly improbable as observations are not likely to coincide with the maximum and minimum daily SSTs. Therefore modelled diurnal amplitudes can only be indirectly validated by comparing modelled SSTs to individual observations at observation times throughout the day. For this reason it is essential that the model starts from an accurate initial condition, otherwise the model-observation differences will be characteristic of the initial offset rather than differences in how the modelled and observed SSTs have evolved over the day. To improve the initial condition we use the OSTIA product described in Section 5.3.5. This product represents an average of all GHRSST-PP SST derived satellite observations over a 24 hour period, excluding daytime observations recorded

in low wind speed conditions. Thus OSTIA can be seen to represent the night time temperature and is used here to initialise the model at 00:00 GMT. Work presented in this thesis is based in the Atlantic Ocean and therefore local time differences are slight; if, however, model runs were to be performed in the Pacific Ocean, for example, then an adjustment would be needed to initialise GOTM at local night time. The OSTIA value is used each day to correct the mixed layer temperatures of FOAM. The procedure is the same as that developed in Section 5.4.2. This correction was found to cause instability problems on a few occasions when OSTIA and the 5 metre FOAM temperature are very different. Under these circumstances it is uncertain how to correct temperatures below the mixed layer and so no model simulation is performed at these locations.

This type of model simulation can be run at several locations and spatial diagnostics of the output produced. A 1° latitude and longitude grid of GOTMs was run over a section of the South Atlantic Ocean for a week in northern hemisphere winter (1st–7th January 2006). The selected region is off the east coast of South America encompassing $-45\,°$N to $-25\,°$N in latitude and $300\,°$E to $330\,°$E in longitude. Preliminary model simulations found this area to have large diurnal warming variability and was thus selected for further study. Sensitivity studies are carried out and the results are presented in the next section. Further results are presented for the whole of the Atlantic Ocean with an improved model set-up and these are discussed in Section 6.6.

6.5 Sensitivity of Model to Mixing and Forcing Options

6.5.1 Turbulent Mixing Options

In these locations the sensitivity of the model to the various additional turbulent mixing options was tested. In these experiments various combinations of options are examined in order to find the optimal combination for modelling the diurnal warming of SSTs. In using a fine near surface grid (see Section 2.4) the model can become very

sensitive to the amount of mixing being generated in the top grid boxes and this is particularly true in low wind speed conditions. Under low wind speed conditions the surface stress is very slight and little TKE is generated, the model has a tendency to under produce TKE in such circumstances, but these values are of extreme importance when modelling the diurnal cycle. To prevent the extinguishing of TKE an internal wave parameterisation (see Section 2.3.4) can be included to represent internal wave activity which always leaves a background residue of TKE. To enhance mixing at the surface a wave breaking parameterisation (see Section 2.3.3) can be included. Under low wind stress conditions the type of surface boundary conditions (prescribed Dirichlet conditions or a flux boundary Neumann type condition) for TKE and dissipation can also make a difference.

The starting point was to consider modelled diurnal warming estimates of over $4\,^{\circ}\mathrm{C}$ as unlikely. The various combinations of options were tested over the selected region and chosen time period and a count was taken of the number of occurrences when the modelled diurnal warming exceeded $4\,^{\circ}\mathrm{C}$ and a record kept of the maximum value. If the model is consistently under producing TKE at the near surface then it is expected that the number of extreme warming events will increase in number and magnitude. The modelled SST, $\theta_{0.015\mathrm{m}}$, is validated against SEVIRI observations. All the results are summarised in Table 6.2. The values in parentheses indicate model results produced only from locations successfully modelled in all cases (on occasions the conditions are such that some combinations of options result in such extreme near surface warming that the model becomes unstable and crashes). This still encompasses a large number of observational comparisons (2285 SEVIRI observations used).

From the results in Table 6.2 it is clear that the internal wave parameterisation is essential; without this the TKE can vanish when wind speeds approach zero and on these occasions produce totally infeasible SST warming estimates. When using the internal wave parameterisation it appears that the Neumann boundary conditions produce slightly better results than the Dirichlet surface boundary conditions. Looking at the remaining results it seems that the use of the wave breaking parameterisation slightly inhibits the likelihood of extreme diurnal warming estimates under Neumann

Mixing Options			Results		
BC	IW	WB	RMS Errors (°C)	Max DW (°C)	Extreme DW Events
Dirichlet	no	no	0.83 (0.83)	15.84 (15.82)	102 (88)
Neumann	no	no	0.84 (0.85)	19.13 (19.13)	104 (100)
Dirichlet	yes	no	0.55 (0.55)	5.09 (5.09)	33 (32)
Neumann	yes	no	0.54 (0.54)	4.97 (4.97)	21 (21)
Dirichlet	yes	yes	0.56 (0.56)	6.20 (6.20)	39 (36)
Neumann	yes	yes	0.53 (0.53)	4.94 (4.94)	15 (14)

Table 6.2: *The effects of surface boundary conditions (BC), internal wave (IW), and wave breaking (WB) parameterisations on RMS differences with modelled SST at $\theta_{0.015m}$ and SEVIRI observations, the magnitude of the maximum diurnal warming (DW) event, and the number of extreme DW events ($\Delta\theta_{0.015m} > 4\,°C$). Values in parentheses are produced from model simulations at identical locations.*

boundary conditions, but when using Dirichlet boundary conditions the wave breaking parameterisation appears to slightly heighten the occurrence of extreme warming events. In the conditions of most interest here (low wind regimes where diurnal warming of SSTs occur), wave breaking is not expected and therefore it was decided against the use of the wave breaking parameterisation. Subsequently the options chosen for model results shown in this thesis use Neumann type flux surface boundary condition for the TKE and dissipation equations and include the use of an internal wave parameterisation but not a wave breaking parameterisation.

It should be noted here that these results were obtained by initialising to FOAM sea temperatures and salinities and by making daily corrections to the mixed layer temperatures based on OSTIA data. These model simulations were forced with prescribed fluxes of LWR, latent and sensible heat, and surface momentum as opposed to dynamically calculating fluxes by using 2 metre air temperatures, dew point temperatures, and 10 metre wind speeds together with the modelled SST. This issue is discussed further in the next section.

6.5.2 Prescribed vs Dynamic Air-Sea Fluxes

The ECMWF predicts 6 hourly integrated forecasts of LWR, latent and sensible heat flux, and surface momentum flux. A mean fixed 6 hourly value is then derived and used to force the mixed layer model. This is described as using prescribed fluxes. Another approach is to use the 6 hourly forecast surface meteorology (air and dew point temperature, air pressure, and u and v wind speeds) together with the SST from GOTM and using the Fairall air-sea flux algorithm calculate the air-sea fluxes of latent and sensible heat and surface momentum (see Section 3.5.8). The LWR is calculated using the Clark formula (see Section 3.4). This method allows feedback between the modelled SST and the fluxes and is referred to as dynamically calculating the fluxes. Choosing the best combination of Neumann surface boundary conditions for the TKE and length scale equations, internal wave mixing parameterisation, but not wave breaking and applying dynamically calculated fluxes instead of using prescribed fluxes gives the following results. The RMS error has increased by $0.01\,^\circ$C to $0.55\,^\circ$C ($0.55\,^\circ$C), but the maximum diurnal warming event is much less at $4.26\,^\circ$C and the number of diurnal warming events greater than $4\,^\circ$C is now only one.

An example, shown in Figures 6.2 and 6.3, demonstrates the differences between forcing the model with prescribed and dynamic fluxes. For the case of forcing the model with prescribed fluxes the diurnal warming estimates on these two days are $4.35\,^\circ$C and $4.97\,^\circ$C; unrealistically large. However, when the model is forced by calculating the air-sea fluxes dynamically the diurnal warming estimates reduce to more respectable values of $1.46\,^\circ$C and $2.33\,^\circ$C respectively. The mean flux values over this period for the prescribed and dynamic cases are given in Table 6.3. The magnitude of the dynamic fluxes are larger thus leading to the lower SST values seen in Figure 6.2. In Figure 6.3 the SST feedback on the dynamic fluxes can clearly be picked out. As SSTs rise during the early afternoon an increase in the magnitude of each of the three heat flux components is distinctly seen in the dynamically calculated case. This is true on both days, but is particularly pronounced on day 2. This increase in the loss of heat from the ocean reduces the build up of heat at the surface and thus limits the diurnal warming of SSTs.
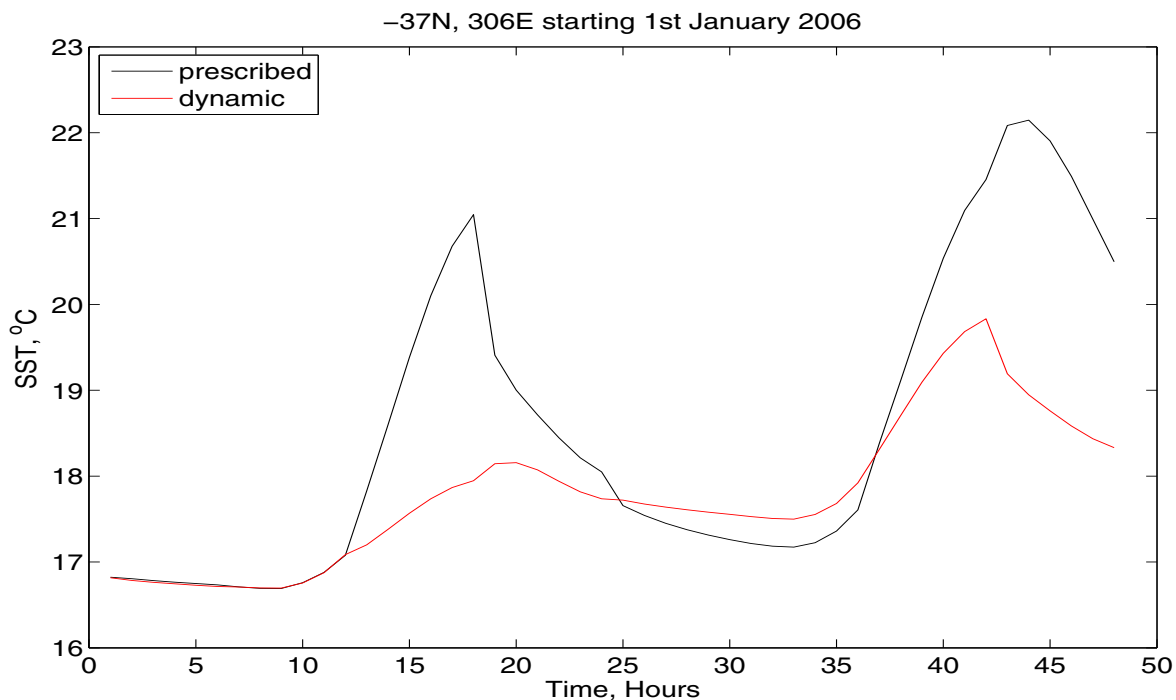
Figure 6.2: *SST at $(-30\,^\circ N, 306\,^\circ E)$ for the 1st–2nd January 2006 forced with prescribed (black) and dynamic (red) fluxes.*

Fluxes	$\overline{Q_E}$	$\overline{Q_H}$	$\overline{Q_B}$	$\overline{Q_E + Q_H + Q_B}$
Prescribed	-25.44	-2.18	-61.77	-84.42
Dynamic	-25.46	-4.75	-71.26	-101.45

Table 6.3: *Mean flux values (prescribed and dynamic) for the 1st–2nd January 2006 at $(-37\,^\circ N, 306\,^\circ E)$. Q_E is the latent heat flux, Q_H the sensible heat flux, and Q_B the long-wave radiation, values are in Wm^{-2}.*

6.5.3 Choice of Radiant Heating Parameterisation

In Section 4.4.2 it was shown that the 9-band ocean radiant heat parameterisation of Paulson and Simpson [101] performed better than their earlier 2-band parameterisation [100]. However, as discussed in Section 3.3, resolving the penetration of solar radiation into a larger number of wave-bands is not the only way to improve the amount of solar absorption at the near surface. Although the 9-band parameterisation covered the full
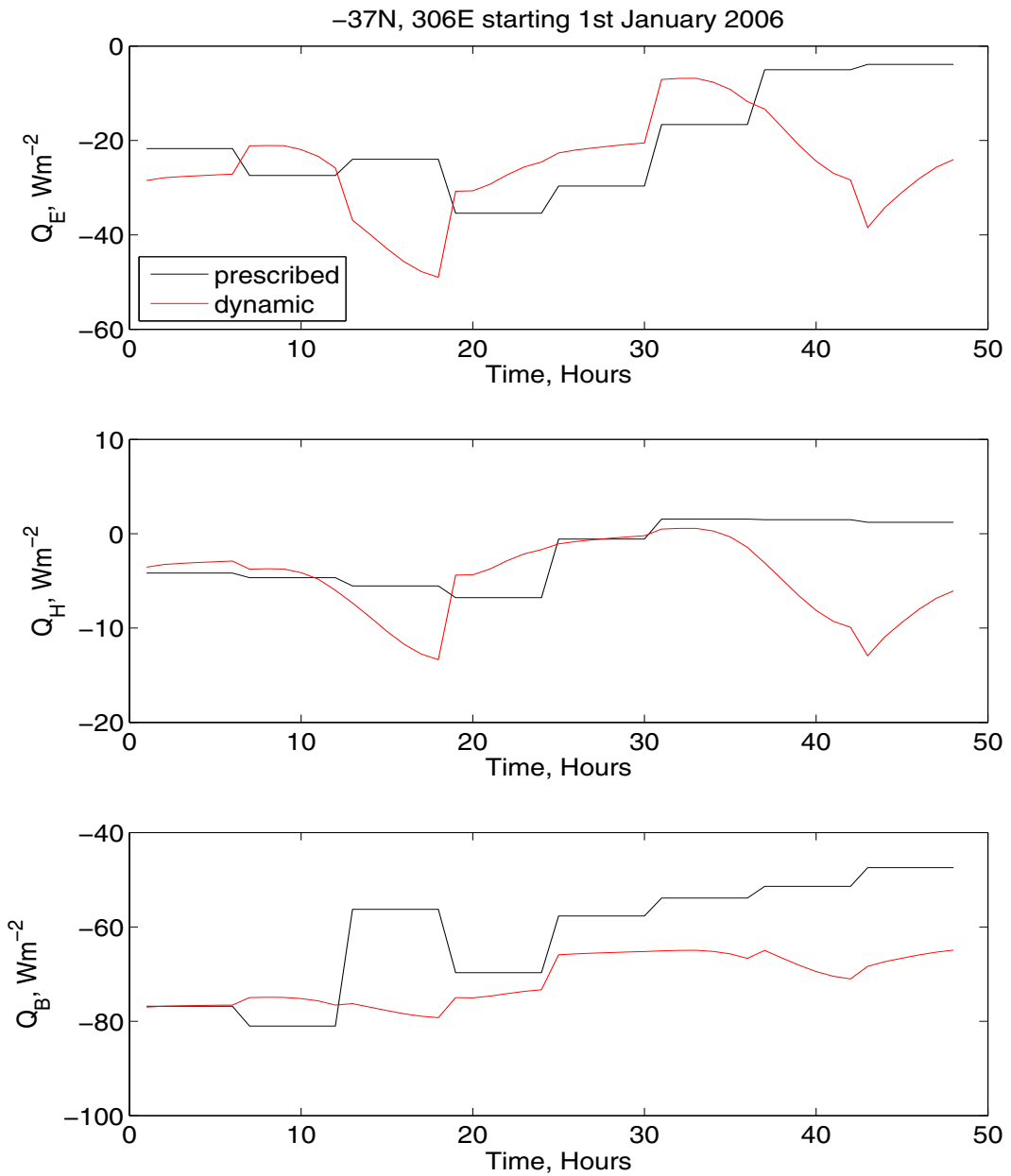
Figure 6.3: *From top: latent heat flux, sensible heat flux, and long-wave radiation at* $(-37\,^\circ N,\ 306\,^\circ E)$ *for the* 1st–2nd *January 2006 comparing 6 hourly prescribed values (black) with dynamically calculated values (red).*

spectral range, the coefficients and exponents in Equation (3.8) are invariant and determined from laboratory experiments using pure water conducted in the early 1900s (see [28]). The ocean, however, is not pure water and contains salt and suspended matter. The coefficients and exponents in the 2-band parameterisation can be modified according to Jerlov water type classification [57], an obsolete index of ocean turbidity. It has been shown that variations in solar transmission are explained almost entirely by upper ocean chlorophyll concentration in the euphotic zone, cloud amount, and solar zenith angle [96]. These factors are the basis of the Ohlmann and Siegel parameterisation [95] which is the only parameterisation to claim to resolve solar transmission variations within the top few metres of the ocean. Global remotely sensed chlorophyll maps replace the crude use of Jerlov water types. It was therefore decided to implement this state-of-the-art parameterisation into GOTM. It should, however, be mentioned that variations in chlorophyll concentration are of little importance for radiant heating within the upper metre because a significant amount of the total energy exists beyond the chlorophyll sensitive wave-bands, as stated in [96].

The 9-band parameterisation is compared to the ocean colour parameterisation of Ohlmann et al. The chlorophyll concentration values used in this thesis are obtained from monthly mean SeaWiFS 9 km chlorophyll-a climatologies which are available at [150]. This data set has only been available since September 1997 and hence was not able to be utilised in the studies at the mooring sites. The RMS errors between SEVIRI observations and the modelled SST, $\theta_{0.015\mathrm{m}}$, using the 9-band parameterisation were $0.57\,°\mathrm{C}$; this is $0.02\,°\mathrm{C}$ greater than when the Ohlmann et al parameterisation was used. The maximum modelled diurnal warming amplitude was $4.83\,°\mathrm{C}$ when using the 9-band parameterisation; this compares with $4.26\,°\mathrm{C}$. The number of extreme warming events ($> 4\,°\mathrm{C}$) was also increased from 1 to 5 when using the 9-band radiation scheme. This suggests that the 9-band radiation parameterisation over estimates the amount of solar absorption at the very near surface. Therefore the ocean radiant heating parameterisation by Ohlmann et al was used for all model simulations in this thesis, excluding at the mooring sites as mentioned earlier.

6.6 Results and Discussion

Having found improvements by using an IW mixing parameterisation, calculating the air-sea fluxes dynamically, and implementing a better ocean radiant heating parameterisation the improved experimental set-up was implemented over the Atlantic Ocean ($-50\,°$N to $50\,°$N and $270\,°$E to $359\,°$E). Modelled diurnal variability ($\Delta\theta_{0.015\text{m}}$) maps were produced for the first week of January 2006 and are shown in Figures 6.4 to 6.10.

Also shown in Figures 6.4 – 6.10 for comparison are graphs of the daily modelled mean SST $\left(\overline{\theta}_{0.015\text{m}}\right)$, the daily modelled mean wind stress $\left(\overline{|\tau|}\right)$, and the daily modelled peak SWR $\left(\overline{I_0}\right)$. There are not too many noticeable changes to the mean SST; however, day to day changes in the diurnal warming can clearly be seen. This particular week is during southern hemisphere summer and several places south of the equator reach a peak SWR of $1000\,\text{Wm}^{-2}$. In the peak SWR graphs (bottom right map in Figures 6.4 – 6.10) it can also be seen, particularly in the southern hemisphere, that areas of high peak SWR, up to $1000\,\text{Wm}^{-2}$, are interspersed with areas of low peak SWR, around $500\,\text{Wm}^{-2}$, this reveals areas affected by cloud cover. The majority of the Atlantic at this time experiences low diurnal warming, between 0 and 1 °C. Some areas, predominately in the southern hemisphere, do experience diurnal warming of above 1 °C. There are also small areas located mainly in the latitude band $-40\,°$N to $-20\,°$N where the diurnal signal becomes large, $2-4\,°$C. Areas of low and extremely low, $< 0.01\,\text{Nm}^{-2}$, wind stress appear to be fairly good indicators of regions of diurnal warming. Strong diurnal warming only occurs when very low wind stresses coincide with very strong SWR.

Stuart-Menteth et al [136] have produced monthly averaged and inter-annual diurnal warming maps derived solely from AVHRR day/night match-up observations. Their study revealed the extent of diurnal warming at mid-latitudes and the tropics and suggested the need for the diurnal cycle to be included in numerical models. A comparison of the diurnal warming graphs (top right map in Figures 6.4 – 6.10) to mean diurnal warming for January 1989 as in Figure 1 of [136] or the graphs in Figure 4 of [136] showing the number of occurrences of warming above 0.5 °C in January

Figure 6.4: *A map of the Atlantic Ocean showing daily mean SST $\left(\overline{\theta}_{0.015m}\right)$, diurnal warming $(\Delta\theta_{0.015m})$, daily mean wind stress $\left(\overline{|\tau|}\right)$, and daily peak SWR $\left(\overline{I_0}\right)$ for the 1st January 2006.*

Figure 6.5: *A map of the Atlantic Ocean showing daily mean SST* $\left(\overline{\theta}_{0.015m}\right)$*, diurnal warming* $(\Delta\theta_{0.015m})$*, daily mean wind stress* $\left(\overline{|\boldsymbol{\tau}|}\right)$*, and daily peak SWR* $\left(\overline{I_0}\right)$ *for the* 2nd *January 2006.*

Figure 6.6: *A map of the Atlantic Ocean showing daily mean SST* $\left(\overline{\theta}_{0.015m}\right)$, *diurnal warming* $(\Delta\theta_{0.015m})$, *daily mean wind stress* $\left(\overline{|\boldsymbol{\tau}|}\right)$, *and daily peak SWR* $\left(\overline{I_0}\right)$ *for the* 3rd *January 2006.*

Figure 6.7: *A map of the Atlantic Ocean showing daily mean SST* $\left(\overline{\theta}_{0.015m}\right)$, *diurnal warming* $(\Delta\theta_{0.015m})$, *daily mean wind stress* $\left(\overline{|\boldsymbol{\tau}|}\right)$, *and daily peak SWR* $\left(\overline{I_0}\right)$ *for the* 4th *January 2006.*

Figure 6.8: *A map of the Atlantic Ocean showing daily mean SST* $\left(\overline{\theta}_{0.015m}\right)$*, diurnal warming* $\left(\Delta\theta_{0.015m}\right)$*, daily mean wind stress* $\left(\overline{|\tau|}\right)$*, and daily peak SWR* $\left(\overline{I_0}\right)$ *for the* 5th *January 2006.*

Figure 6.9: *A map of the Atlantic Ocean showing daily mean SST* $\left(\overline{\theta}_{0.015m}\right)$, *diurnal warming* $(\Delta\theta_{0.015m})$, *daily mean wind stress* $\left(\overline{|\boldsymbol{\tau}|}\right)$, *and daily peak SWR* $\left(\overline{I_0}\right)$ *for the* 6th *January 2006.*
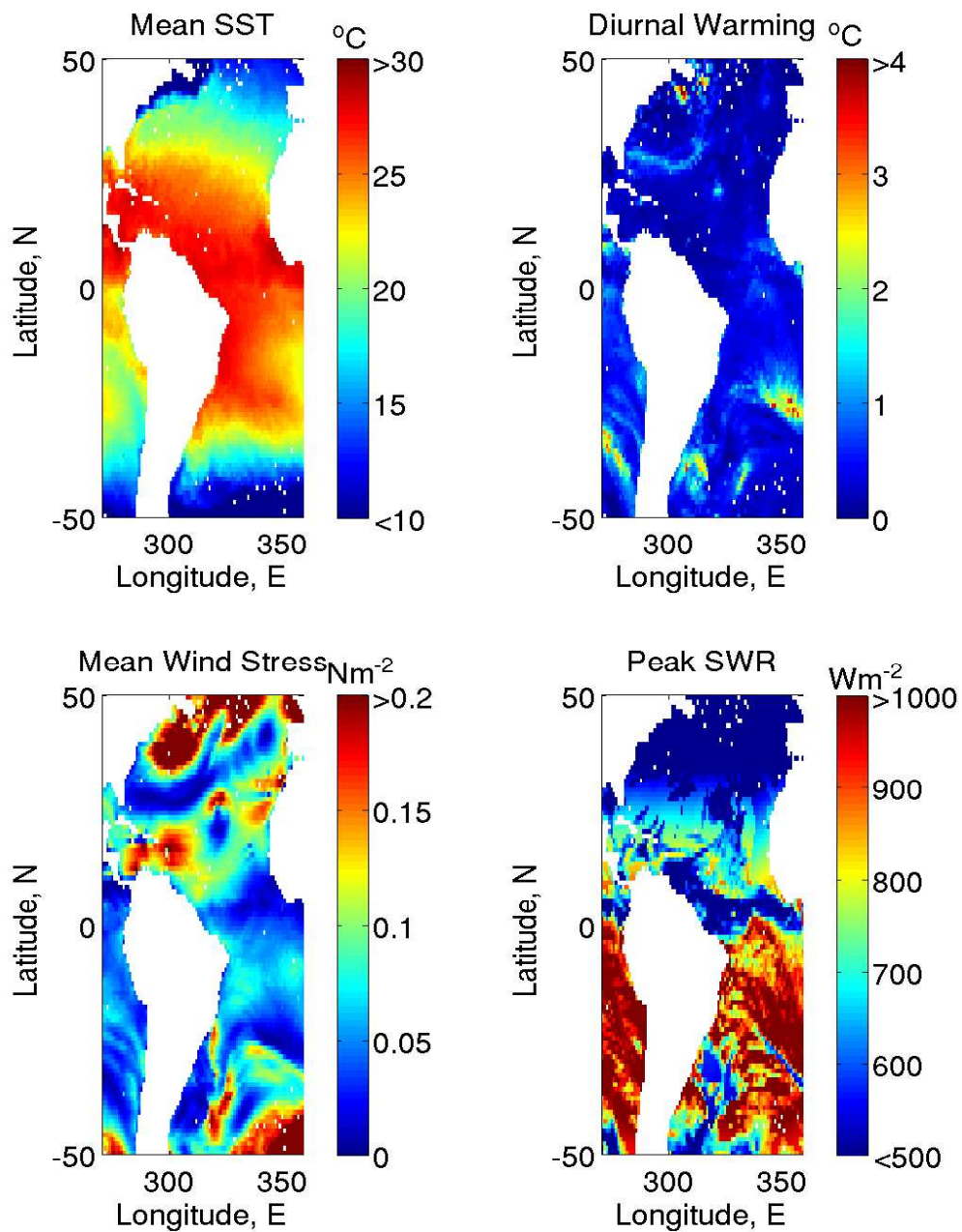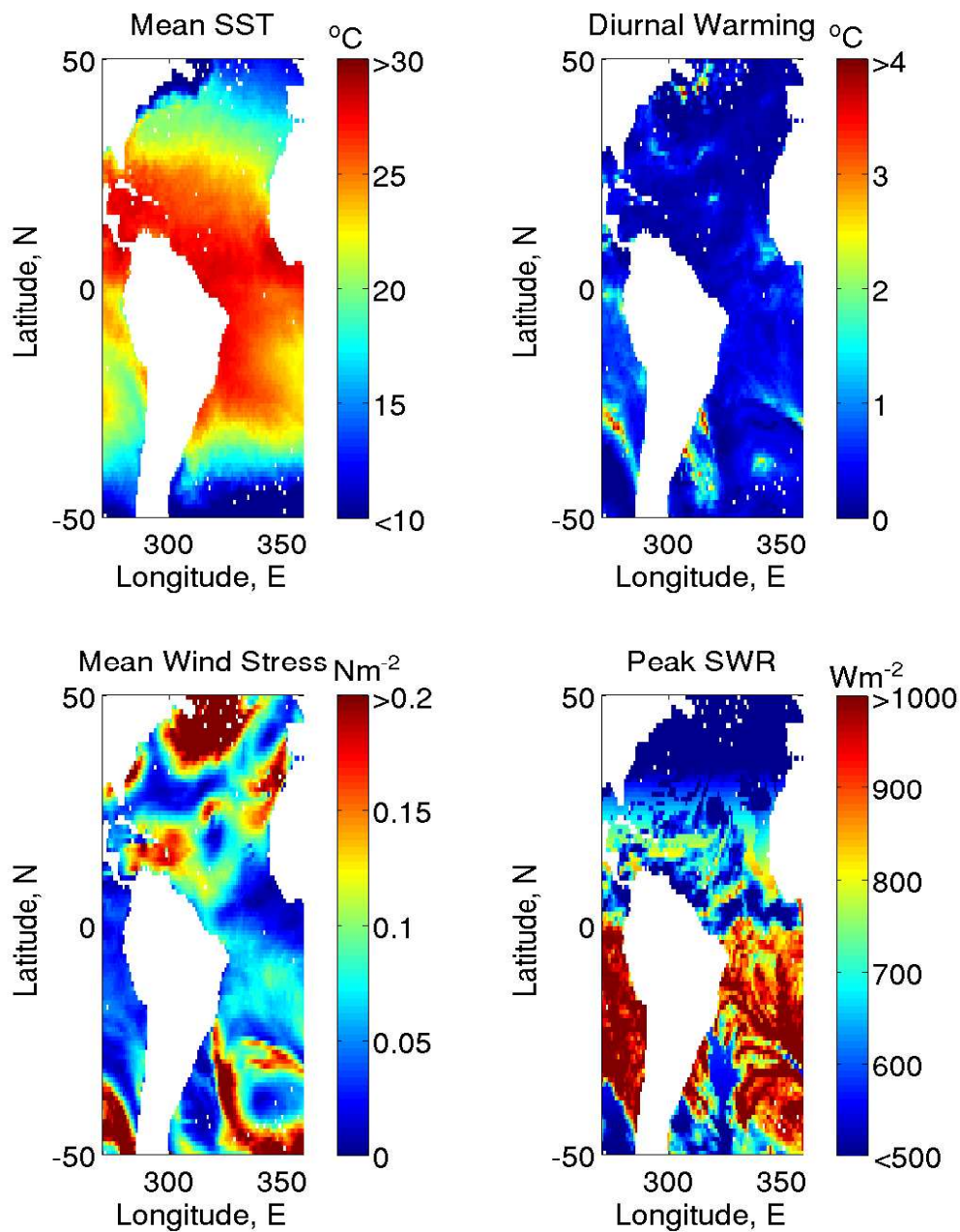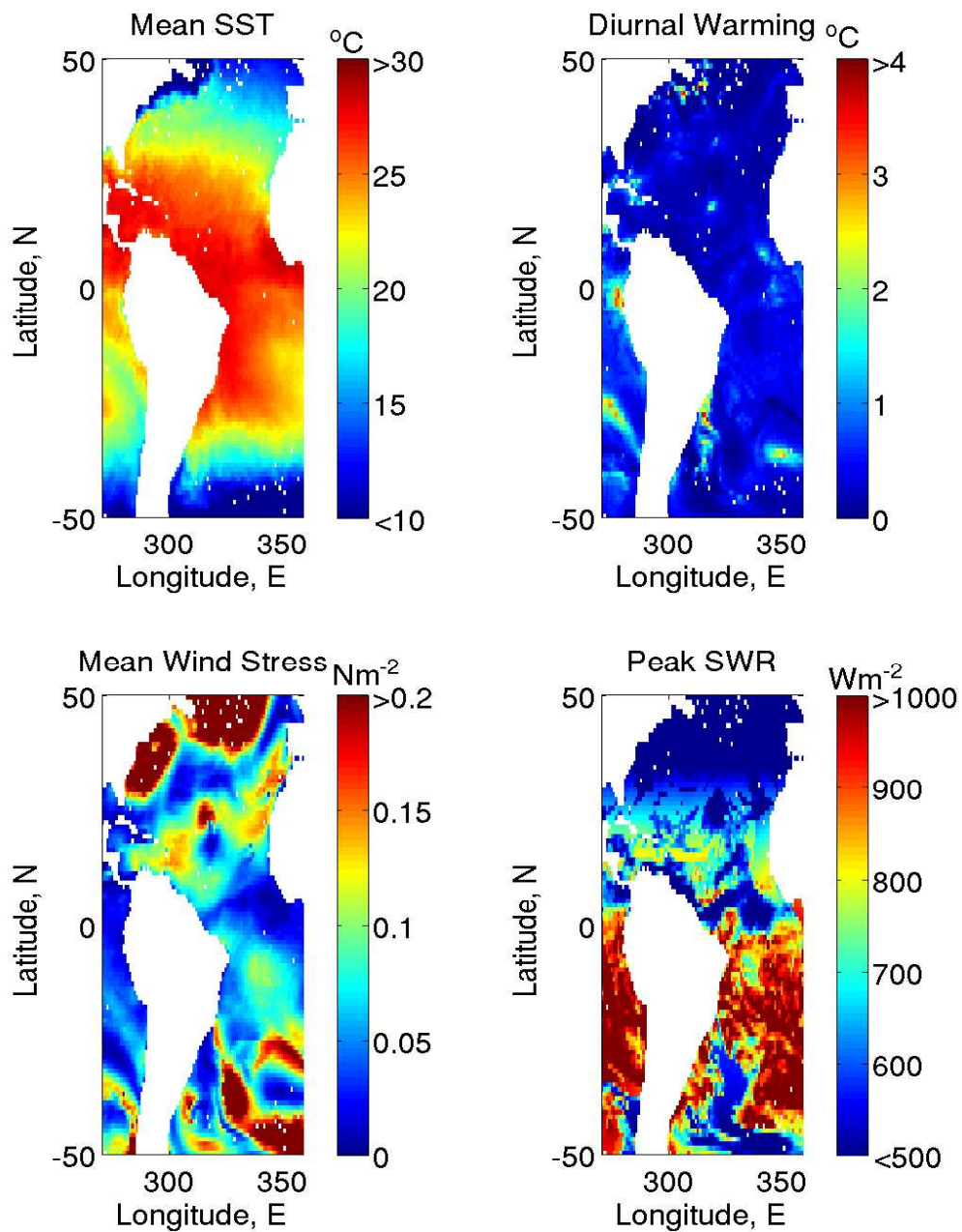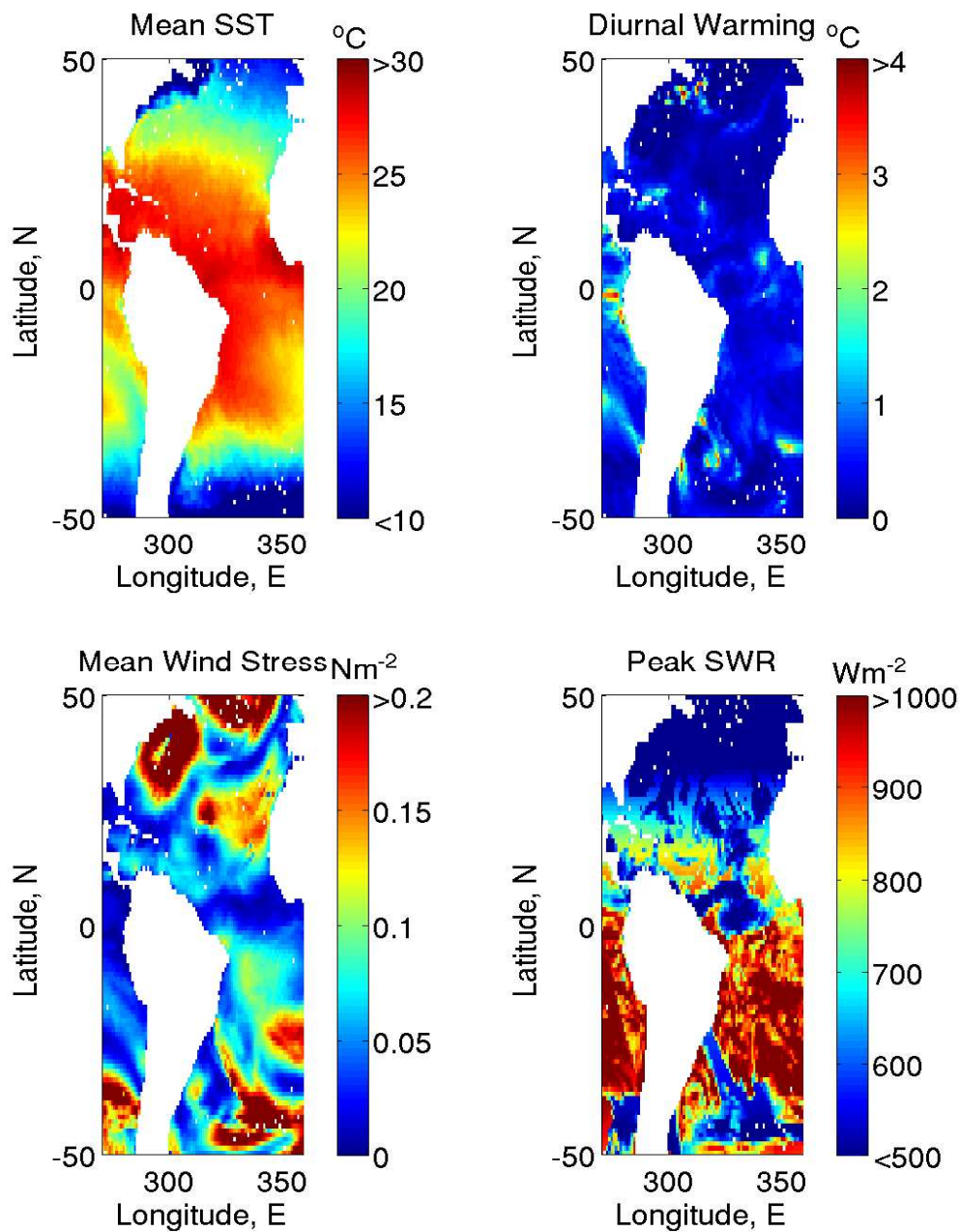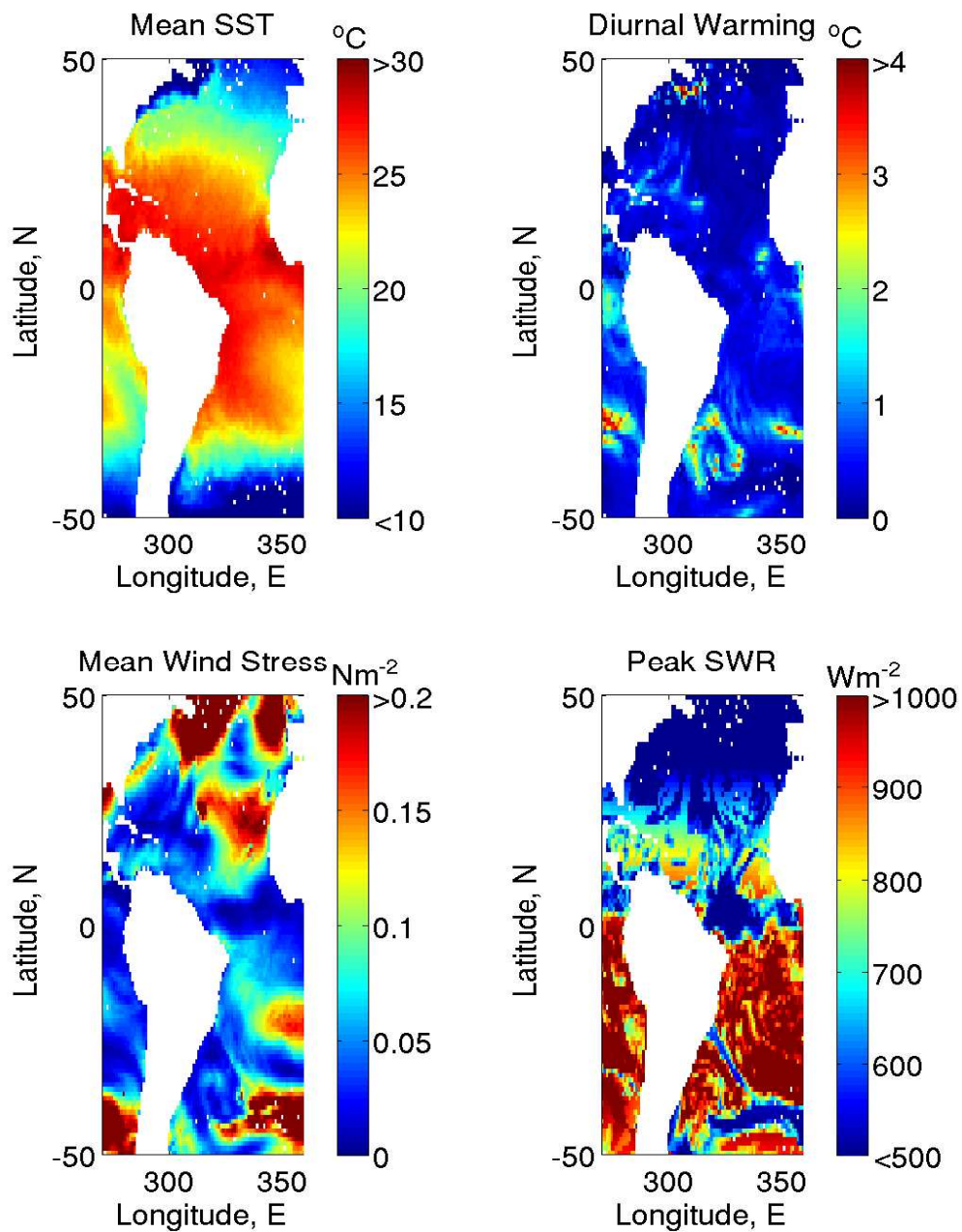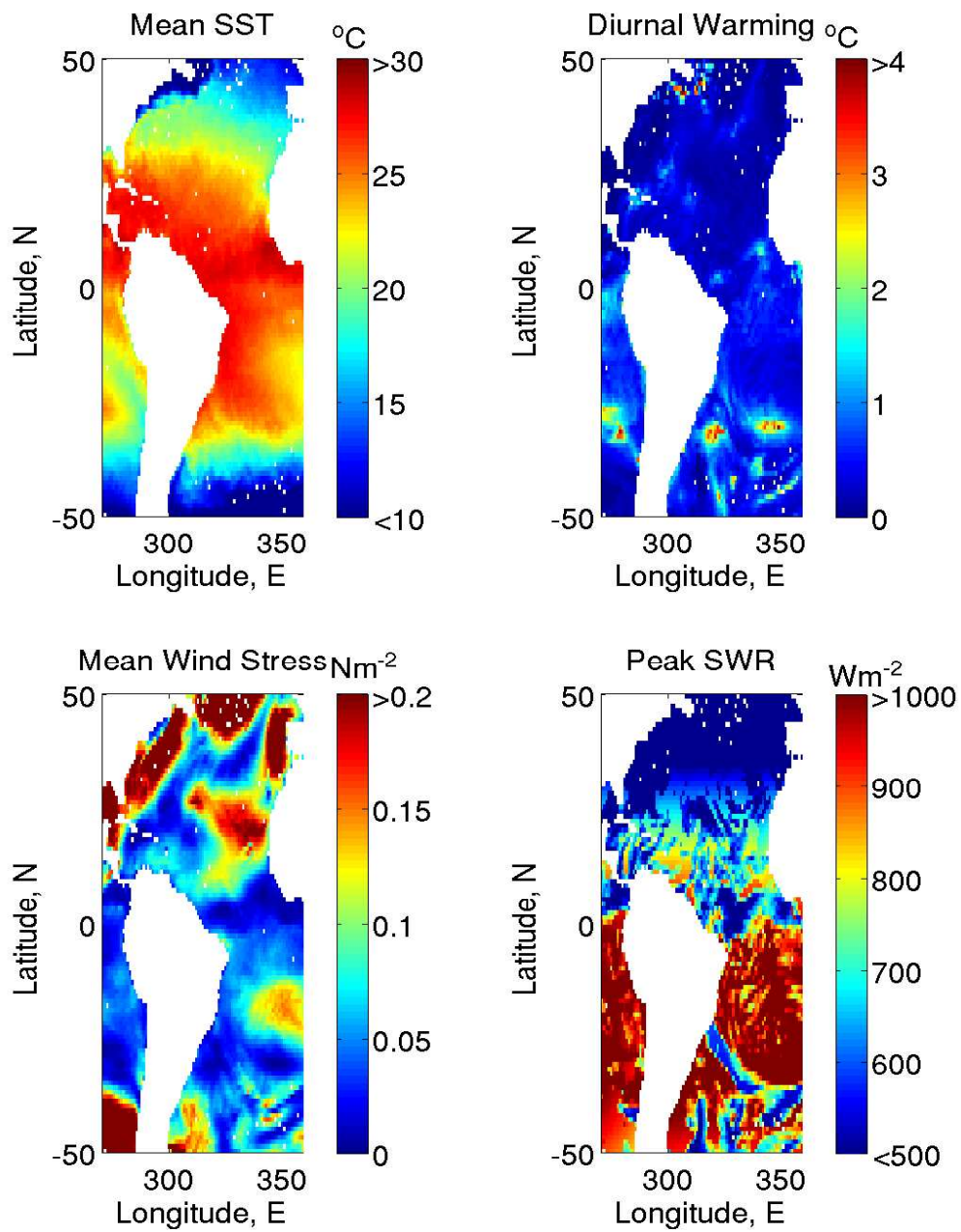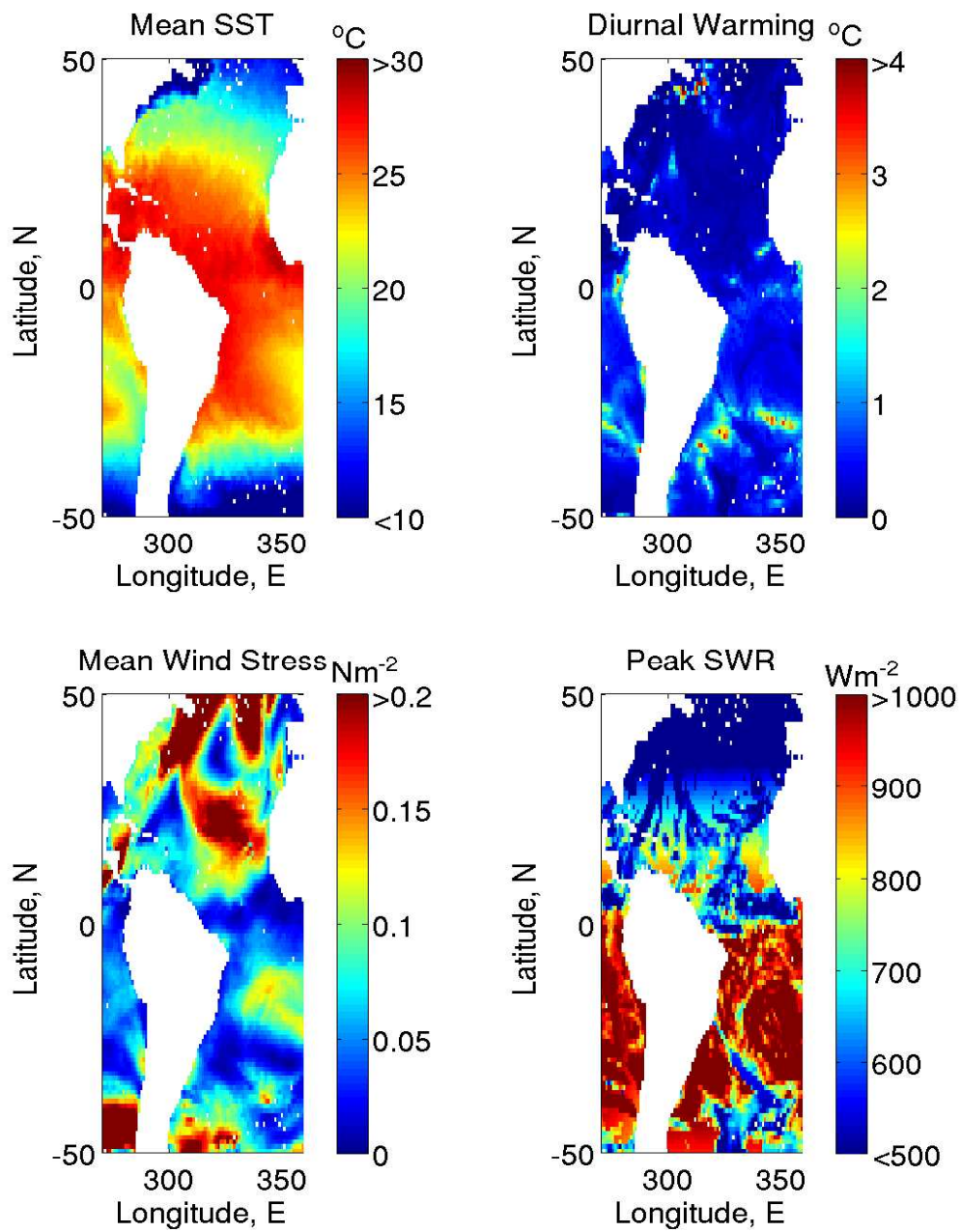
Figure 6.10: *A map of the Atlantic Ocean showing daily mean SST $\left(\overline{\theta}_{0.015m}\right)$, diurnal warming $(\Delta\theta_{0.015m})$, daily mean wind stress $\left(\overline{|\tau|}\right)$, and daily peak SWR $\left(\overline{I_0}\right)$ for the 7th January 2006.*

over 6 particular years does show some similarities - particularly the susceptibility of the latitude band $-40\,°$N to $-20\,°$N to strong diurnal warming. As far as is known plots such as Figures 6.4 – 6.10 are a first attempt to produce such maps based on model output and are of added value in several respects. Firstly they can be produced globally complete on a daily basis, as they do not rely on particular overpass paths and times or the availability of day/night overlaps in the observations. Secondly many climate and ocean modellers are reluctant to include a diurnal cycle in their models because of the increased cost of extra vertical resolution; therefore the satellite community are required to provide observations for assimilation that are not 'corrupted' by a diurnal signal. These maps can be used to highlight areas where observations are likely to have a diurnal warming signal and flag observations in the vicinity; or better still use the model output to remove the diurnal bias at any location. Thirdly this simple model approach could potentially be useful for improving accuracy in observational foundation SST products by again removing the diurnal signal and reducing bias. It follows from the previous two points that what is actually required is not necessarily a diurnal warming value but the skin to bulk measure at an observation time. For example, a satellite measures the temperature at the skin or sub-skin depth and a quantification of the near surface variability is needed to convert this measurement to the foundation depth for inclusion in a bulk SST product, or at the $5\,\mathrm{m}$ depth for assimilation into an ocean model. The new approach presented here can provide these much needed estimates.

To assess the accuracy of the modelled diurnal warming estimates GHRSST L2P observations from SEVIRI, AMSRE, and TMI are compared to hourly model output. The results presented in Table 6.4 show that overall the model–observation differences have zero mean and a root mean square of $0.58\,°$C. A negative bias, warmer observations than model, are seen for the SEVIRI observations and positive biases for AMSRE and TMI observations. This could represent an inherent warm bias in SEVIRI SST when compared to AMSRE and TMI measured SST. The SEVIRI observations are compared to the parameterised cool skin temperature of the model. A persistently over estimated cool skin effect could be contributing to the larger SEVIRI offset. The

table also shows that although the mean SEVIRI errors are larger than the other observation types the RMS errors are smaller, as are the standard deviations. Thus indicating a much smaller random component to the SEVIRI observation errors. The overall model–observation differences are shown to be the same for daytime and night time match-ups and the RMS and STD are similar, varying by only 0.02 °C. Daytime here is defined as occurring between the hours 10–16 (local time) and night time hours between 22–04 (local time).

Match-up	Number	Mean	RMS	STD
GOTM-SEVIRI	28075	−0.24	0.43	0.26
Day: GOTM-SEVIRI	7610	−0.26	0.42	0.21
Night: GOTM-SEVIRI	6264	−0.24	0.44	0.26
GOTM-AMSRE	26884	0.13	0.62	0.59
Day: GOTM-AMSRE	6009	0.14	0.55	0.51
Night: GOTM-AMSRE	5660	0.19	0.61	0.55
GOTM-TMI	22269	0.16	0.68	0.64
Day: GOTM-TMI	6103	0.15	0.67	0.64
Night: GOTM-TMI	4647	0.07	0.67	0.66
GOTM-ALL	77228	0.00	0.58	0.58
Day: GOTM-ALL	19722	−0.01	0.55	0.55
Night: GOTM-ALL	16571	−0.01	0.57	0.57

Table 6.4: *Comparing model output (θ_{skin} for SEVIRI and $\theta_{0.015m}$ for AMSRE and TMI) to GHRSST L2P satellite data. Results show number of match-ups, mean, root mean square difference, and standard deviation; values in* °C.

The satellite observations are also compared to the OSTIA product in Table 6.5. The differences in Table 6.5 are generally slightly smaller than Table 6.4. This is perhaps not surprising since OSTIA is a mean of the GHRSST satellite observations anyway. The satellite observations all have a negative bias (except daytime AMSRE and daytime TMI), showing that the satellite observations are slightly warmer than

OSTIA on average. This should be expected as OSTIA represents a night time or foundation temperature, whereas the match-ups here compare all observations, including those that contain a diurnal signal. It is odd, however, that the daytime AMSRE and TMI observations show a positive bias (OSTIA warmer than observations). It would be expected that the daytime observations on average would be warmer than the OSTIA, which represents the night time temperature. There is also particularly large errors associated with the night time TMI observations which should be a concern. The SEVIRI observations again show a larger bias than the other observations suggesting an inherent warm bias in SEVIRI SST.

Match-up	Number	Mean	RMS	STD
OSTIA-SEVIRI	28447	−0.14	0.36	0.31
Day: OSTIA-SEVIRI	7693	−0.14	0.33	0.27
Night: OSTIA-SEVIRI	6376	−0.12	0.36	0.32
OSTIA-AMSRE	27364	−0.03	0.55	0.55
Day: OSTIA-AMSRE	6068	0.06	0.49	0.48
Night: OSTIA-AMSRE	5803	−0.03	0.60	0.60
OSTIA-TMI	23750	−0.01	0.65	0.65
Day: OSTIA-TMI	6137	0.05	0.60	0.60
Night: OSTIA-TMI	5382	−0.20	0.78	0.72
OSTIA-ALL	79561	−0.06	0.53	0.52
Day: OSTIA-ALL	19898	−0.02	0.48	0.48
Night: OSTIA-ALL	17561	−0.11	0.59	0.57

Table 6.5: *Comparing OSTIA, used as the initial condition for the Atlantic model runs, to GHRSST L2P satellite data. Results show number of match-ups, mean, root mean square difference, and standard deviation; values in °C.*

6.7 Summary

In this chapter it has been shown how global operational forecasting data sets can be used to initialise and force a 1-D mixed layer ocean model to produce diurnal variability estimates. These models can then be run at many locations in a particular area and spatial maps of the diurnal variability can be produced. It is shown how model performance can be improved by first resolving the SWR at a resolution much finer than 6 hours. In this chapter it was also shown how important the choice of additional mixing options can be. It was found that the most stable choice was using internal wave mixing, but not wave breaking and to use Neumann type surface boundary conditions for the TKE and length scale equations. Calculating the air-sea fluxes using the forecast surface meteorology and modelled SSTs was also found to produce improvements on using the 6 hourly fixed ECMWF surface fluxes. This is because the feedback between the modelled SST and the air-sea fluxes prevents extreme diurnal warming and keeps a balance. Finally the 9-band ocean radiant heating parameterisation was upgraded to the state-of-the-art parameterisation that uses remotely sensed chlorophyll data to better represent the absorption of solar radiation in the upper ocean. This type of 'optimal' set-up was shown to produce fairly accurate results when compared to SEVIRI satellite derived SST observations. The method was then applied over the Atlantic Ocean to produce daily modelled diurnal variability SST maps. These types of maps are potentially very useful in highlighting areas susceptible to diurnal warming and then producing information for flagging daytime satellite observations, or better still removing the warming signal in those areas. The modelled SST estimates were shown to have zero mean and 0.58 °C RMS errors when compared to SEVIRI, AMSRE, and TMI observations. Detailed knowledge of the extent of diurnal warming in the world's oceans is still limited and this system could be employed at various locations and in different seasons to improve our understanding of the conditions required for diurnal variability and to build a climatology of its global distribution. This system could be used in real time to forecast likely diurnal warming signals and thus could be used as part of a data assimilation system that assimilates SST observations in real

time.

In the next chapter a method is developed by which the modelled diurnal warming estimates are improved by the assimilation of satellite observations of SST. In combining model output with observations over the diurnal cycle uncertainties in the original modelled output are reduced.

Chapter 7

Assimilating Satellite SST Observations into the Diurnal Cycle

7.1   Introduction

The work in Chapter 6 demonstrated how operational forecast data can be used to force a collection of mixed layer models in order to estimate diurnal variability. The output from these model simulations can be used to evaluate diurnal warming patterns in time and over a wide area, as seen in Figures 6.4 – 6.10. In the introduction to Chapter 5 it was described how data assimilation is used to merge dynamical model output with observations to improve state estimation. In this chapter work is presented that shows how the modelled diurnal warming estimates, as produced in Chapter 6, can be improved by incorporating satellite derived observations of the SST over the day. A technique to assimilate individual SST observations into the mixed layer was described in Section 5.4.2. This adjustment to mixed layer temperatures at night time was shown to improve SST estimates at the buoy sites, and was used in Chapter 6 to initialise the model by adjusting the mixed layer FOAM temperatures according to OSTIA observations. However, as was discussed in Chapter 5 this assimilation method was not able to improve diurnal warming estimates. It was outlined how observations would be needed throughout the day in order to improve the modelled diurnal signal. Forcing in the model could then be made better, for example by the choice of fractional

cloud cover. In this chapter GHRSST L2P satellite derived SST observations occurring throughout the day are used to improve model estimates of the diurnal signal. A new and novel assimilation scheme is developed that exploits diurnal information in the observations to better quantify the diurnal cycle of SSTs. This is achieved by making corrections (within uncertainty limits) to the forcing data.

This chapter proceeds as follows: Firstly, an outline of the current research problem of preparing SST observations for assimilation by accounting for diurnal variability in the satellite measurements is presented. Following this the SST data assimilation method that has been developed for this problem is outlined and details of the steps involved are given. This algorithm is then employed at locations in the Atlantic Ocean. Variations and improvements to the algorithm are discussed. The results obtained from using this scheme are presented and conclusions drawn.

7.2 Preparing Satellite SSTs Observations for Assimilation

Satellites measure SST either in the infrared (IR) or the microwave (MW) part of the electromagnetic spectrum. IR instruments derive a skin temperature and MW instruments the sub-skin temperature. In Chapter 1 it was described how these near surface observations can be susceptible to diurnal warming signals. Therefore the timing of the observations and the conditions in which the measurements are taken is very important. However, current ocean models are not able to resolve the near surface thermal micro-structure or adequately represent features of diurnal variability and therefore the assimilation of daytime SST observations presents difficulties.

In the assimilation process the innovation vector $Hx - y$ uses an observation operator H to transform model variables x onto an observed quantity y, so that a like-for-like comparison can be made. The sea temperature at the minimum modelled depth, typically $5\,\mathrm{m}$ or deeper in an ocean model, needs to be transformed in space and time to give a temperature at the near surface, as measured by the satellite. What is therefore needed for the satellite SST assimilation problem is an operator that can effectively

provide the diurnal warming estimate at the observation time. This observation operator can not be invariant as the transformation will depend on the particular local conditions at a given time. Developing such an operator is not an easy task; several attempts at parameterising the likely warming (e.g. [151], [68], [42], and [137]) have experienced difficulties in representing the full range of outcomes in this highly complex and non-linear system. A prognostic skin SST scheme has been tried with the ECMWF atmospheric model [158]; however, its effect on weather forecasting and four-dimensional data assimilation have yet to be fully examined. In Chapters 4 and 6 of this thesis results are presented which show some degree of success in modelling the diurnal variability. The use of GOTM in this way can be viewed as providing a dynamic observation operator H, because by modelling the diurnal cycle and providing good near surface resolution we are able to quantify the transform from foundation temperature to skin or sub-skin temperature. However the modelled diurnal variability is not without error. This error could be reduced by assimilating the observations into the diurnal cycle at the correct time and near surface depth. How this should best be done is an interesting problem in itself.

The extent of diurnal warming is predominately dependent on two key factors: sea surface wind speeds and the strength of the insolation, whose variance at a given location and time is largely determined by the cloud cover. As explained in Section 1.5 strong insolation during daytime, under clear skies, causes a warm stable stratified layer to appear, but this near surface warming can easily be broken down in the presence of wind driven mixing. The uncertainties in these forcing variables (cloud cover and wind speed) thus contribute to the uncertainty in the modelled diurnal warming estimates. Unfortunately in NWP there is not a single, simple law which governs the formation of cloud and thus it is very difficult to parameterise and is a major source of uncertainty in model predictions. For example, Groisman et al [49] explicitly highlights cloud cover 'as one of the major trouble spots' of cloud parameterisation. Assumptions with respect to distributions of cloud cover throughout the atmosphere can significantly affect the energy budget [56]. Wind speeds are also very difficult to assess in weather forecasting, particularly at low ($< 3\,\mathrm{ms}^{-1}$) and high ($> 20\,\mathrm{ms}^{-1}$) values where obser-

114

vational comparisons are difficult and errors vary for different regions and time scales
[17]. In diurnal cycle modelling the high values are not of concern as no diurnal signal
forms at high wind speeds; however, the diurnal warming is very sensitive to slight
changes in wind speeds at the low values. The wind speed, w, is important because
wind stress increases roughly as $w^{2.7}$ and mixed layer deepening with w^4 [97]. There-
fore even slight biases in NWP sea surface wind speeds can lead to systematic errors in
ocean circulation models that are forced by these winds [17]. Wind speeds of less than
$5\,\mathrm{ms}^{-1}$ account for nearly 40% of global hourly averaged winds [125]. Weak winds are
concentrated in the tropics and sub-tropics where the majority of ocean to atmosphere
heat flux occurs and shifts in their patterns affect the global heat flux balance [125].

SST observations over the day can provide additional information as to the correct-
ness of the modelled estimate of the warming. To bring the model projection closer
to the observations the forcing data over the time period will need to be adjusted. As
explained above the magnitude of diurnal warming is primarily a response to the wind
speeds and the cloud cover. The method developed here therefore judiciously seeks
to adjust the wind speeds and cloud forcing, within feasible error bounds, in order to
better fit the modelled SST to the observations recorded over the day. The modelled
SST at observation depth, $\theta_{z^{\mathrm{obs}}}$, can be described as a non linear function of cloud
cover, n, and wind speed, w,

$$\theta_{z^{\mathrm{obs}}} = \theta_{z^{\mathrm{obs}}}\left(n, w\right).$$ (7.1)

The problem can then be stated as finding values of n and w such that

$$\left|\theta_{z^{\mathrm{obs}}} - \theta^{\mathrm{obs}}\right|$$ (7.2)

is minimised. In other words to find optimal values of n and w that will bring the
modelled SST trajectory as close to the SST observations as possible.

7.3   The Data Assimilation Method

This section describes an assimilation algorithm for finding a solution to the above
outlined problem.

7.3.1 Overview

A forcing parameter pair (ϵ_A, ϵ_B) associated with adjustments to the wind speed, w, and cloud cover, n, is introduced and its value tuned over each 24 hour window. Five model realisations are required over the time window. To start with, the parameters are set at zero and the wind speeds and cloud cover values are derived from ECMWF 6 hourly forecasts. A further model run is performed in which ϵ_B is perturbed. The results of these simulations are used to calculate local gradient information. This gradient information is then used to find an 'optimal' ϵ_B parameter that will minimise the model-observation SST differences over the time window. With the first 'optimal' parameter found, two further model runs are performed in order to determine the sensitivity to the parameter ϵ_A, and its 'optimal' value determined. The final model simulation uses the two 'optimal' parameters. The 'best' model run is then chosen as the analysis for that 24 hour period.

7.3.2 The Algorithm

The modelled SST at the top grid level, θ_{150}, can be viewed as a function of fractional cloud cover, n, and the wind speed forcing, $w = \sqrt{u^2 + v^2}$,

$$\theta_{150} = \theta_{150}(n, w). \tag{7.3}$$

Parameters ϵ_A and ϵ_B are introduced

$$n = n_{obs} + \epsilon_A, \tag{7.4}$$

$$
\begin{aligned}
w &= (1 + \epsilon_B)w_{obs}, \tag{7.5}\\
&= (1 + \epsilon_B)\sqrt{u_{obs}^2 + v_{obs}^2}. \tag{7.6}
\end{aligned}
$$

These parameters remain fixed over each 24 hour time window, although the observed forcing data: n_{obs}, u_{obs}, and v_{obs} change every 6 hours. Note that the cloud correction uses absolute errors, whereas the wind correction uses relative errors. This is because an absolute correction to w is not possible because the correction is performed on the components u_{obs}, v_{obs}. Also a relative error correction to the cloud field is not desirable

because of the strong cloud limits, see Equations (7.10) and (7.11). The SST can now be viewed as a function of the parameters

$$\theta_{150} = \theta_{150}\left(\epsilon_A, \epsilon_B\right). \tag{7.7}$$

The observed forcing data, n_{obs}, is obtained by using the 6 hourly integrated ECMWF forecast SWR in Equation (6.2), and the u_{obs} and v_{obs} are the 6 hourly mean 10 m wind speed components from the ECMWF forecasts. The model is initialised to FOAM sea temperature and salinity profiles at the start of each 24 hour time window. In addition daily OSTIA values are assimilated into the near surface, by adjusting the FOAM mixed layer temperatures using the method described in Section 5.4.2.

We now define a cost function $J = J\left(\epsilon_A, \epsilon_B\right)$ as

$$J = \sum_{i=1}^{N} \left(\theta_i^{\text{model}} - \theta_i^{\text{obs}}\right), \tag{7.8}$$

where N is the number of observations over the 24 hour window. If $J_0 = J(0,0) < 0$ then on average the SST observations are higher than the model and therefore, to increase the size of the diurnal cycle, cloud cover and wind speeds need to be reduced (ϵ_A, $\epsilon_B < 0$). On the other hand if $J_0 > 0$ then the modelled SST is generally greater than the observations and the diurnal cycle needs to be reduced and this can be achieved by increasing cloud cover and wind speeds (ϵ_A, $\epsilon_B > 0$).

The data assimilation problem can now be stated as follows.
An 'optimal' parameter pair $(\epsilon_A^*, \epsilon_B^*)$ is sought such that for all feasible (ϵ_A, ϵ_B)

$$|J(\epsilon_A^*, \epsilon_B^*)| \leq |J(\epsilon_A, \epsilon_B)|. \tag{7.9}$$

It is possible that an increase in cloud cover and a decrease in wind speeds and vice versa could provide the desired effect. In this scenario the effects of changes in wind speed and cloud cover on the SST would to some extent cancel each other out. Because the whole parameter space is not sampled and additional information, such as independent observations of cloud or wind, are not used, these possibilities are excluded in the interests of simplicity. The feasible parameter range is therefore defined in two

quadrants:

$$0 < \epsilon_A \leq 1,$$
$$0 < \epsilon_B < 3, \tag{7.10}$$

if $J_0 > 0$ and

$$-1 \leq \epsilon_A < 0,$$
$$-1 < \epsilon_B < 0, \tag{7.11}$$

if $J_0 < 0$. In the trivial case where $J_0 = 0$ the optimal parameters are $(0,0)$. The choice of parameter range is (where possible) based on physical assumptions. The range for ϵ_A is therefore the maximum and minimum possible change to n_{obs}. Because four different n_{obs} values are given over a 24 hour period a check is made on each to ensure that n lies within one and zero, i.e. can not take the cloud cover value beyond total cloud cover and below the clear sky value. The parameter ϵ_B is not permitted to change the wind direction, only the magnitude. The upper bound on ϵ_B is more uncertain, the value of 3 was initially chosen, which allows a 300% increase in the wind speeds. When considering the very low wind speed values associated with strong diurnal warming this upper limit is plausible. It was assumed that for high wind speeds a perturbed increase will not produce much change in SST on diurnal time scales and therefore the sensitivity will be too small to make a correction within the limits, thus no correction is made. This therefore provides a natural upper bound on unwanted changes in large wind speeds.

The solution procedure used for solving problem (7.9) is outlined below.

STEP 1

Run the model forward over the time window $t \in [0, T]$, where $T = 24$ hours, with $(\epsilon_A, \epsilon_B) = (0, 0)$ and evaluate $J_0 = J(0, 0)$ over the period.

STEP 2

Restart at $t = 0$ and run the model over the time window again, this time the wind parameter, ϵ_B, is perturbed

$$(\epsilon_A, \epsilon_B) = (0, \epsilon_{B_1}), \tag{7.12}$$

where

$$\epsilon_{B_1} = \begin{cases} 0.25 & \text{if } J_0 > 0 \\ -0.25 & \text{otherwise} \end{cases} \tag{7.13}$$

representing a 25% change in the wind speed forcing. The cost function $J(0, \epsilon_{B_1})$ is evaluated over the period. Then estimate the sensitivity or local gradient of J_0 with respect to ϵ_B,

$$\frac{\partial J_0}{\partial \epsilon_B} \approx \frac{J(0, \epsilon_{B_1}) - J_0}{\epsilon_{B_1}}. \tag{7.14}$$

STEP 3

Assuming the cost function $J(0, \epsilon_B)$ varies linearly within the feasible ϵ_B parameter range (Equation (7.10) or (7.11)) we are able to construct the line

$$J(0, \epsilon_B) = \frac{\partial J_0}{\partial \epsilon_B} \epsilon_B + J_0 \tag{7.15}$$

and determine an 'optimal' value

$$\epsilon_B^* = \left(\frac{\partial J_0}{\partial \epsilon_B} \right)^{-1} \left(\min_{\text{feasible } \epsilon_B} |J(0, \epsilon_B)| - J_0 \right). \tag{7.16}$$

The aim is to choose $J(0, \epsilon_B)$ as small as possible without taking the line, Equation (7.15), outside the feasible limits set in Equation (7.10) or (7.11). This is calculated through an iterative process:

$$\epsilon_B^k = \left(\frac{\partial J_0}{\partial \epsilon_B} \right)^{-1} \left(J(0, \epsilon_B)^k - J_0 \right), \tag{7.17}$$

where $k = 1, \ldots,$ end are the iterates. If $J_0 > 0$ then

$$J(0, \epsilon_B)^k = J_0 - \alpha k \tag{7.18}$$

and if $J_0 < 0$ then

$$J(0, \epsilon_B)^k = J_0 + \alpha k, \tag{7.19}$$

where the step size for J, α, is chosen as $0.05\,^\circ\text{C}$. This allows $J(0, \epsilon_B)^k$ to be evaluated to within $0.05\,^\circ\text{C}$. At each iteration ϵ_B^k (Equation (7.17)) is determined and a calculation made to ascertain whether this value lies outside the feasible range, Equations (7.10) or (7.11). The iteration loop ends when $J(0, \epsilon_B)$ reaches zero, or alternatively when ϵ_B^k no longer falls within the trust region. At this stage the minimum $|J(0, \epsilon_B)|$ is known and the optimal parameter, ϵ_B^*, is determined using Equation (7.16). An example is shown in Figure 7.1.

$J(0, \epsilon_B)$

$J(0, \epsilon_B) = \frac{\partial J_0}{\partial \epsilon_B}\epsilon_B + J_0$

$\epsilon_B = 3$
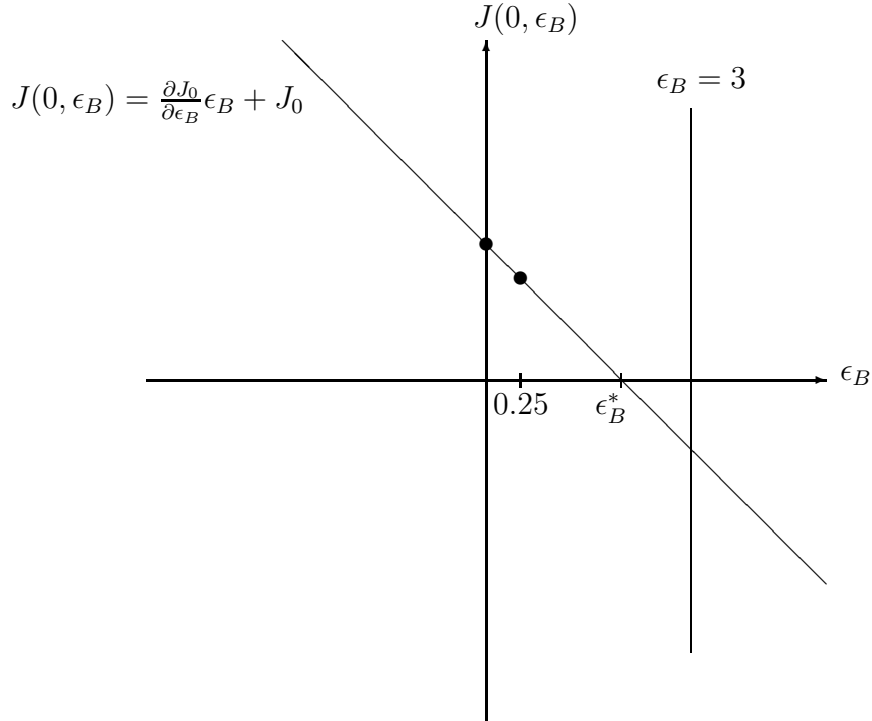
ϵ_B

0.25 $\quad \epsilon_B^*$

Figure 7.1: *A sketch showing an example of how the line, Equation (7.15), lies within the feasible limits (in this case $0 < \epsilon_B < 3$) and the 'optimal' parameter ϵ_B^* is determined.*

STEP 4

Two further model runs at performed with $(\epsilon_A, \epsilon_B) = (0, \epsilon_B^*)$ and $(\epsilon_A, \epsilon_B) = (\epsilon_{A_1}, \epsilon_B^*)$ where

$$\epsilon_{A_1} = \begin{cases} 0.1 & \text{if } J_0 > 0 \\ -0.1 & \text{otherwise} \end{cases} \tag{7.20}$$

representing a 1/10 increment in cloud cover. Using the methods of step 2 and 3 a local gradient $\left(\frac{\partial J(0, \epsilon_B^*)}{\partial \epsilon_A}\right)$ is determined and the 'optimal' parameter ϵ_A^* is calculated.

STEP 5

The model is run over the time window for a fifth and final time using the calculated pair $(\epsilon_A^*, \epsilon_B^*)$ and the cost function evaluated. The best model run (that which produced the smallest cost function value) is then chosen as the final analysis. This is expected to be from the calculated optimal parameters, but as previous model output is temporarily stored a quick and easy comparison is made to the cost function values from previous model runs. This whole process is then repeated for each 24 hour period of interest.

7.3.3 Justification

The assumption in this method is that J varies linearly with respect to the parameters (ϵ_A, ϵ_B) within the feasible limits. The validity of this assumption is very difficult to test thoroughly because of the enormous range of conditions. However, an example of a 'typical' scenario is given in Figure 7.2. In these graphs it is shown that to good approximation J does vary linearly within the feasible parameter limits, given by Equations (7.10) and (7.11).
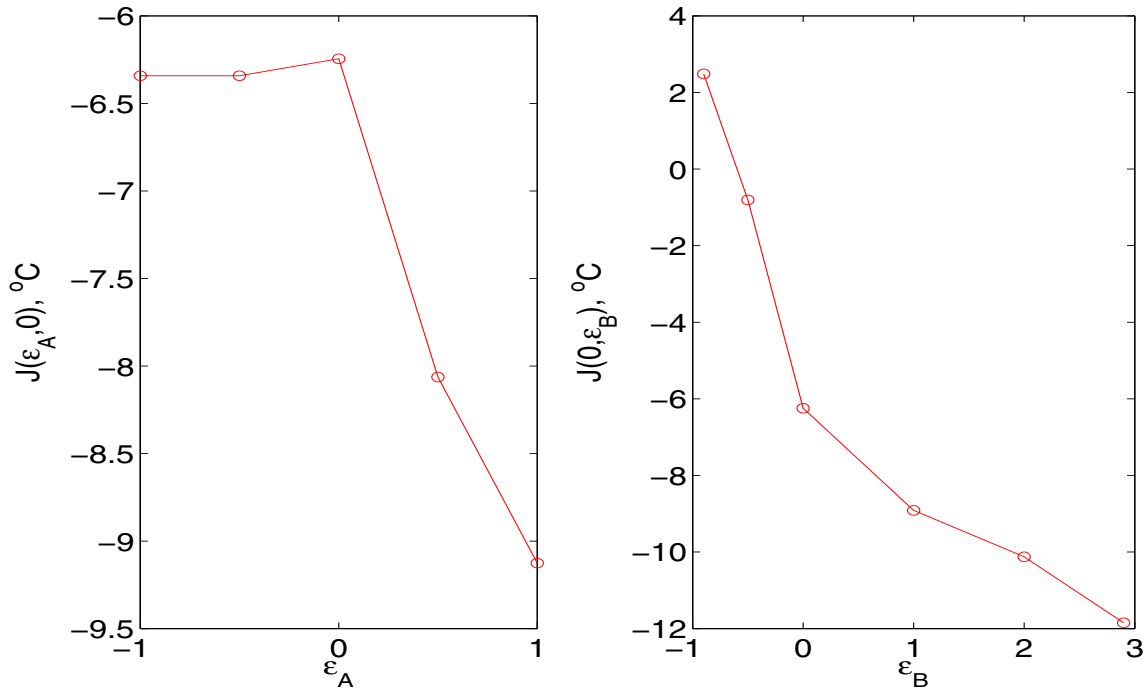
Figure 7.2: *The variability of the cost function to changes in the parameters ϵ_A and ϵ_B for a 'typical' day.*

The sequential process of optimising the parameters in turn, steps 2 to 4, could be continued in a cycle by reevaluating the optimal parameters in turn until convergence. However, in the interests of saving time this sequence is truncated after the first cycle.

The implementation described above was chosen because of its low computer resource requirements. The method is relatively cheap compared to more sophisticated approaches and therefore the implementation of the algorithm over a larger area is possible. A more standard data assimilation approach is to use the least squares

cost function, Equation (5.3) in Section 5.2. Minimising this produces the maximum likelihood estimate which for random, unbiased, Gaussian observations is a minimum variance estimate. For this particular problem the cost function could be adapted to include the constraints. For example

$$J\left(\epsilon_A, \epsilon_B\right) = \sum_{i=1}^{N} \frac{1}{\sigma_i^2} \left(\theta_i - \theta_i^{obs}\right)^2$$

$$- \mu \left[\log\left(\epsilon_A + 1\right) + \log\left(1 - \epsilon_A\right) + \log\left(\epsilon_B + 1\right) + \log\left(3 - \epsilon_B\right)\right] \quad (7.21)$$

could be minimised with respect to the parameters $(\epsilon_A, \epsilon_B, \mu)$. Standard techniques for solving such a non-linear optimisation problem can be found in [46]. However it should be noted that there is no explicit expression for the gradient of J with respect to the control variables. This therefore needs to be estimated first. The value is then used in a descent algorithm to find new control parameters which make the cost function move towards its minimum. Each estimation of the gradient and iteration in the optimisation algorithm requires an evaluation of J which can only be found by running the model over the time window. A more advanced method, such as this, may not be warranted and the increased computational time required would need to be justified before being implemented.

7.4 Results

This new algorithm was first tested with SEVIRI observations in the same region used in Section 6.5 ($-45\,°$N to $-25\,°$N in latitude and $300\,°$E to $330\,°$E in longitude). See Figure 7.9 which shows the region. The simulation was performed from 1st–7th January 2006; this therefore required seven consecutive 24 hour assimilation cycles for each location.

7.4.1 Initial Findings

Various implementations of the algorithm in Section 7.3.2 were initially tested, these include:

1. Control

   Step 1 only, the parameters, ϵ_A and ϵ_B, are set to zero.

2. Wind Only

   Here only the wind value is corrected thus only the parameter ϵ_B is tuned. Therefore step 4 is not required.

3. Cloud Only

   As above except cloud cover rather than wind speed is corrected.

4. Wind then Cloud

   The wind speed value is corrected first followed the cloud value as originally described.

5. Cloud then Wind

   As above except the cloud cover correction is determined first followed by the wind speed correction.

6. Wind and Cloud

   In this approach the wind and cloud parameters are determined together. To find an 'optimal' parameter pair a first order Taylor expansion of two variables is used

   $$J(\epsilon_A + \Delta\epsilon_A, \epsilon_B + \Delta\epsilon_B) = J(\epsilon_A, \epsilon_B) + \Delta\epsilon_A \frac{\partial J(\epsilon_A, \epsilon_B)}{\partial \epsilon_A} + \Delta\epsilon_B \frac{\partial J(\epsilon_A, \epsilon_B)}{\partial \epsilon_B}. \quad (7.22)$$

   By choosing $(\epsilon_A, \epsilon_B) = (0,0)$ and $(\Delta\epsilon_A, \Delta\epsilon_B) = (\epsilon_A, \epsilon_B)$, and denoting $S_A = \frac{\partial J_0}{\partial \epsilon_A}$ and $S_B = \frac{\partial J_0}{\partial \epsilon_B}$, Equation (7.22) can be rearranged as

   $$\epsilon_B = -\frac{S_A}{S_B}\epsilon_A + \frac{J - J_0}{S_B}. \quad (7.23)$$

   This is an equation of a straight line in parameter space (ϵ_A, ϵ_B). If a value for $J = J(\epsilon_A, \epsilon_B)$ is chosen such that $0 \leq |J| \leq |J_0|$ then an equation in two unknowns (ϵ_A and ϵ_B) results, reducing the problem to two degrees of freedom. As before an iteration reduces J and checks whether the line, Equation (7.23), falls within the trust region. When J reaches zero or the line moves outside the

trust region the optimal parameters, $(\epsilon_A^*, \epsilon_B^*)$, are then chosen as the mid-point of the line, Equation (7.23), within the trust region, Equation (7.10) or (7.11). This is shown in Figure 7.3.
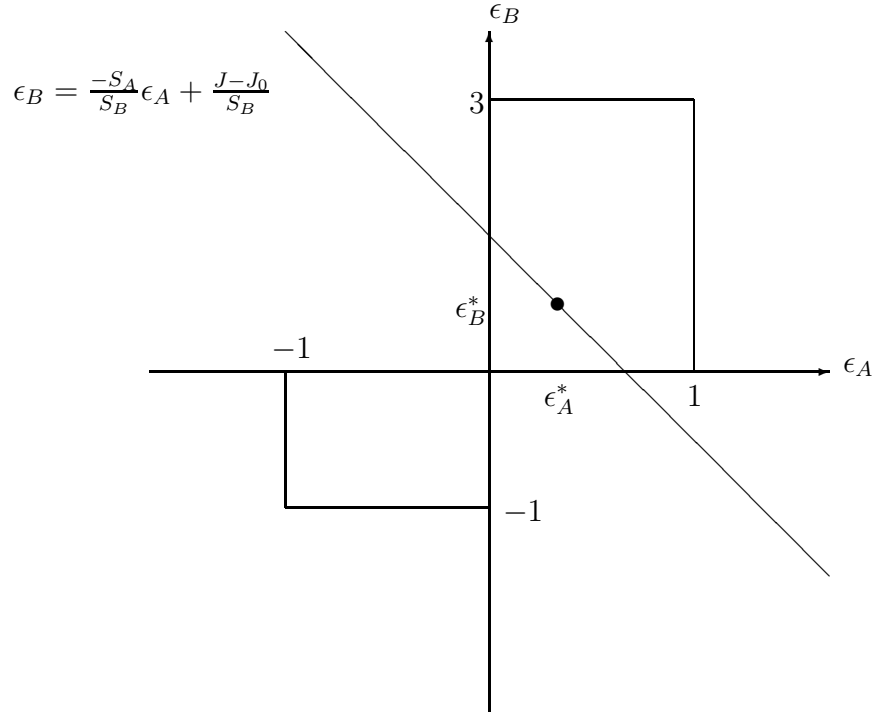

Figure 7.3: *A sketch of the parameter space* (ϵ_A, ϵ_B) *with 'optimal' parameters* $(\epsilon_A^*, \epsilon_B^*)$ *chosen as the mid-point of the portion of the line within the feasible limits.*

Results from these different implementations of the data assimilation algorithm are given in Table 7.1.

It can be seen that the mean differences are low in all cases, except the cloud only run, indicating no significant bias. The RMS differences are reduced by the assimilation in all cases, with the greatest reduction ($0.19\,°\mathrm{C}$) occurring in the wind then cloud case. This is an improvement of 35% and shows that the assimilation provides much better SST estimates than the control, although the mean error is slightly worse. On a few occasions a correction from the assimilation caused the model to become unstable, therefore the numbers in parenthesis show results calculated only at locations and days simulated in all cases. The wind followed by cloud correction performs better than the cloud then wind correction, this is because the SST is found to have a greater

	Mean	RMS	STD
Control	0.02 (0.02)	0.55 (0.57)	0.55 (0.55)
Cloud Only	-0.16 (-0.16)	0.47 (0.47)	0.44 (0.44)
Wind Only	0.01 (0.01)	0.42 (0.42)	0.42 (0.42)
Cloud then Wind	-0.02 (-0.02)	0.39 (0.39)	0.39 (0.39)
Wind then Cloud	-0.06 (-0.06)	0.36 (0.36)	0.36 (0.36)
Wind and Cloud	-0.02 (-0.02)	0.40 (0.40)	0.40 (0.40)

Table 7.1: *Results showing the mean, RMS, and STD of $\theta_{0.015m} - \theta_{SEVIRI}$, in $^\circ C$, for the area $-45\,^\circ N$ to $-25\,^\circ N$ and $300\,^\circ E$ to $330\,^\circ E$ during 1st–7th January 2006. The numbers in parenthesis compare only those results calculated at locations and days simulated in each case.*

sensitivity to changes in wind than changes in the cloud cover. For example, if the cloud correction is made first then the smaller sensitivity will lead to unreasonably large changes in cloud cover to provide the SST change, whereas if the cloud correction is made after a wind correction then the remaining change needed in modelled SST is much smaller and so the less sensitive cloud cover parameter is suitable. The most effective method is to tune first the wind speeds and then the cloud cover.

7.4.2 Combining IR and MW Observations

The SEVIRI observations are IR measurements and therefore are unable to penetrate through clouds. This additional information can be used in the assimilation routine. The proximity confidence values chosen for this study (see Section 6.3) suggest SEVIRI data are far from any clouds. Therefore if an IR observation is available then the cloud cover value at this time must be zero, i.e. clear sky. Because IR radiometers are unable to view through cloud there are many occasions where SST observations are absent (roughly half the globe is thought to be covered by cloud at any one time [82]) and model output can not be constrained. In this section the use of the assimilation method is extended to incorporate MW observations (from AMSRE and TMI). Where

evaluating model-observation differences using IR measurements, the comparison is to the parameterised modelled skin temperature (see Section 3.5.9) whereas for the MW measurements the comparison is with the top modelled SST, at a depth of $0.015\,\mathrm{m}$, without the cool skin effect. Results from this improved method are presented in Table 7.2. Model output is compared separately to IR observations only and combined IR and MW observations. The control simulation makes no corrections to the forcing data. The cloud check runs reduce cloud cover to zero in the presence of IR observations. The wind runs perform the cloud check followed by an adjustment to the wind speeds. Finally, the wind then cloud runs perform the cloud check then adjust wind speeds followed by adjusting cloud cover values (in the presence of MW observations only).

	Mean	RMS	STD
IR: control	−0.25	0.62	0.57
IR and MW: control	0.07	0.79	0.79
IR: cloud check	−0.25	0.62	0.57
IR and MW: cloud check	0.06	0.78	0.78
IR: wind	−0.02	0.34	0.33
IR and MW: wind	0.10	0.53	0.52
IR and MW: wind then cloud	0.07	0.49	0.49

Table 7.2: *Results showing the mean, RMS, and STD of $\theta_{model} - \theta_{obs}$, in $°C$. For the area $-45\,°N$ to $-25\,°N$ and $300\,°E$ to $330\,°E$ during 1st–7th January 2006.*

It is noticeable that with the inclusion of MW observations the mean differences increase by $0.32\,°C$ in the control case. This switch in the bias indicates that, for this area and time period at least, the IR observations are on average warmer than the model and the MW observations are cooler than the model. With the inclusion of MW observations the RMS errors have also increased. The cloud check seems to have had only a very slight influence on the statistics; this may indicate that initial cloud estimates were already zero, or low, in these areas and therefore no, or small, corrections

were necessary. If the SST observations are then used to adjust the wind forcing then the errors are significantly reduced with the RMS differences falling to 0.34 °C in the IR case and 0.53 °C in the IR and MW case. This is further reduced when a correction is made to cloud cover values at occasions when only MW observations are present. The resulting model-observation differences after assimilation may now be approaching the expected accuracy of the observations with the standard deviations (STD) below those quoted in Table 6.1.

Figure 7.4 shows an example of the results of the IR and MW: wind then cloud assimilation run. It can be seen that the model run is initialised to OSTIA at the start of each day. At this location no observations occurred during the first day (1st January 2006). During the last two days a diurnal signal in the satellite observations can clearly be marked out. The model control appears to under estimate the warming on these occasions. However earlier in the week the modelled diurnal warming estimates are much larger than observations seem to suggest. The data assimilation method reduces the cloud, if necessary, in the presence of SEVIRI observations, followed by a correction to the wind speed forcing and then the cloud fractions (when SEVIRI observations are not present). The assimilation is able to reduce the modelled warming for days 2 through to 5, and increase the diurnal warming on days 6 and 7, thus fitting the observations much more closely. On day 2 and 5 the assimilation has not been able to reduce the warming as much as the observations would suggest. In these cases the system does not adhere to the assumptions of the assimilation routine and thus the assimilation is less effective.

In Figures 7.5 – 7.8 results from neighbouring locations are shown. The consistency of the changes in modelled SST induced by the assimilation at these nearby locations suggest that the SST corrections are sensible. The changes produced by the assimilation run are calculated independently at each location. In Figure 7.5 (−29 °N, 315 °E) the results are almost identical except the warming on day 3 is not reduced as much as previously. Further south in Figure 7.6 (−29 °N, 315 °E) only one observation is present on day 2 and this causes a larger diurnal cycle, against the trend at nearby locations. On day 7 at (−29 °N, 315 °E) and (−30 °N, 314 °E) the observations suggest the diurnal

Figure 7.4: *A graph comparing the model SST before and after assimilation with the individual satellite observations and OSTIA at $(-30\,°N, 315\,°E)$ for the 1st–7th January 2006.*

warming is close to that estimated by the control, unlike the other locations where the control is deemed an under estimation. At $(-30\,°N, 314\,°E)$ in Figure 7.8 on day 5 OSTIA shows a warm bias compared to the observations and this is likely the cause of the assimilation run to fail at this point.

7.4.3 Spatial Patterns

The estimates of the diurnal warming of SSTs can also be viewed spatially over the whole area. These results are shown in Figure 7.9. In this figure the plots in the left column show the diurnal warming before assimilation and the plots in the right column after assimilation. The progress down the column displays how the diurnal warming pattern evolves over time, day by day. The white triangle in the top left hand corner is the coast of South America. Generally speaking the assimilation seems to have weakened the diurnal signal in areas of strong modelled diurnal warming. Areas
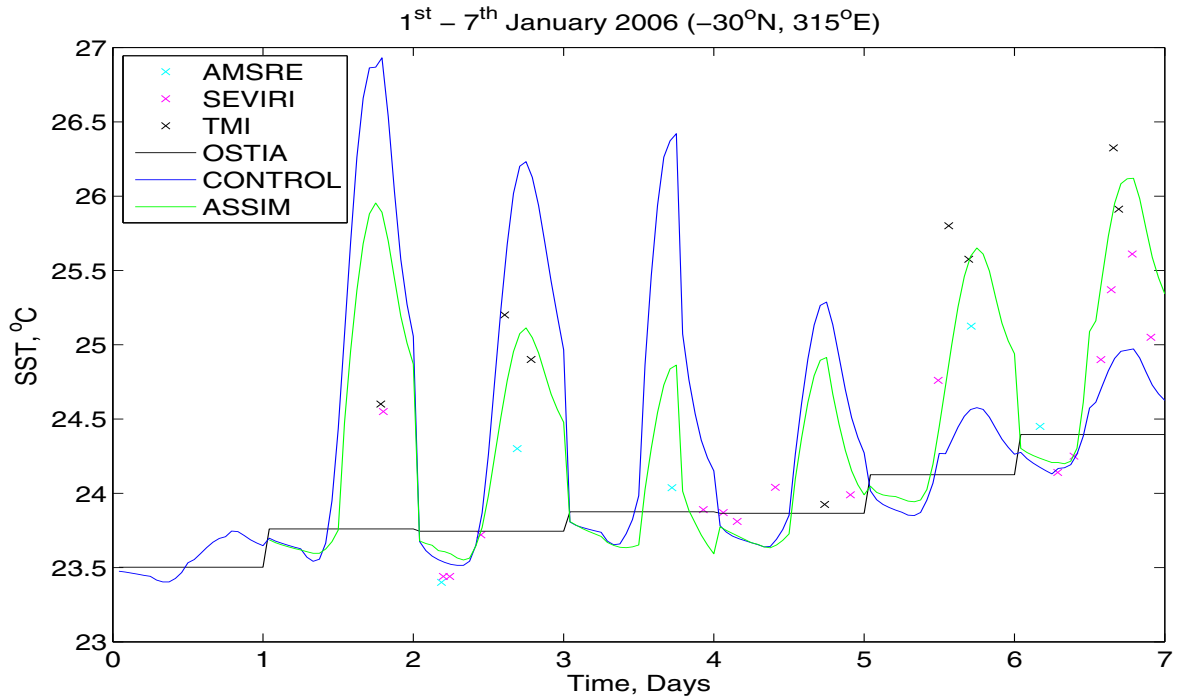
Figure 7.5: *A graph comparing the model SST before and after assimilation with the individual satellite observations and OSTIA at $(-29\,^{\circ}N,\ 315\,^{\circ}E)$ for the 1st–7th January 2006.*

Figure 7.6: *A graph comparing the model SST before and after assimilation with the individual satellite observations and OSTIA at $(-31\,^{\circ}N,\ 315\,^{\circ}E)$ for the 1st–7th January 2006.*

Figure 7.7: *A graph comparing the model SST before and after assimilation with the individual satellite observations and OSTIA at $(-30\,^{\circ}N,\ 316\,^{\circ}E)$ for the $1^{st}\text{–}7^{th}$ January 2006.*
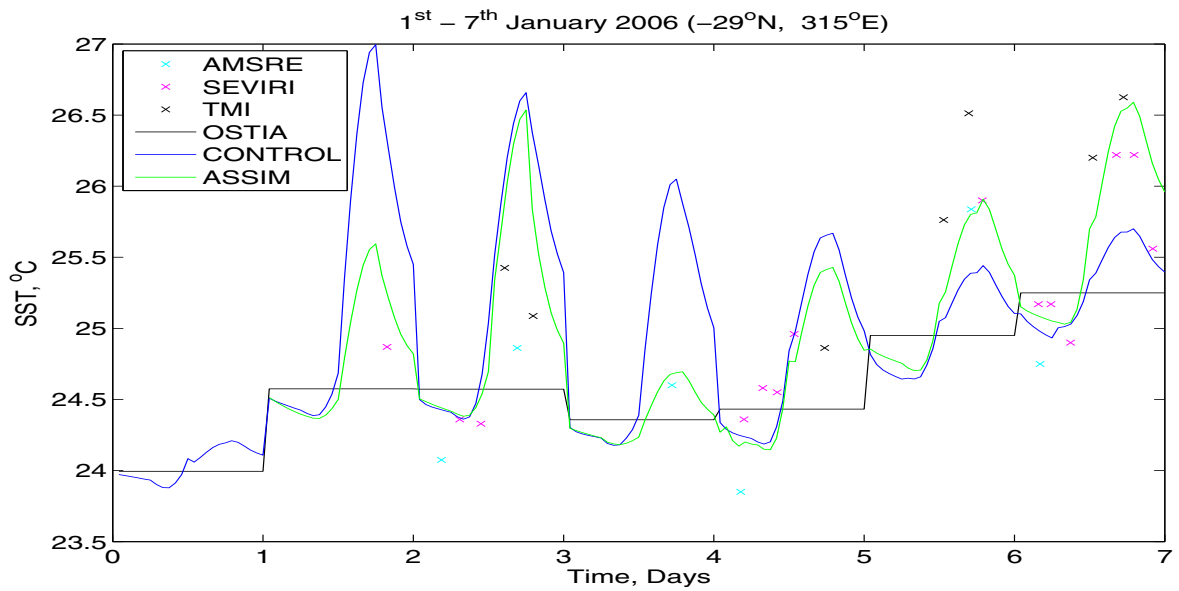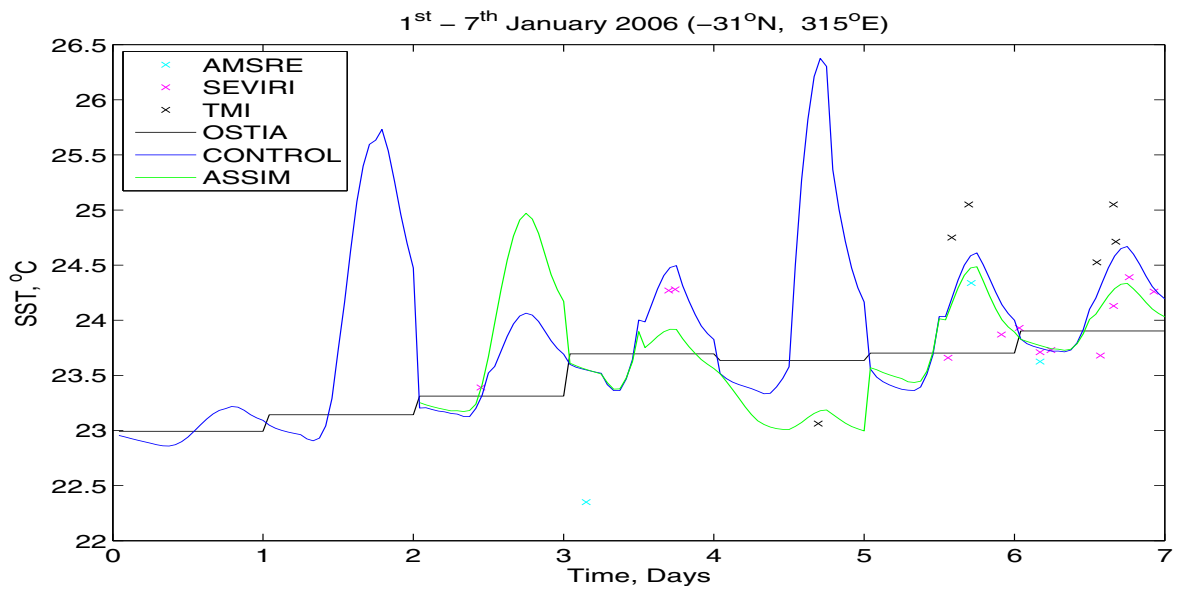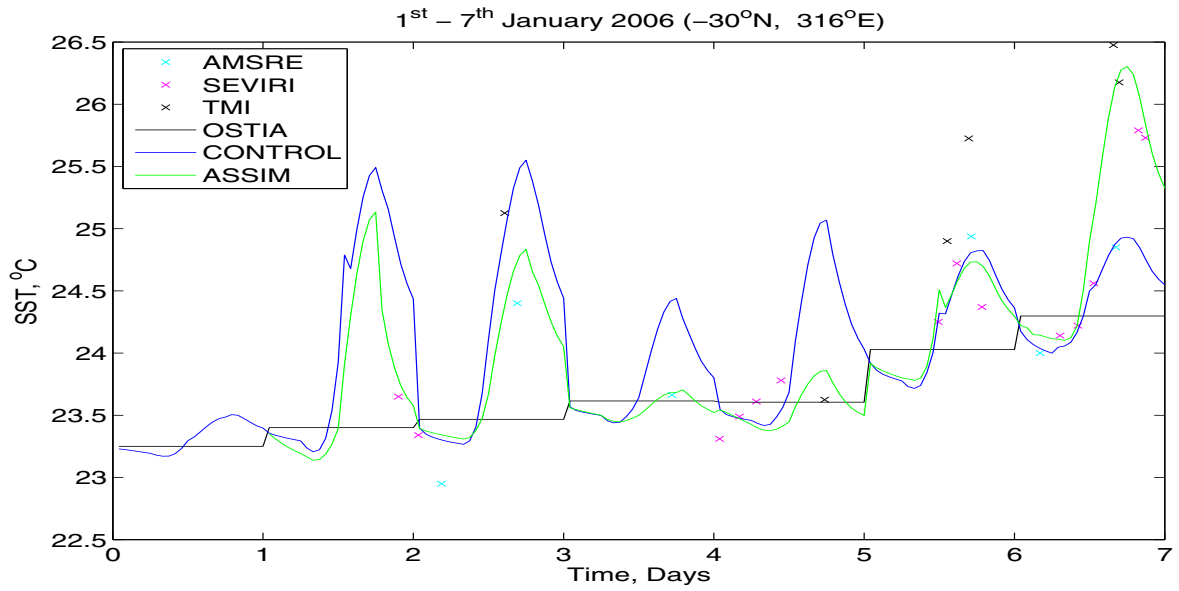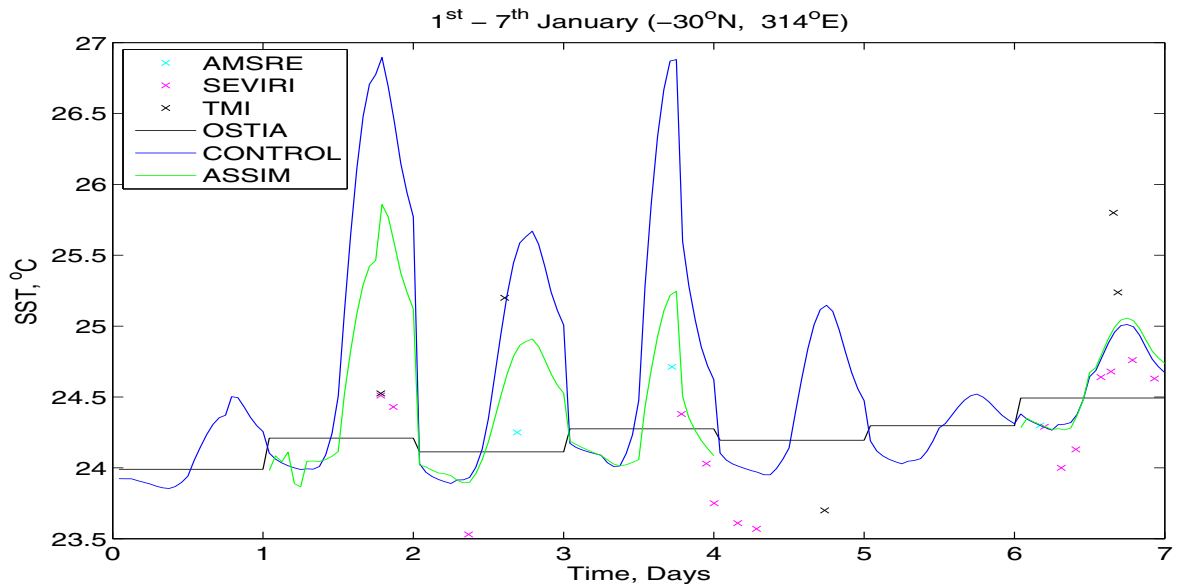

Figure 7.8: *A graph comparing the model SST before and after assimilation with the individual satellite observations and OSTIA at $(-30\,^{\circ}N,\ 314\,^{\circ}E)$ for the $1^{st}\text{–}7^{th}$ January 2006.*

where the assimilation has increased warming can also be seen, particularly on the 6th and 7th of January 2006. The patch of warming occurring on the 6th January 2006 appears less intense and more spread out after the assimilation. On the 7th January the modelled estimates before assimilation show two separate patches of strong diurnal warming. After assimilation the warming in the north-eastern corner again appears less intensified and seems to spread towards the coast. The other patch of strong warming is shown to have moved much further to the south-west. The assimilation only works at locations where observations are present. These areas are identified in Figure 7.10; this figure is identical to Figure 7.9 except the white patches in the right columns are areas where no satellite observations were available, and on these occasions the initial model estimates remained unchanged.

The changes to the forcing can be viewed in Figures 7.11 and 7.12. The daily averaged wind stress is changed by adjustments to the wind speeds in the assimilation and the daily peak SWR will be affected by adjustments to cloud cover in the assimilation. What is immediately noticeable in these graphs are the less smooth fields after assimilation. This is a consequence of using 1-D models, while the initial fields are provided from a global 3-D atmospheric model, the adjustments to the wind fields and cloud cover distributions are determined independently at individual locations. Such changes would normally be smoothed horizontally and the information spread from areas high in observations to areas with low observation densities. However, diurnal warming is an irregular feature because it is susceptible to patches of cloud cover and fine scale wind bursts. Therefore it would not necessarily be desirable to smooth these fields.

7.4.4 Comparing Different Satellite Observations

Further analysis was also performed to assess the relative errors associated with individual observation types and these are presented in Table 7.3.

A similar number of SEVIRI and AMSRE observations are available over the time period in this area, with fewer TMI observations. The model-observation match-ups reveal differences between the three satellite instruments. The SEVIRI observations are shown to be on average warmer than the parameterised skin temperature, whereas

131
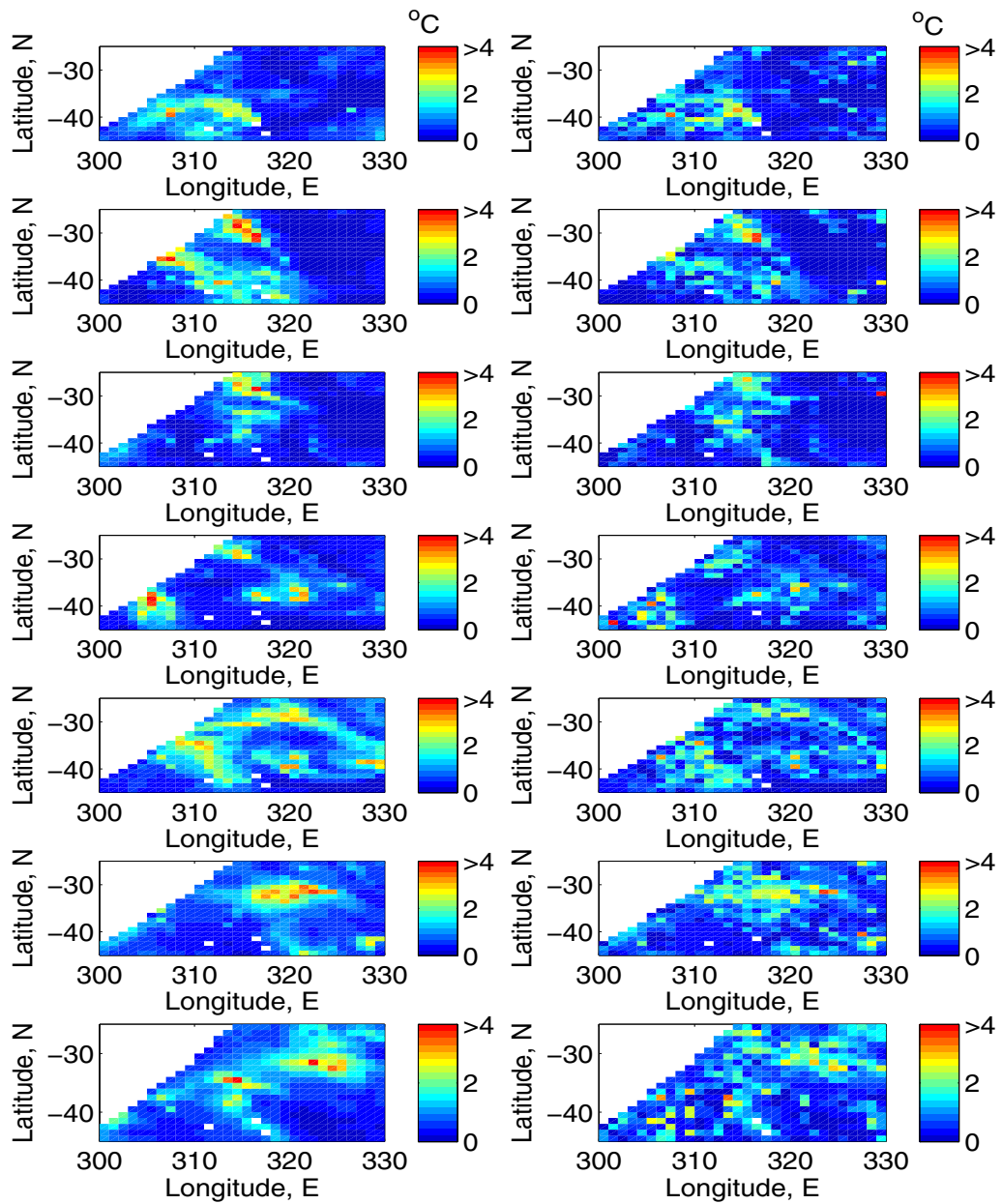
Figure 7.9: *The maps in the left column show modelled diurnal warming estimates before data assimilation and the those in the right column diurnal warming estimates after assimilation (values in $^{\circ}C$). The maps down the columns represent successive days from 1st to the 7th January 2006.*
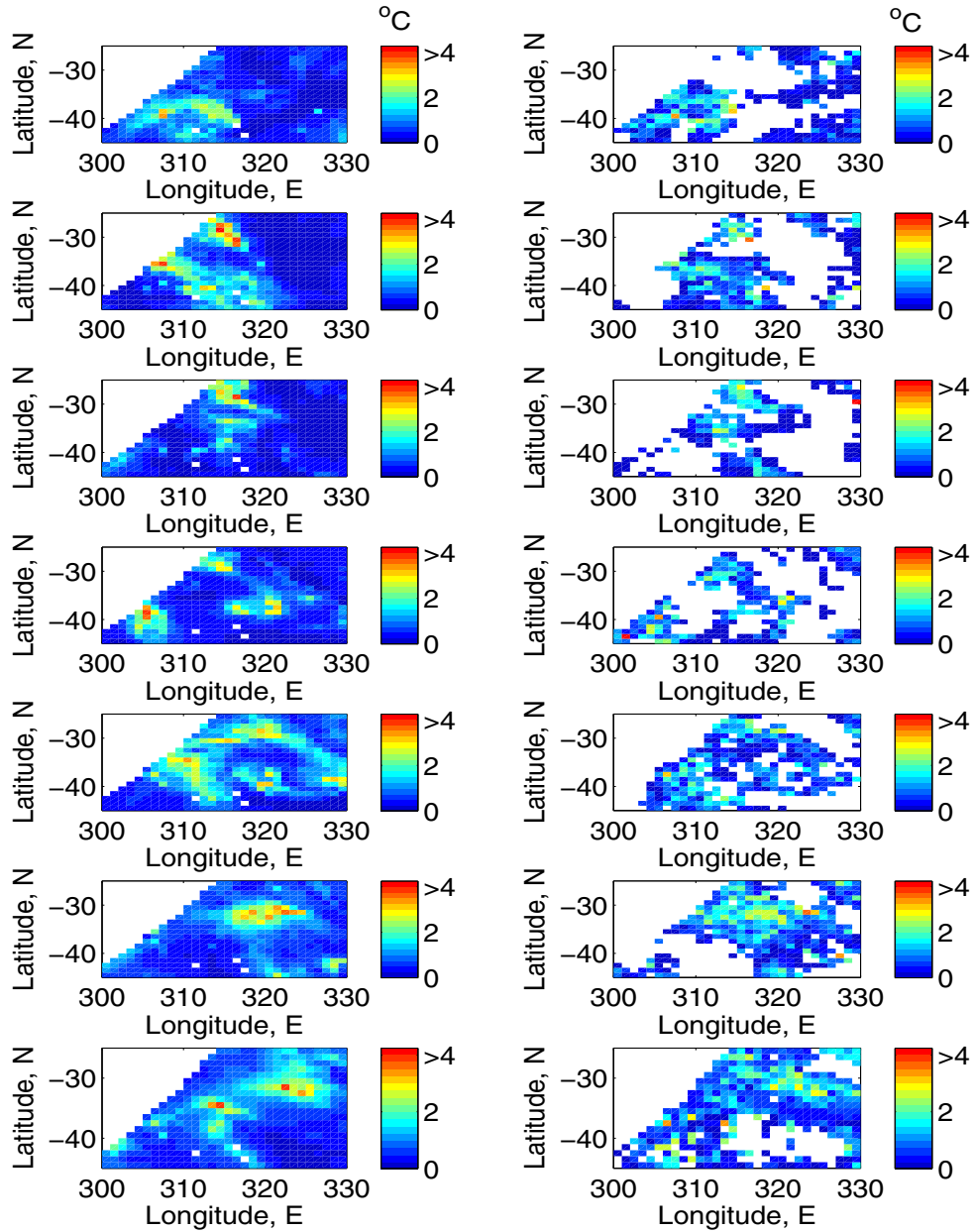
Figure 7.10: *The maps in the left column show modelled diurnal warming estimates before data assimilation and the those in the right column diurnal warming estimates after assimilation (values are only shown where satellite SST observations were available). The maps down the columns represent successive days from 1st to the 7th January 2006.*
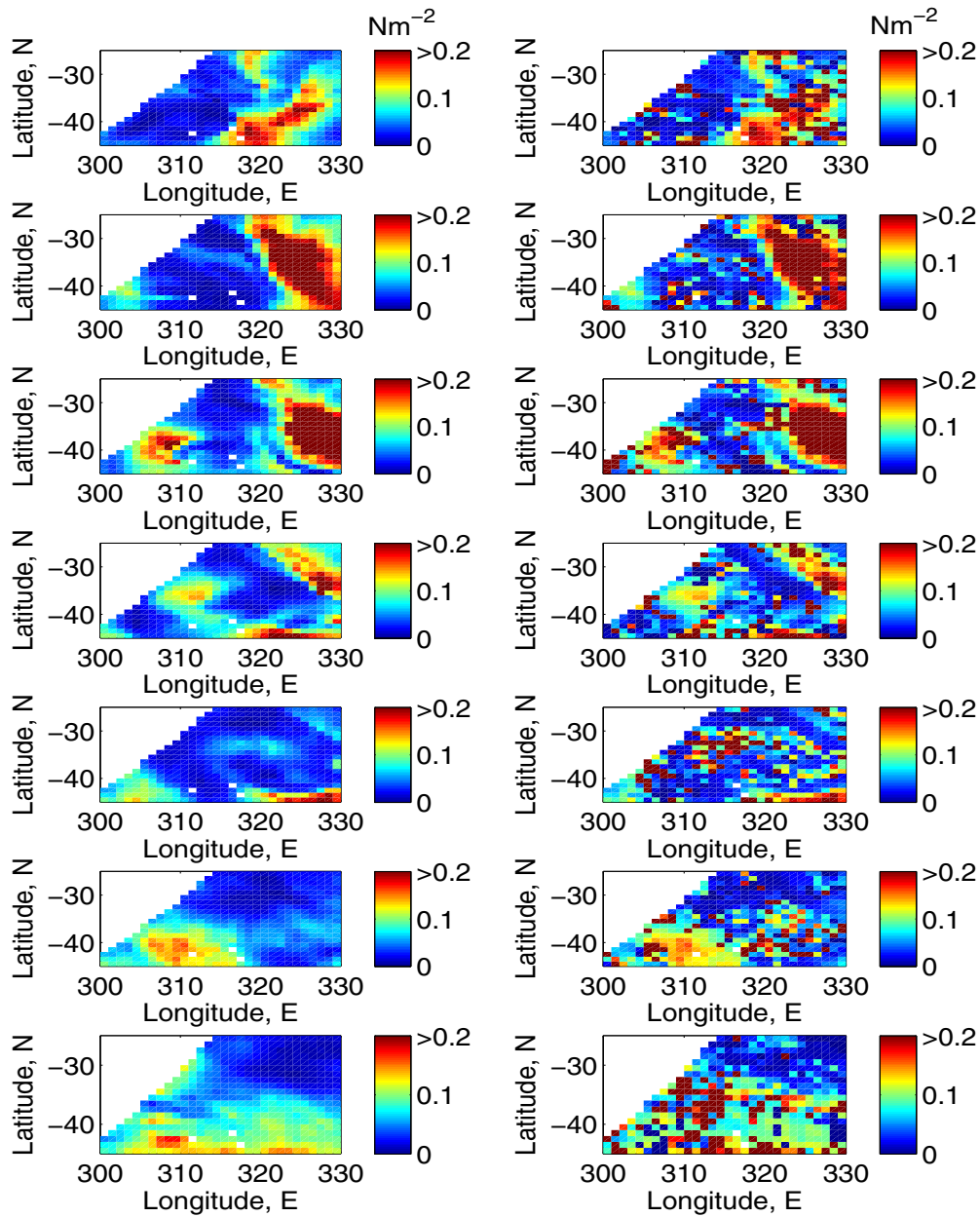
Figure 7.11: *The maps in the left column show the daily mean wind stress before data assimilation and the those in the right column are after assimilation (values in Nm^{-2}). The maps down the columns represent successive days from 1st to the 7th January 2006.*

Figure 7.12: *The maps in the left column show daily peak SWR before data assimilation and the those in the right column are after assimilation (values in Wm^{-2}). The maps down the columns represent successive days from 1st to the 7th January 2006.*
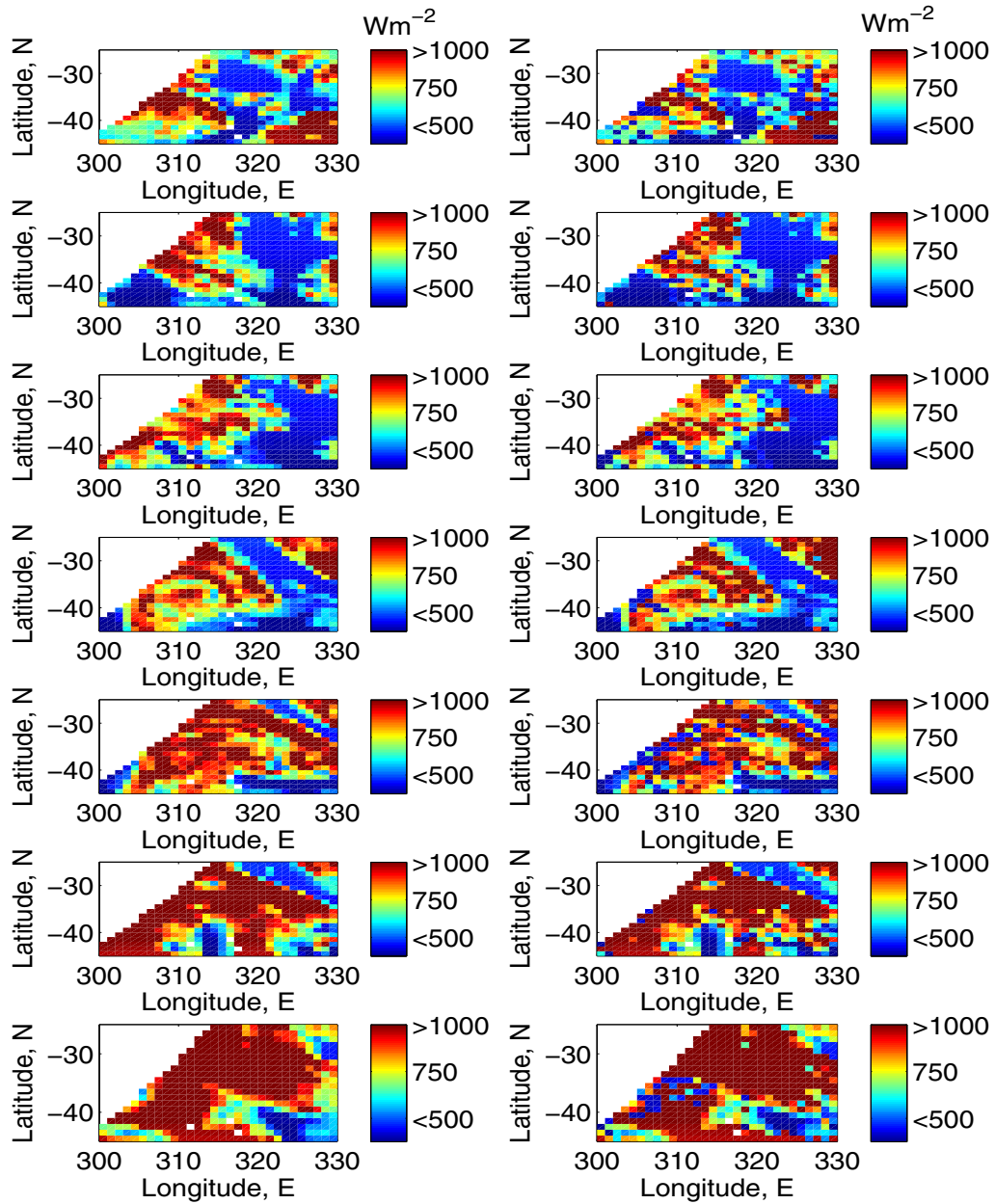
	No. Obs.	Mean	RMS	STD
SEVIRI only	2343	−0.25	0.62	0.57
AMSRE only	2220	0.20	0.80	0.77
TMI only	1532	0.37	0.98	0.91

Table 7.3: *Results showing the number of observations, the mean, RMS, and STD of* $\theta_{control} - \theta_{obs}$*, in* °C*, for individual satellite types. For the area* $-45\,°N$ *to* $-25\,°N$ *and* $300\,°E$ *to* $330\,°E$ *during* 1st*–*7th *January 2006.*

the AMSRE and TMI observations are cooler on average than the modelled SST. This suggests that the observations have some systematic errors in this area at this time, with SEVIRI SST systematically too warm and/or AMSRE and TMI observations systematically too cool. The model could also have a warm bias and be estimating too great a cool skin correction. This seems unlikely as the parameterised cool skin correction for this period was on average 0.15 °C, i.e. smaller than the SEVIRI only mean difference. The model simulations are dependent on the OSTIA SST at the start of each day; therefore any errors in OSTIA will also be apparent (see Section 7.4.6). The RMS and STD are significantly lower when comparing SEVIRI observations with either AMSRE or TMI. The largest errors are found with the TMI observations, where the RMS error approaches 1 °C.

7.4.5 Day-Night Comparisons

Differences in night time (between the hours 22:00–04:00 local time) and daytime (between the hours 10:00–16:00 local time) match-ups were also compared. The results shown in Table 7.4 indicate much larger mean differences during daytime. It looks likely that the model is over estimating the diurnal warming signal. An alternative explanation could be that the retrieval algorithms have inadvertently suppressed the true warming signal. The RMS and STD differences remain similar for both day and night.

136

	No. Obs.	Mean	RMS	STD
daytime	2799	0.14	0.53	0.51
night time	1365	0.00	0.50	0.50

Table 7.4: *Results showing the number of observations, the mean, RMS, and STD of* $\theta_{analysis} - \theta_{obs}$, *in* $^\circ C$, *during daytime (10–16) and night time (22–04) local time. For the area* $-45\,^\circ N$ *to* $-25\,^\circ N$ *and* $300\,^\circ E$ *to* $330\,^\circ E$ *during* 1st–7th *January 2006.*

7.4.6 Comparisons to OSTIA

To further determine whether the biases are due to model or observations the individual satellite observations were also compared to the OSTIA value.

	No. Obs.	Mean	RMS	STD
SEVIRI only	2525	−0.22	0.56	0.51
AMSRE only	2256	−0.08	0.70	0.69
TMI only	1532	−0.20	0.87	0.84
all obs	6333	−0.17	0.69	0.67
daytime SEVIRI only	721	−0.51	0.76	0.56
daytime AMSRE only	1249	−0.29	0.77	0.71
daytime TMI only	1345	−0.22	0.89	0.86
daytime all obs	3315	−0.31	0.82	0.76
night time SEVIRI only	535	0.06	0.38	0.37
night time AMSRE only	1003	0.19	0.59	0.56
night time TMI only	0	–	–	–
night time all obs	1538	0.14	0.53	0.51

Table 7.5: *Results showing the number of observations, the mean, RMS, and STD of* $\theta_{OSTIA} - \theta_{obs}$, *in* $^\circ C$, *including daytime (10–16) and night time (22–04) local time. For the area* $-45\,^\circ N$ *to* $-25\,^\circ N$ *and* $300\,^\circ E$ *to* $330\,^\circ E$ *during* 1st–7th *January 2006.*

The results shown in Table 7.5 reveal that SEVIRI has the largest bias but small-

est RMS difference of the three instruments when compared to OSTIA. The biases are all negative for daytime observations and all positive for night time observations. However, the daytime biases are larger and when comparing all 6333 observations a bias of $-0.17\,^\circ$C is found. Indicating the satellite observations on average are warmer than OSTIA. The sharp difference in day and night time mean values demonstrates the presence of diurnal signals in the daytime observations. OSTIA is the mean value of these observations, as well as others, and so the expectation is that the bias would be small. In this match-up all observations are included whereas OSTIA is formed by eliminating daytime observations taken with wind speeds less than $6\,\mathrm{ms}^{-1}$. These additional observations are therefore contributing to the slight cool bias in OSTIA. Comparing results in Tables 7.5, 7.4, and 7.2 indicates that the modelled control simulation results in a smaller mean error than OSTIA, but produces slightly larger RMS and STD errors than OSTIA. However after data assimilation of the L2P satellite data the analysis is a much better representation of the observed SSTs with reduced mean, RMS, and STD. For example moving from the persistence assumption of OSTIA to assimilating into the diurnal cycle model reduced the RMS error by $0.2\,^\circ$C.

7.4.7 Using Satellite Wind Measurements

The AMSRE and TMI instruments also measure wind speeds and this data is provided with the GHRSST-PP L2P products. These observations when available may provide an improvement on the ECMWF forecast winds. Therefore model simulations were performed in which the satellite wind measurements were used for the 6 hour periods when available. The model requires the wind components u and v and so the ECMWF values were adjusted by the same factor so that $w = \sqrt{u^2 + v^2}$ was made equal to the satellite derived value. This model (control) simulation resulted in an improved mean model-observations SST difference of $0.17\,^\circ$C and a similar RMS difference of $0.78\,^\circ$C when compared to results using ECMWF winds only (see IR and MW: control in Table 7.2).

The availability of these satellite wind measurements also allows for a comparison to be made between the original ECMWF wind values and the corrected wind values

after the assimilation. These results are presented in Table 7.6.

	No. Obs.	Mean	RMS	STD
ECMWF-AMSRE	2009 (1635)	−0.07 (−0.12)	1.76 (1.72)	1.76 (1.71)
ASSIM-AMSRE	1635	−0.23	2.74	2.73
ECMWF-TMI	1278 (1212)	−0.49 (−0.49)	1.68 (1.60)	1.61 (1.52)
ASSIM-TMI	1212	−0.45	2.57	2.53
ECMWF-ALL	3287 (2847)	−0.23 (−0.28)	1.73 (1.67)	1.71 (1.64)
assim-ALL	2847	−0.33	2.67	2.65

Table 7.6: *Results comparing the ECMWF forecast wind speeds before and after assimilation to the AMSRE and TMI wind measurements showing the number of observations, the mean, the RMS, and STD differences in ms^{-2}. For the area $-45\,^{\circ}N$ to $-25\,^{\circ}N$ and $300\,^{\circ}E$ to $330\,^{\circ}E$ during 1st–7th January 2006. The numbers in parenthesis are calculations only at the locations and times when wind speeds are corrected in the assimilation.*

The results in Table 7.6 reveal that the satellite measured winds, particularly from TMI, are slightly stronger than the ECMWF forecasted values. The RMS differences between the ECMWF winds and all the satellite derived winds is $1.73\,ms^{-1}$. After the ECMWF winds have been corrected in the assimilation process the RMS is approximately increased by $1\,ms^{-1}$ in all cases. However the resulting error is just outside the quoted mission accuracy of the AMSRE product $(1\,ms^{-1})$ [79], although validation against buoy and scatterometer data at very low wind speeds is particularly difficult [79].

7.5 Summary

In this chapter a data assimilation method has been developed that assimilates satellite derived SST observations into a diurnal cycle model. It is proposed that model errors in diurnal warming estimates are primarily caused by uncertainties in NWP forcing data. Other sources of errors, such as errors in model parameterisations and incorrect vertical

structure after assimilation of OSTIA data are addressed earlier in the thesis. It is also noted that the sources of modelled diurnal warming errors were slightly different at the mooring sites (see Chapters 4 and 5); for example, at these locations the forcing wind speed observations were known to a high degree of accuracy and were not considered a major source of uncertainty.

The diurnal variability of SSTs can be viewed as a function of wind speeds and fractional cloud cover. Observations from SEVIRI, AMSRE, and TMI occurring throughout the day are compared to their modelled equivalent. The resulting differences are then reduced by making mean corrections to the forcing wind speeds and cloud cover. This tuning of the forcing is shown to result in modelled SST estimates that resemble available observations much more closely. The assimilation method could be viewed as smoothing and interpolating the satellite SST observations in an intelligent manner. The method is shown, for example, to fit the observations better than OSTIA which uses a daily persistence assumption. In correcting wind speed and cloud cover values, within uncertainty bounds, it also attempts to give a better balance between thermal and dynamical fields.

The method described here could now be implemented on a much wider scale to build up a detailed real time picture of diurnal warming across the world's oceans. The distribution and magnitude of diurnal signals are still relatively unknown and this technique of merging observations with a diurnal cycle model could be used to improve this situation. Another application could be to use this technique to calculate foundation temperatures. For example the method could be used to re-calculate the OSTIA product. In using more of the data (i.e. daytime observations in low wind speeds) and actually calculating the foundation temperature (the temperature from which a diurnal cycle develops) an increase in accuracy could be realised. It is also shown how there is scope to improve on the techniques developed; this could be achieved by implementing a more sophisticated assimilation routine, using a 3-D model with horizontal correlations, and improving our understanding of errors associated with the different satellite data types and model estimates.

Chapter 8

Conclusions

8.1 Thesis Summary

Accurate knowledge of SST is extremely important for ocean and atmospheric sciences, perhaps most crucially for its central role in air-sea flux calculations. The diurnal cycle is a fundamental mode of the climate system and much evidence is presented in Chapter 1 to show how the diurnal variability of SST has impacts on longer timescales. Awareness of the diurnal cycle is also shown to be essential in accurately interpreting satellite derived observations of the SST. In order for satellite SST data to be compatible with the historical climate record of bulk SST, any temperature gradients between the depth of traditional in-situ samplers and the near surface of satellite derived measurements must be accounted for. The magnitude of diurnal thermoclines are significant given the accuracy that SST records aspire to. Consideration of the timing and depth of SST observations in relation to modelled counterparts is therefore required for a more careful approach to assimilating SST data.

The GOTM, a one-dimensional mixed layer ocean model, is used to study and estimate the diurnal variability of the upper ocean. One-dimensional models are useful for this type of study as they can be employed with an adequate fine near surface spatial resolution and temporal resolution to capture diurnal variability. As explained in Chapter 2 the model explicitly resolves or parameterises the fundamental processes involved in the development of the diurnal cycle of SSTs. The system equations and

details of the mixing scheme are documented.

Diurnal stratification is driven by solar radiative warming of the upper ocean. The penetration of SWR into the ocean is an important concept for diurnal cycle modelling. Many parameterisations exist that attempt to resolve the amount of ocean radiant heating at depth; these are outlined in Chapter 3. However only the most advanced methods should be used for modelling the diurnal cycle as it is important to resolve solar transmission variations within the upper few metres. The parameterisation of air-sea fluxes are also extremely important for accurately modelling diurnal variability. The ability to measure air-sea fluxes is limited; therefore their calculation is dependent on parameterisations using commonly available meteorological data. In Chapter 3 a derivation of air-sea flux formulae is given followed by a description of the two algorithms tested in Chapter 4, of which the TOGA COARE method developed by Fairall et al produced the best results.

In Chapter 4 the model was tested at three mooring sites in different parts of the world. Various aspects of upper ocean variability were examined. The model was shown to have very good accuracy in estimating SSTs over the observed time-series. The key sources of error were identified, these were advection events, which are not accounted for in 1-D models, and uncertainty in cloud cover values. Analysis is presented which shows that the SSTs are sensitive to changes in cloud cover on diurnal and longer timescales and therefore knowledge of this parameter is deemed vital. Estimates of diurnal variability were not significantly changed when model forcing was reduced to 6 hourly mean values, highlighting the possible use of NWP fields for diurnal warming estimates.

In Chapter 5 the general data assimilation problem is formulated, where observations are used together with a numerical model to produce an estimate of the state of the system. A detailed review is then presented of the use of such methods for the specific purposes of assimilating SSTs. It is found that SST data assimilation is perhaps an underdeveloped area; difficulties arise in distributing information from the surface into the deeper ocean, accounting for diurnal warming errors, and in adjusting this prognostic variable in a non disruptive manner. Various different approaches to

the SST assimilation problem were experimented with at the mooring sites. One such scheme assimilated the SST increment by correcting all temperatures within the mixed layer. More novel approaches were also explored involving the use of an SST observation to estimate a cloud cover value. However, it was often difficult to attribute an SST error to a particular cause. A discussion was also presented on the possible use of comparing modelled and observed changes in SST to determine errors in the modelled mixed layer depth.

The use of the 1-D model is extended by utilising operational forecast and analysis data sets to initialise and force the simulations. Details are given on how the 6 hourly resolution of the meteorological data can be maximised for the purposes of modelling the diurnal cycle. The estimation of diurnal warming was shown to be sensitive to the use of internal wave and wave breaking parameterisations as well as the type of boundary condition that was implemented. The best performing combination was to use an internal wave mixing parameterisation but not a wave breaking parameterisation and to apply flux boundary conditions for the TKE and dissipation equation. To better represent heat flux and SST feedbacks the air-sea fluxes are computed dynamically as opposed to using prescribed values. The use of remotely sensed SeaWiFS chlorophyll maps is shown to improve the parameterisation of solar absorption within the upper ocean. A cluster of models is run at different locations and used to produce diurnal variability maps on a daily basis over wide areas. The possibility of producing accurate diurnal variability maps, as presented in Chapter 6, is a new and important tool for the SST community. These maps can be utilised by identifying areas of diurnal warming and flagging observations taken in those areas, therefore reducing systematic errors in observational products and assimilation systems.

In using operational data to force the diurnal cycle model, satellite derived observations of SSTs can be used to constrain SST estimates. As satellite observations are available at various times throughout the day, and because they observe a near surface temperature, they are susceptible to diurnal warming. Therefore these observations can be assimilated into the diurnal cycle model. Unlike at the mooring sites, high quality intensively observed forcing data is not available and the use of NWP fields

143

can lead to errors in modelled diurnal warming estimates as a result of incorrect wind speed and cloud cover values. A new method is developed in Chapter 7 that uses the SST observations to derive corrections, within uncertainty bounds, to wind speed and cloud cover values. This is the first time SST data has been assimilated into a diurnal cycle model. Adjusting the forcing to be more consistent with the SST observations is an original approach to the problem. Results are presented which show improvements when using this assimilation algorithm. It is also demonstrated how the method could be implemented on a global scale.

8.2   Main Findings

This thesis opened with an introduction to the subject of SST diurnal variability. Topics that were addressed included, an explanation of the mechanisms that cause warming, the influence diurnal variability has on the ocean-atmosphere system, and its effects on longer time scales, and the relevance of diurnal warming effects for the interpretation and assimilation of satellite derived SST measurements. This exposition highlighted areas where further research was needed and provided the motivation for the specific aims of this thesis, as laid out in Chapter 1. In this next section the key findings from this thesis, in regards to the stated aims, are assembled and presented.

8.2.1   Modelling the SST Diurnal Cycle

Progress has been made in understanding and advancing the ability to numerically model diurnal variability at the near surface. A widely used one-dimensional mixed layer model is optimised for the purposes of diurnal cycle modelling. State-of-the-art parameterisations for air-sea flux and ocean radiant heating calculations are implemented and utilised. The sensitivity of the magnitude of the modelled diurnal cycle, in low wind speed conditions, to the use of internal wave mixing and wave breaking parameterisations, as well as the selection of surface boundary conditions, have been elucidated. It is clearly demonstrated for the first time that accurate diurnal warming estimates can be achieved from model output forced with NWP data. A cluster of

models were run over a wide range of locations and the results used to produce daily spatial maps of the diurnal warming signal in SST. This mesh of models forced with the ubiquitous NWP data has the potential to become a very useful method, viz, in identifying areas of diurnal warming and quantifying diurnal signals in observational SST data.

8.2.2 An Observation Operator for Satellite Derived SST

This thesis has highlighted the depth disparity between SST observations and their model counterparts as well as the lack of model representation of diurnal variability seen in observations. In order to reduce errors in an assimilation procedure an observation operator is needed to transform model variables of bulk temperatures into the skin and sub-skin temperatures of satellite derived SSTs. The reverse is true for producing foundation SST observational products; for this case SST observations 'corrupted' by a signal need to be converted to the base temperature from which the diurnal thermocline has developed. It is demonstrated how a 1-D model equipped with fine near surface resolution and diurnal forcing, as used in this thesis, is an effective dynamic observation operator for the uses outlined here.

8.2.3 Advancement of SST Data Assimilation

A literature review of SST data assimilation techniques carried out in Chapter 5 highlights several shortcomings in current schemes. These include the absence of an observation operator to account for diurnal signals, instabilities and disruptions caused by adjusting prognostic variables, a lack of vertical correlations due to a dearth of vertical model resolution and uncertainty of how information content at the surface can inform the sub-surface, and an imbalance between thermal and dynamical fields which reduces the effectiveness of the assimilation.

The model used in this thesis can be viewed and applied as an observation operator in the data assimilation process, as indicated in the previous section. The model attempts to resolve observable scales and therefore observations can be assimilated

into the diurnal cycle. It is shown how perfect correlations within the mixed layer can be assumed so that night time SST observations can be used to adjust all ocean temperatures in the mixed layer. To reduce the original cause of SST errors attempts were made to account for SST errors by using SST observations to estimate cloud cover values. It is also shown how a comparison between changes in modelled and observed SST could be used to correct mixed layer depths diagnosed by the model. A new and novel SST data assimilation method is developed for assimilating observations in time over a day. Wind speed and cloud cover values are adjusted to induce diurnal warming estimates commensurate with SST observations over the day. This method assimilates observations into the diurnal cycle model. In correcting wind speed and cloud cover values, within uncertainty bounds, it also attempts to give a better balance between thermal and dynamical fields. This assimilation scheme was successfully demonstrated by using a combination of infrared and microwave satellite SST observations in an area of the Atlantic Ocean. It is shown how the scheme effectively smoothes and interpolates the observations over the diurnal cycle, thus reducing errors associated with persistence assumptions.

8.2.4   Diurnal Variability Maps

The progress presented in this thesis establishes a paradigm of how infrared and microwave satellite derived observations can be merged with diurnal modelling output to produce diurnal variability maps. If implemented on a wide scale, utilising NWP fields and global satellite data sets, an accurate picture of the global day to day extent of diurnal warming could be built up. This type of information, on the diurnal variability of SSTs, is vital for climate monitoring and for a better understanding of ocean-atmosphere interaction. Research reviewed in Chapter 1 indicated the influence of diurnal warming on longer timescales, and therefore these maps could be vital in furthering our understanding of the ocean-atmosphere system.

8.3 Future Work

In answering the aims set out in Chapter 1 it is evident that many open problems remain and a number of interesting follow up questions have arisen. In this final section some avenues of future study are outlined.

The problem of how the diurnal cycle of SSTs can be incorporated into operational models remains a major issue. Huge computational requirements are needed to run an ocean or coupled GCM. Resolution is improving all the time with advances in computer technology, but it will be some time before the diurnal cycle is explicitly resolved. In recent years several approaches have been considered to try to mimic diurnal variability, given the current vertical resolution of ocean GCMs.

One approach recently tried by Zeng and Beljaars [158] was to develop a prognostic sea surface skin temperature scheme for modelling and data assimilation. The scheme was implemented into the ECMWF operational model and the skin SST is compared to that measured by the Geostationary Operational Environment Satellite (GOES).

Another proposal originally conceived by McCulloch et al in 2004 [81] and extended by Schiller and Godfrey in 2005 [121] is to include an additional transient model level in the top grid box simulating a variable depth diurnal sub-layer. A one-dimensional mixed layer model with 10 m resolution and with the sub-layer simulates diurnal SSTs close to those observed from the TOGA COARE with typical errors of about 0.1 °C. The impact of improved SSTs on surface heat fluxes is also shown by coupling the 1-D mixed layer model with sub-layer, to an atmospheric boundary layer model.

A further approach is to develop empirical formulae to estimate the diurnal skin SST based on atmospheric conditions (e.g. wind and solar radiation). This has been used in modelling studies: for example, Wei et al [153] used a parameterisation by Webster et al [151] to improve SST simulation in the western Pacific. However, mostly these parameterisations have been developed for observational studies: Stuart-Menteth et al [136] used the Kawai and Kawamura regression model [68] in a global study of AVHRR diurnal warming patterns, Gentemann et al [42] developed a parameterisation for interpreting diurnal signals in AVHRR and TMI SST measurements, and Nardelli

et al [91] used the parameterisation of Stuart-Menteth et al [137] in an attempt to remove diurnal warm layer effects from AVHRR daytime images.

It is uncertain which route will ultimately provide the best results, but it is anticipated that this will be an active area of research over the next few years. Because diurnal warming has potential effects on climate phenomena, especially in the tropics (see Chapter 1), it is essential that coupled ocean-atmosphere models start to utilise tools such as the transient sub-layer. The work from this thesis could inform and lead to further improvements in these various parameterised approaches. Further improvements would most certainly be achieved with careful assimilation of observations. Further work would seek to implement these schemes together with the assimilation method developed in this thesis to provide a robust operational approach to the problem. A thorough analysis of the impact of a diurnal scheme on climate modelling and data assimilation is a worthy future task.

The limitation of empirical models, developed from regression analysis of SST observations, is that they have been based on a particular type of observation in a particular area. It is very difficult to develop a parameterisation that captures diurnal warming under all realistic conditions because of the complex non-linear responses at play in the ocean-atmosphere system. The model developed in this thesis could be used to create a more universal diurnal warming parameterisation: differing forcing scenarios can be simulated and the output analysed to further understand the mechanisms at play.

This thesis has demonstrated a new method of merging infrared and microwave satellite SST data with diurnal cycle model output to provide estimates of the diurnal warming. The method was successfully tested for a week at locations in the southern Atlantic Ocean. This methodology can now be implemented on a global scale over long periods of time, providing a detailed database on the extent and variability of diurnal warming. It is believed the analysis of results from this type of wider implementation would provide much needed quantification of diurnal warming at certain times in specified locations and under a range of conditions. Further analysis could also be carried out into the suggested changes in the NWP air-sea fluxes as a result of the changes in SST and the corrections brought about by the assimilation algorithm. Other di-

agnostics of interest would include comparing the mixed layer depths as estimated by FOAM and GOTM.

The work carried out in this thesis could certainly form the basis of a more comprehensive system that could be developed for an operational centre producing an SST product. The method developed here could be used purely for quantifying diurnal warming estimates at observation times. The removal of the diurnal warming signal in SST observations would produce more accurate observational foundation SST products. Further work would be needed to extend the method to include as many observation types as are available, but this would also require additional computer time to manage the increase in data input. As the system develops, more insights into the likely errors associated with individual observation types will emerge and a better account of error statistics in the data assimilation process will be needed. Further work on the likely associated errors in modelled diurnal warming estimates when forced with 6 hourly NWP data would enable a better quantification of model error in the assimilation system. Other improvements could include implementing a more advanced data assimilation method as outlined in Section 7.3.3, but this would require additional computer time to run. Another improvement could be to embed the 1-D vertical model into a 3-D model. This type of implementation would reduce errors caused by advection and provide a more natural setting to include horizontal correlations in the data assimilation, but again would require additional computer resources.

As discussed in Chapter 5 a key aim in the improvement of SST data assimilation methods is understanding how surface features relate to the deeper ocean. How can an assimilation method translate surface temperature observations into information on temperatures at depth. It has been clearly demonstrated how surface observations can be used to make corrections to temperatures within the mixed layer. In Section 5.4.5 an idea of comparing modelled and observed changes in SST in order to provide insight on the depth of the mixed layer, was introduced. Further work into this possibility could provide promising results. Ocean temperatures at depth are not well known and limited observations are available. ARGO floats are improving the situation; however, they are still sparsely distributed in comparison to the size of the oceans of the world.

Bibliography

[1] J.Icarus Allen, J. R. Siddorn, J. C. Blackford, and F. J. Gilbert. Turbulence as a control on the microbial loop in a temperate seasonally stratified marine systems model. *J. Sea Res.*, 52:1–20, 2004.

[2] S. P. Anderson and R. A. Weller. Surface buoyancy forcing and the mixed layer of the western Pacific warm pool: Observations and 1d model results. *J. Climate*, 9:3056–3085, 1996.

[3] I. Andreu-Burillo, J. Holt, R. Proctor, J. D. Annan, I. D. James, and D. Prandle. Assimilation of sea surface temperature in the POL coastal ocean modelling system. *J. Mar. Syst.*, 65:27–40, 2007.

[4] J. D. Annan and J. C. Hargreaves. Sea surface temperature assimilation for a three-dimensional baroclinic model of shelf seas. *Cont. Shelf Res.*, 19:1507–1520, 1999.

[5] WHOI Upper Ocean Mooring Data Archive. http://kuvasz.whoi.edu/uopdata/uopdata.html, April 2007.

[6] B. Barnier, L. Siefridt, and P. Marchesiello. Thermal forcing for a global ocean circulation model using a three-year climatology of ECMWF. *J. Mar. Syst.*, 6:363–380, 1995.

[7] M. J. Bell, R. M. Forbes, and A. Hines. Assessment of the FOAM global data assimilation system for reat-time operational ocean forecasting. *J. Mar. Syst.*, 25:1–22, 2000.

[8] M. J. Bell, M. J. Martin, and N. K. Nichols. Assimilation of data into an ocean model with systematic errors near the equator. *Q. J. R. Meteorol. Soc.*, 129, 2003.

[9] D. J. Bernie, S. J. Woolnough, J. M. Slingo, and E. Guilyardi. Modelling diurnal and intraseasonal variability of the ocean mixed layer. *J. Climate*, 18:1190–1202, 2005.

[10] F. Bignami, S. Marullo, R. Santoleri, and M. E. Schiano. Longwave radiation budget in the Mediterranean Sea. *J. Geophys. Res.*, 100:2501–2514, 1995.

[11] H. Burchard. Simulating the wave-enhanced layer under breaking surface waves with two-equation turbulence models. *J. Phys. Oceanogr.*, 31:3133–3145, 2001.

[12] H. Burchard and K. Bolding. Comparative analysis of four second-moment turbulence closure models for the oceanic mixed layer. *J. Phys. Oceanogr.*, 31:1943–1968, 2001.

[13] H. Burchard, K. Bolding, W. Kühn, A. Meister, T. Neumann, and L. Umlauf. Description of a flexible and extendable physical-biogeochemical model system for the water column. *J. Mar. Syst.*, 61:180–211, 2006.

[14] H. Burchard, K. Bolding, T. P. Rippeth, A. Stips, J. H. Simpson, and J. Sündermann. Microstructure of turbulence in the northern North Sea: comparative study of observations and model simulations. *J. Sea. Res.*, 47:223–238, 2002.

[15] H. Burchard, K. Bolding, and M. R. Villarreal. *GOTM, a General Ocean Turbulence Model. Theory, implementation and test cases.* Tech. Rep. EUR 18745 EN, European Commission, 1999.

[16] H. Burchard, H. Lass, V. Mohrholz, L. Umlauf, J. Sellschopp, V. Fiekas, K. Bolding, and L. Arneborg. Dynamics of medium-intensity dense water plumes in the Arkona Sea, Western Baltic Sea. *Ocean Dynamics*, 55:391–402, 2005.

[17] D. B. Chelton and M. H. Freilich. Scatterometer-based assessment of 10-m wind analyses from the operational ECMWF and NCEP numerical weather prediction models. *Mon. Wea. Rev.*, 133:409–429, 2005.

[18] D. Chen, S. E. Zebiak, and M. A. Cane. Initialization and predictability of a coupled ENSO forecast model. *Mon. Wea. Rev.*, 125:773–788, 1997.

[19] R. M. Clancy, J. M. Harding, K. D. Pollak, and P. May. Quantification of improvements in an operational global-scale ocean thermal analysis system. *J. Atmos. Oceanic Technol.*, 9:55–65, 1992.

[20] R. M. Clancy, P. A. Phoebus, and K. D. Pollak. An operational global-scale ocean thermal analysis system. *J. Atmos. Oceanic Technol.*, 7:233–254, 1990.

[21] N. E. Clark, L. Eber, R. M. Laurs, J. A. Renner, and J. F. T. Saur. Heat exchange between ocean and atmosphere in the eastern north Pacific for 1961-1971. Technical report, NOAA, 1974.

[22] M. C. Cooper and K. Haines. Data assimilation with water property conservation. *J. Geophys. Res.*, 101:1059–1077, 1996.

[23] P. Cornillon and L. Stramma. The distribution of diurnal sea surface warming events in the western Sargasso Sea. *J. Geophys. Res.*, 90:11811–11815, 1985.

[24] P. D. Craig and M. L. Banner. Modeling wave-enhanced turbulence in the ocean surface layer. *J. Phys. Oceanogr.*, 24:2546–2559, 1994.

[25] J. Crank and P. Nicolson. A practical method for numerical evaluation of solutions of partial differential equations of the heat-conduction type. *Proc. Cambridge Philos. Soc.*, 43:50–67, 1947.

[26] G. Danabasoglu, W. G. Large, J. J. Tribbia, P. R. Gent, and B. P. Briegleb. Diurnal coupling in the tropical oceans of CCSM3. *J. Climate*, 19:2347–2365, 2006.

[27] D. Dee and A. M. DaSilva. Data assimilation in the presence of forecast bias. *Q. R. Meteorol. Soc.*, 124:269–295, 1998.

[28] A. Defant. *Physical Oceanography*. Pergamon Press, 1961.

[29] J. Derber and A. Rosati. A global oceanic data assimilation system. *J. Phys. Oceanogr.*, 19:1333–1347, 1989.

[30] F-X. Le Dimet and M. Ouberdous. Retrieval of balanced fields: an optimal control method. *Tellus*, 45A:449–461, 1993.

[31] F. W. Dobson and S. D. Smith. Bulk models of solar radiation at sea. *Q. J. R. Meteorol. Soc.*, 114:165–182, 1988.

[32] C. J. Donlon, P. J. Minnett, C. Gentemann, T. J. Nightingale, I. J. Barton, B. Ward, and M. J. Murray. Toward improved validation of satellite sea surface temperature measurements for climate research. *J. Climate*, 15:353–369, 2002.

[33] C. J. Donlon and the GHRSST-PP Science Team. The recommended GHRSST-PP data processing specifications GDS (version 1 revision 1.5). Technical Report 17, GHRSST-PP, 2004.

[34] T. Ezer and G. Mellor. Data assimilation experiments in the Gulf stream region: How useful are satellite-derived surface data for nowcasting the subsurface fields. *J. Atmos. Oceanic Technol.*, 14:1379–1391, 1997.

[35] C. W. Fairall, E. F. Bradley, J. S. Godfrey, G. A. Wick, J. B. Edson, and G. S. Young. Cool-skin and warm-layer effects on sea surface temperature. *J. Geophys. Res.*, 101:1295–1308, 1996.

[36] C. W. Fairall, E. F. Bradley, J. E. Hare, A. A. Grachev, and J. B. Edson. Bulk parameterization of air-sea fluxes: Updates and verification for the COARE algorithm. *J. Climate*, 16:571–591, 2003.

[37] C. W. Fairall, E. F. Bradley, D. P. Rogers, J. B. Edson, and G. S. Young. Bulk parameterization of air-sea fluxes for TOGA-COARE. *J. Geophys. Res.*, 101:3747–3764, 1996.

[38] C. W. Fairall, J. B. Edson, S. E. Larsen, and P. G. Mestayer. Inertial-dissipation air-sea flux measurements: a prototype system using real-time computations. *J. Atmos. Oceanic Tech.*, 7:425–453, 1990.

[39] A. S. Fischer, R. A. Weller, D. L. Rudnick, C .C. Eriksen, C. M. Lee, K. H. Brink, C. A. Fox, and R. R. Leben. Mesoscale eddies, coastal upwelling, and the upper-ocean heat budget in the Arabian Sea. *Deep-Sea Res. II*, 49:2231–2264, 2002.

[40] P. Flament, J. Firing, M. Sawyer, and C. Trefois. Amplitude and horizontal structure of a large sea surface warming event during the Coastal Ocean Dynamics Experiment. *J. Phys. Oceanogr.*, 24:124–139, 1994.

[41] C. Gautier and R. Frouin. Net surface solar irradiance variability in the Central Equatorial Pacific during 1982-1985. *J. Climate*, 1992.

[42] C. L. Gentemann, C. J. Donlon, A. Stuart-Menteth, and F. J. Wentz. Diurnal signal in satellite sea surface temperature measurements. *Geophys. Res. Lett.*, 30:1140, 2003.

[43] C. Gilman and C. Garrett. Heat flux parameterization for the Mediterranean Sea: The role of atmospheric aerosols and constraints from the water budget. *J. Geophys. Res.*, 99:5119–5134, 1994.

[44] J. S. Jr. Godfrey, R. H. Johnson, R. Lukas, J.-L. Redelsperger, A. Sumi, and R. Weller. Coupled Ocean-Atmosphere Response Experiment (COARE): An interim report. *J. Geophys. Res.*, 103:14395–14450, 1998.

[45] G. J. Goni and J. A. Trinanes. Ocean thermal structure monitoring could aid in the intensity forecast of tropical cyclones. *EOS*, 84:573–580, 2003.

[46] N. I. M. Gould and S. Leyffer. An introduction to algorithms for nonlinear optimization. Technical Report 031, RAL, 2002.

[47] W. J. Gould and J. Turton. Argo - sounding the oceans. *Weather*, 61:17–21, 2006.

[48] A. K. Griffith and N. K. Nichols. Adjoint techniques in data assimilation for estimating model error. *Journal of Flow, Turbulence and Combustion*, 65:469–488, 2000.

[49] P. Y. Groisman, R. S. Bradley, and B. Sun. The relationship of cloud cover to near-surface temperature and humidity: comparison of GCM simulations with empirical data. *J. Climate*, 13:1858–1878, 2000.

[50] S. Hallsworth. *Modelling the diurnal variation of sea surface temperature using a one-dimensional ocean temperature model.* PhD thesis, University of Edinburgh, 2006.

[51] R. L. Haney. Surface thermal boundary conditions for ocean circulation models. *J. Phys. Oceanogr.*, 1:241–248, 1971.

[52] L. A. Horrocks, A. R. Harris, and R. W. Saunders. Modelling the diurnal thermocline for daytime bulk SST from AATSR. Technical Report FR 418, UK Met Office, 2003.

[53] J. T. Houghton, Y. Ding, D.J. Griggs, M. Noguer, P. J. van der Linden, and D. Xiaosu, editors. *Climate Change 2001: The Scientific Basis. Contribution of working group 1 to the third assessment report of the Intergovernmental Panel on Climate Change*, chapter 2.2 How much is the world warming, pages 110–112. Cambridge University Press, 2001.

[54] A. Isaacs, J. Daintith, and E. A. Martin, editors. *Concise Science Dictionary.* Oxford Paperbacks, 3rd edition, 1997.

[55] H. J. Isemer, J. Willebrand, and L. Hasse. Fine adjustment of large scale air-sea flux parameterizations by direct estimates of ocean heat transport. *J. Climate*, 2:1173–1184, 1989.

[56] C. Jakob and S. Klein. The role of vertically varying cloud fraction in the parametrization of microphysical processes in the ECMWF model. *Q. R. Meteorol. Soc.*, 125:941–965, 1999.

[57] N. G. Jerlov. *Marine Optics*. Elsevier, 1976.

[58] S. A. Josey, R. W. Pascal, P. K. Taylor, and M. J. Yelland. A new formula for determining the atmospheric longwave flux at the ocean surface at mid-high latitudes. *J. Geophys.Res.*, 108, 2003.

[59] R. Kalman. A new approach to linear filtering and prediction problems. *J. Basic Eng.*, 82:35–45, 1960.

[60] E. Kalnay. *Atmosheric Modeling, Data Assimilation and Predictability*. Cambridge University Press, 2003.

[61] I. V. Kamenkovich and E. S. Sarachik. Reducing errors in temperature and salinity in an ocean model forced by restoring boundary conditions. *J. Phys. Oceangr.*, 31:1856–1869, 2004.

[62] L. H. Kantha and C. A. Clayson. An improved mixed layer model for geophysical applications. *J. Geophys. Res.*, 99:25235–25266, 1994.

[63] A. Kaplan, M. A. Kushnir, M. A. Cane, and M. B. Blumenthal. Reduced space optimal analysis for historical data sets: 135 years of Atlantic sea surface temperatures. *J. Geophys. Res.*, 102:27835–27860, 1997.

[64] A. B. Kara, P. A. Rochford, and H. E. Hurlburt. An optimal definition for ocean mixed layer depth. *J. Geophys. Res.*, 105:16803–16821, 2000.

[65] K. B. Katsaros. Parameterization schemes and models for estimating the surface radiation budget. In G. L. geernaert and W. J. Plant, editors, *Surface Waves and Fluxes*, volume II, pages 339–368. Kluwer, 1990.

[66] K. B. Katsaros and A. V. Soloviev. Vanishing horizontal sea surface temperature gradients at low wind speeds. *Bound. Layer Met.*, 112:381–396, 2004.

[67] K. B. Katsaros, A. V. Soloviev, R. H. Weisberg, and M. E. Luther. Reduced horizontal sea surface temperature gradients under conditions of clear skies and weak winds. *Bound. Layer Met.*, 116:175–185, 2005.

[68] Y. Kawai and H. Kawamura. Evaluation of the diurnal warming of sea surface temperature using satellite-derived marine meteorological data. *J. Oceanogr.*, 58:805–814, 2002.

[69] P. D. Killworth, D. A. Smeed, and A. J. G. Nurser. The effects on ocean models of relaxation toward observations at the surface. *J. Phys. Oceanogr.*, 30:160–174, 2000.

[70] S. Kizu. Systematic errors in estimation of insolation by empirical formulas. *J. Oceanogr.*, 54:165–177, 1998.

[71] J. Kondo. Air-sea bulk transfer coefficients in diabatic conditions. *Bound. Layer Met.*, 9:91–112, 1975.

[72] E. Kraus and S. Turner. A one-dimensional model of the seasonal thermocline: The general theory and its consequences. *Tellus*, 19:98–106, 1967.

[73] E. B. Kraus and J. A. Businger. *Atmospheric-Ocean Interaction*. Oxford University Press, 1994.

[74] W. G. Large, J. C. McWilliams, and S. C. Doney. Oceanic vertical mixing: A review and a model with a nonlocal boundary layer parameterization. *Rev. Geophys.*, 34:363–403, 1994.

[75] D. V. Ledvina, G. S. Young, R. A. Miller, and C. W. Fairall. The effects of averaging on bulk estimates of heat and momentum fluxes for the tropical western Pacific ocean. *J. Geophys. Res.*, 98:20211–20218, 1993.

[76] T. W. Liu, K. B. Katsaros, and J. A. Businger. Bulk parameterization of air-sea exchanges of heat and water vapor including the molecular constraints at the interface. *J. Atmos. Sci.*, 36:1722–1735, 1979.

[77] J. Lu and W. W. Hsieh. On determining initial conditions and parameters in a simple coupled atmosphere-ocean model by adjoint data assimilation. *Tellus*, 50a:534–544, 1998.

[78] A. Manda, N. Hirose, and T. Yanagi. Feasible method for the assimilation of satellite-derived SST with an ocean circulation model. *J. Atmos. Oceanic Technol.*, 22:746–756, 2005.

[79] S. Martin. *An introduction to ocean remote sensing.* Cambridge Univerisity Press, 2004.

[80] J. P. McCreary, K. E. Kohler, Hood R. R, S. Smith, J. Kindle, A. S. Fischer, and R. A. Weller. Influences of diurnal and intraseasonal forcing on mixed-layer and biological variability in the central Arabian Sea. *J. Geophy. Res.*, 106:7139–7155, 2001.

[81] M. E. McCulloch, J. O. S. Alves, and M. J. Bell. Modelling shallow mixed-layers in the northeast Atlantic. *J. Mar. Syst.*, 52:107–119, 2004.

[82] R. McIlveen. *Fundamentals of Weather and Climate.* Chapman and Hall, London, second edition, 1992.

[83] G. L. Mellor and T. Yamada. Development of a turbulence closure model for geophysical fluid problems. *Rev. Geophys. Space Phys.*, 20:851–875, 1982.

[84] C. Merchant. Report from the DV-WG. In *Report of the Sixth GODAE High Resolution SST Pilot Project Science Team Meeting*, pages 61–69. GHRSST-PP, 2005.

[85] General Ocean Turbulence Model. http://www.gotm.net, April 2007.

[86] General Ocean Turbulence Model.
http://www.gotm.net/index.php?go=software&page=testcases, April 2007.

[87] A. S. Monin and A. M. Obukhov. Basic laws of turbulent mixing in the ground layer of the atmosphere. *Trans. Geophys. Inst. Akad.*, 151:163–187, 1954.

[88] A. Morel. Optical modeling of the upper ocean in relation to its biogenous matter content (case I waters). *J. Geophys. Res.*, 93:10749–10768, 1988.

[89] A. Morel and D. Antoine. Heating rate within the upper ocean in relation to its bio-optical state. *J. Phys. Oceangr.*, 24:1652–1665, 1994.

[90] K. A. Moyer and R. A. Weller. Observations of surface forcing from the subduction experiment: A comparison with global model products and climatological datasets. *J. Climate*, 10:2725–2742, 1997.

[91] B. B. Nardelli, S. Marullo, and R. Santoleri. Diurnal variations in AVHRR SST fields: A strategy for removing warm layer effects from daily images. *Remote Sens. Environ.*, 95:47–56, 2005.

[92] I. M. Navon. Practical and theoretical aspects of adjoint parameter estimation and identifiability in meteorology and oceanography. *Dyn. Atmos. Oceans*, 27:55–79, 1997.

[93] P. P. Niiler and E. B. Kraus. One-dimensional models of the upper ocean. In E. B. Kraus, editor, *Modelling and prediction of the upper layers of the oceans*, pages 143–172. Pergamon Press, 1975.

[94] A. G. O'Carroll, J. G. Watts, N. A. Rayner, and R. W. Saunders. Influence of sea surface temperature products from the ATSR series on HadISST1 global analyses. Technical Report FR 450, UK Met Office, 2004.

[95] J. C. Ohlmann and D. A. Siegel. Ocean radiant heating. Part II: Parameterizing solar radiation transmission through the upper ocean. *J. Phys. Oceanogr.*, 30:1849–1865, 2000.

[96] J. C. Ohlmann, D. A. Siegel, and C. D. Mobley. Ocean radiant heating. Part I: Optical influences. *J. Phys. Oceanogr.*, 30:1833–1848, 2000.

[97] Working Group on Air-Sea Fluxes (WGASF). Intercomparison and validation of ocean-atmosphere energy flux fields, final report of the joint WCRP/SCOR working group on air-sea fluxes (SCOR working group 110). Technical report, World Climate Research Programme, 2000.

[98] H. A. Panofsky and J. A. Dutton. *Atmospheric Turbulence, Models and Methods for Engineering Applications.* John Wiley & Sons, 1984.

[99] S. V. Patankar. *Numerical Heat Transfer and Fluid Flow.* Taylor & Francis, 1980.

[100] C. A. Paulson and J. J. Simpson. Irradiance measurements in the upper ocean. *J. Phys. Oceanogr.*, 7:952–956, 1977.

[101] C. A. Paulson and J. J. Simpson. The temperature difference across the cool-skin of the ocean. *J. Geophys. Res.*, 86:11044–11054, 1981.

[102] R. E. Payne. Albedo of the sea surface. *J. Atmos. Sci.*, 29:959–970, 1972.

[103] L. S. Pontryagin, V. G. Boltyanskii, R. V. Gamkrelidze, and E. F. Mishchenko. *The Mathematical Theory of Optimal Processes.* Wiley & Sons, 1962.

[104] J. F. Price and R. A. Weller. Diurnal cycling: Observations and models of the upper ocean response to diurnal heating. *J. Geophys. Res.*, 91, 1986.

[105] J. F. Price, R. A. Weller, C. M. Boewrs, and M. G. Briscoe. Diurnal response of SST observed at the long term upper ocean study (34N, 70W) in the Sargasso Sea. *J. Geophys. Res.*, 92:14,480–14,490, 1987.

[106] GODAE High Resolution Sea Surface Pilot Project. http://www.ghrsst-pp.org, April 2007.

[107] GODAE High Resolution Sea Surface Pilot Project. http://www.ghrsst-pp.org/sst-definitions.html, April 2007.

[108] D. K. Ralston and M. T. Stacey. Shear and turbulence production across subtidal channels. *J. Mar. Syst.*, 64:147–171, 2006.

[109] R. K. Reed. On estimating insolation over the ocean. *J. Phys. Oceanogr.*, 7:482–485, 1977.

[110] R. W. Reynolds. Impact of Mount Pinatubo aerosols on satellite-derived sea surface temperatures. *J. Climate*, 6:768–774, 1993.

[111] R. W. Reynolds, N. A. Rayner, T. M. Smith, D. C. Stokes, and W. Wang. An improved in situ satellite SST analysis for climate. *J. Climate*, 15:1609–1625, 2002.

[112] R. W. Reynolds and T. M. Smith. Improved global sea surface temperature analyses using optimum inerpolation. *J. Climate*, 7:929–948, 1994.

[113] I. S. Robinson, N. C. Wells, and H. Charnock. The sea surface thermal boundary layer and its relevance to the measurement of sea surface temperature by airborne and spaceborne radiometers. *Int. J. Remote Sens.*, 5:19–45, 1984.

[114] C.D. Rodgers. *Inverse methods for atmospheric sounding theory and practice.* World Scientific, 2000.

[115] W. Rodi. Examples of calculation methods for flow and mixing in stratified fluids. *J. Geophys. Res.*, 92:5305–5328, 1987.

[116] A. Rosati and K. Miyakoda. A general circulation model for upper ocean simulation. *J. Phys. Oceanogr.*, 18:1601–1626, 1988.

[117] A. Rosati, K. Miyakoda, and R. Gudgel. The impact of ocean initial conditions on ENSO forecasting with a coupled model. *Mon. Wea. Rev.*, 125:754–772, 1997.

161

[118] Y. Sasaki. Some basic formalisms in numerical variational analysis. *Mon. Wea. Rev.*, 98:875–883, 1970.

[119] P. M. Saunders. The temperature at the ocean-air interface. *J. Atmos. Sci.*, 24:269–273, 1967.

[120] M .E. Schiano. Insolatation over the western Mediterranean Sea: A comparison of direct measurement and Reed's formula. *J. Geophys. Res.*, 101:3831–3838, 1996.

[121] A. Schiller and J. S. Godfrey. A diagnostic model of the diurnal cycle of sea surface temperature for use in coupled ocean-atmosphere models. *J. Geophys. Res.*, 110:11014–11023, 2005.

[122] G. R. Seckel and F. H. Beaudry. The radiation from sun and sky over north Pacific ocean (abstract). *Trans. Amer. Geophys. Union*, 54:1114, 1973.

[123] J. Segschneider, D. L. T. Anderson, and T. N. Stockdale. Towards the use of altimetry for operational seasonal forecasting. *J. Climate*, 13:3115–3138, 2000.

[124] ESSC Godiva Project Server. http://www.nerc-essc.ac.uk/godiva/, April 2007.

[125] K. Shankaranarayanan and M. A. Donelan. A probabilistic approach to scatterometer function verification. *J. Geophys. Res.*, 106:19969–19990, 2001.

[126] L. K. Shay, G. J. Goni, and P. G. Black. Effects of a warm oceanic feature on hurricane Opal. *Mon. Wea. Rev.*, 128:1366–1383, 2000.

[127] T. Shinoda. Impact of the diurnal cycle of solar radiation on intraseasonal SST variability in the western equatorial Pacific. *J. Climate*, 18:2628–2636, 2005.

[128] T. Shinoda and H. H. Hendon. Mixed layer modeling of intraseasonal variability in the tropical western Pacific and indian oceans. *J. Climate*, 11:2668–2685, 1998.

[129] J. J. Simpson and T. D. Dickey. Alternative parameterizations of downward irradiance and their dynamic significance. *J. Phys. Oceangr.*, 11:876–882, 1981.

[130] R. C. Smith and K. S. Baker. Optical classification of natural waters. *Limnol. Oceanogr.*, 23:260–267, 1978.

[131] J. Stark and C. Donlon. A new high-resolution operational sea surface temperature analysis for oceanography and meteorology. *Eos Trans. AGU, Ocean Sci. Meet. Suppl.*, 87:Abstract OS12A–04, 2006.

[132] J. W. Stevenson and P. P. Niiler. Upper ocean heat budget during the Hawaii-to-Tahiti shuttle experiment. *J. Phys. Oceanogr.*, 13:1894–1907, 1983.

[133] A. Stips, H. Burchard, K. Bolding, H. Prandke, and A. Wüest. Measurement and simulation of viscous dissipation rates in the wave affected surface layer. *Deep Sea Res. II*, 52:1133–1155, 2005.

[134] H. Stommel. Observations of the diurnal thermocline. *Deep Sea Res.*, 16:269–284, 1969.

[135] L. Stramma, P. Cornillon, R. A. Weller, J. F. Price, and M. G. Briscoe. Large diurnal sea surface temperature variability: Satellite and in situ measurements. *J. Phys. Oceanogr.*, 56:345–358, 1986.

[136] A. C. Stuart-Menteth, I. S. Robinson, and P. G. Challenor. A global study of diurnal warming using satellite-derived sea surface temperature. *J. Geophys. Res.*, 108:3155, 2003.

[137] A. C. Stuart-Menteth, I. S. Robinson, and C. J. Donlon. Sensitivity of the diurnal warm layer to meteorological fluctuations. Part 2: A new parameterisation for diurnal warming. *Journal of Atmospheric and Ocean Science*, 10:209–234, 2005.

[138] A. C. Stuart-Menteth, I. S. Robinson, R. A. Weller, and C. J. Donlon. Sensitivity of the diurnal warm layer to meteorological fluctuations. Part 1: Observations. *Journal of Atmospheric and Ocean Science*, 10:193–208, 2005.

[139] R. Swinbank, V. Shutyaev, and W. A. Lahoz, editors. *Data Assimilation for the Earth System.* NATO Science Series IV: Earth and Environmental Sciences - Vol. 26. Kluwer Academic Publishers, 2003.

[140] Remote Sensing Systems. http://www.remss.com, April 2007.

[141] H. H. Syu and D. Neelin. ENSO in a hybrid coupled model. Part II: Prediction with piggyback data assimilation. *Climate Dyn.*, 16:35–48, 2000.

[142] Y. Tang and W. W. Hsieh. ENSO simulation and prediction in a hybrid coupled model with data assimilation. *J. Meteor. Soc. Japan*, 81:1–19, 2003.

[143] Y. Tang and R. Kleeman. A new strategy for assimilating SST data for ENSO predictions. *Geophys. Res. Lett.*, 29:1841, 2002.

[144] Y. Tang, R. Kleeman, and A. M. Moore. SST assimilation experiments in a tropical Pacific ocean model. *J. Phys. Oceangr.*, 34:623–642, 2004.

[145] H. Tennekes and J. L. Lumley. *A First Course in Turbulence.* MIT Press, 1972.

[146] J. N. Thepaut and P. Courtier. Four-dimensional data assimilation using the adjoint of a multi-level primitive-equation model. *Quart. J. Roy. Meteor. Soc.*, 117:1225–1254, 1991.

[147] L. Umlauf and H. Burchard. A generic length-scale equation for geophysical turbulence models. *J. Mar. Res.*, 61:235–265, 2003.

[148] L. Umlauf and H. Burchard. Second-order turbulence closure models for geophysical boundarys. a review of recent work. *Cont. Shelf Res.*, 25:795–827, 2005.

[149] L. Umlauf, H. Burchard, and K. Bolding. *General Ocean Turbulence Model. Scientific documentation. v3.2.* Marine Science Reports no. 63, Baltic Sea Research Institute Warnemnde, Warnemnde, Germany, 2005.

[150] OceanColor Webmaster. http://oceancolor.gsfc.nasa.gov/, April 2007.

[151] P. J. Webster, C. A. Clayson, and J. A. Curry. Clouds, radiation, and the diurnal cycle of sea surface temperature in the tropical western Pacific. *J. Climate*, 9:1712–1730, 1996.

[152] P. J. Webster and R. Lukas. TOGA COARE: The Coupled Ocean - Atmosphere Response Experiment. *Bull. Am. Meteorol. Soc.*, 73:1377–1416, 1992.

[153] L. Wei, Y. Rucong, L. Hailong, and Y. Yongqiang. Impacts of diurnal cycle of SST on intraseasonal variation of surface heat flux over the western Pacific warm pool. *Adv. Atmos. Sci.*, 18:793–806, 2001.

[154] R. A. Weller and S. P. Anderson. Surface meteorology and air-sea fluxes in the western tropical Pacific warm pool during the TOGA Coupled Ocean-Atmosphere Response Experiment. *J. Climate*, 9:1959–1990, 1996.

[155] R. A. Weller, M. F. Baumgartner, S. A. Josey, A. S. Fischer, and J. C. Kindle. Atmospheric forcing in the Arabian Sea during 1994-1995: observations and comparisons with climatology and models. *Deep-Sea Res. II*, 45:1961–1999, 1998.

[156] R. A. Weller, A. S. Fischer, D. L. Rudnick, C. C. Eriksen, T. D. Dickey, J. Marra, C. Fox, and R. Leben. Moored observations of upper-ocean response to the monsoons in the Arabian Sea during 1994-1995. *Deep-Sea Res. II*, 49:2195–2230, 2002.

[157] G. Yang and J. Slingo. The diurnal cycle in the tropics. *Mon. Wea. Rev.*, 129:784–801, 2001.

[158] X. Zeng and A. Beljaars. A prognostic scheme of sea surface skin temperature for modelling and data assimilation. *Geophys. Res. Lett.*, 32:14605–14609, 2005.